KU LEUVEN

ARENBERG DOCTORAL SCHOOL
Faculty of Engineering Science

Quasi 2D Si-O superlattices for nanoelectronic applications

Suseendran Jayachandran

Supervisors:
Prof.Dr.Ir.Marc Heyns
Prof.Dr.Annelies Delabie

Dissertation presented in partial fulfillment of the requirements for the degree of Doctor in Engineering Science: Materials Engineering

October 2016

Quasi 2D Si-O superlattices for nanoelectronic applications

Suseendran JAYACHANDRAN

Examination committee:
Prof.Dr.Willy Sansen, chair
Prof.Dr.Ir.Marc Heyns, supervisor
Prof.Dr.Annelies Delabie, supervisor
Prof.Dr.Jean-Pierre Locquet
Prof.Dr.Wilfried Vandervorst
Prof.Dr.Shaun Carl
Prof.Dr.Ngoc Duy Nguyen (University of Liège, Belgium)
Dr.Matty Caymax (Imec, Belgium)
Prof.Dr.Jin Won Seo,Secretary

External jury member
(External affiliation)

Dissertation presented in partial fulfillment of the requirements for the degree of Doctor in Engineering Science: Materials Engineering

October 2016

Dedicated to my parents, my brother and my wife.

If you want something you've never had, You must be willing to do something you've never done

- Thomas Jefferson

Acknowledgements

Succeeding PhD is a dream for many students including me. It is not easy and requires meticulous efforts. In addition to research, I learned more on the time management and importantly, gained lots of patience. I would like to thank many people, who made it possible.

First, I would like to thank my Promoters - Prof. Marc Heyns and Prof. Annelies Delabie for giving me this opportunity to work on this research. Next, I would like to thank the examination committee, for giving inputs to improve my PhD manuscript. I would also like to thank the "Superlattice Bi-weekly meeting" committee, who were guiding me periodically for the past 4 years. I would like thank Prof. Wilfried Vandervorst and Matty cayamx, who helped me at difficult times with their valuable inputs. Many times, I simply knock their office door to get my questions clarified. I would also like to thank Eddy Simoen, for the efficient and progressive meetings at the coffee corners. Would be glad, if I could get an opportunity to work with him again.

Second, I would like to convey my sincere gratitude to Annelies Delabie, who was my only pushing factor to do things on time. She reviewed all my research/paper work and ensured that, I am on the progressive track. There was always a good balance between her guidance and at times, where she expected me to work alone. Thanks always Annelies.

Next, thanks to the Hardware engineers (Charles Koopmanschaap, Raf Rennan, Rachid and Elie) of the Polygon tool in 200 mm clean room. Despite this tool being at low priority, these people always help me with hardware issues even during non-working hours. Thanks guys.

I would also like to thank the MCA team of IMEC, especially Johan Meersshaut and Bastien Douhard, who helped with all the questions on RBS and SIMS respectively.

I would also like to thank my friends Gokulakrishnan, Hariharasudan,

Antony, Ravi Chandra, Marissa, Josephine, Shibesh, Siva, Sadhish, Sathish, Gowri, Jie Hu and many others for a fun filled social life at Leuven. Gokul, Hari, Marissa and Ravi are few of my close friends, where we all live together like a family. Thanks guys.

Last but not least, I would like to thank my parents and my brother for bearing my absence for the past 6 years. I am being the first person in our family to hold a PhD degree, which comes at the expense of their numerous sacrifices. A poor and cute girl, my wife (Saranya) kept cooking mouth watering dishes whenever I am back home. She always wishes me to stay next to her at all times, but it was hard during the last phase of my PhD. I would like to thank her for tolerating me.

I love you all and thanks for everything.

Abstract

Two dimensional (2D) materials are explored in the context of scaling complementary metal oxide semiconductor (CMOS) devices for future technology nodes. Quasi 2D Silicon (Si) - Oxygen (O) superlattices (SLs) are promising channel materials consisting of alternating periods of epitaxial Si layers and O atomic layers (ALs). The O ALs in Si perturb the periodic lattice potential and confine the charge carriers, leading to an anisotropic band structure. The longitudinal effective mass along the channel direction is lowered, where a greater carrier mobility is achieved. Simultaneously, the transverse effective mass in the perpendicular direction is enhanced, resulting in a lower gate leakage current. Thus, transistors with band-engineered Si-O SL channels can demonstrate a high on-off current ratio. However, the growth of epitaxial Si-O SL is not straightforward and involves intricate challenges. The surface structures of O ALs that can enable epitaxial ordering of Si are not understood and hence the fabrication of fully crystalline Si-O SL with multiple periods is a major challenge.

This research presents a systematic study of structural and electrical properties of epitaxial Si-O SLs grown by chemical vapor deposition (CVD). First, we present our insight in the growth processes and the structural properties of epitaxial Si-O SLs. Second, we evaluate the carrier mobility of the Si-O SL channel integrated in a MOS device.

Based on our insight on the O surface chemistry and the Si CVD kinetics, we have designed a process that enables epitaxial Si despite the presence of multiple O layers. The O surface structure, the O-content and the Si deposition rate affect the epitaxy of Si on O AL. With an O-content of less than 1 O AL, after O_3 exposure on H−Si(100), the O atoms are mainly configured in the surface Si−Si dimers and back bonds (−OSiH). This results in a minor surface distortions that can still enable epitaxial ordering of Si. We propose that the Si epitaxy proceeds by direct epitaxial seeding on H−Si as well as on H−SiOSi surface structures. The reduction of the Si deposition rate by a factor of two as

compared to the Si homo-epitaxy allows for sufficient time for the Si adatoms to diffuse on the surface, allowing their incorporation in the Si lattice.

The Si-O SLs with multiple Si-O periods are achieved after surface H-passivation at each period of Si. This passivation ensures a sub-AL O-content and hence the epitaxial SL structures.

On the electrical performance, a degradation in mobility with an increase in the number of Si-O periods and Si thickness between the O ALs is observed. The degradation at low and high gate fields is presumed to be due to Coulomb and surface scattering respectively. The Coulomb scattering is primarily due to the donor hole traps, while the accumulation of the surface roughness during SL growth causes surface scattering. However, the scattering can be minimized by decreasing the Si thickness between the O ALs. The Si-O SL can be further explored in terms of low Si thickness, different Si-O surface structures and number of Si-O periods which can enhance the carrier mobility of future devices.

Beknopte samenvatting

Twee-dimensionele (2D) materialen worden onderzocht als mogelijke nieuwe bouwstenen voor toekomstige complementaire metaal oxide halfgeleider (CMOS) componenten. Silicium-zuurstof (Si-O) superroosters zijn quasi-2D materialen die bestaan uit alternerende periodes van kristallijne Si lagen en atoomlagen van O. Deze interessante halfgeleiders worden onderzocht als alternatief materiaal voor het kanaal van CMOS transistoren. De aanwezigheid van de O-atoomlagen verstoort de periodische roosterpotentiaal van het siliciumkristal, zodat een anisotrope bandenstructuur ontstaat. Een hogere mobiliteit van de ladingsdragers wordt beoogd door de afname van de effectieve massa in de richting van het kanaal. Tegelijkertijd wordt een lagere lekstroom beoogd door een toename van de effectieve massa in de richting loodrecht op die van het kanaal. Het creëren van Si-O superroosters door middel van epitaxiale groeiprocessen is echter erg uitdagend: de epitaxiale uitlijning van het kristalrooster mag niet verstoord worden door de aanwezigheid van de O atomen, en dit doorheen de verschillende periodes van het Si-O superrooster. Dit werk bestudeert de structuur en elektrische eigenschappen van Si-O superroosters, gecreëerd door epitaxiale groei met chemische dampdepositie (CVD). Het epitaxiale groeiproces en de resulterende structuur van de Si-O superroosters worden onderzocht. Daarnaast wordt ook de mobiliteit van Si-O superroosters bestudeerd na integratie in MOS transistoren.

Ons vernieuwde inzicht in de oppervlaktechemie en kinetica van de O en Si depositieprocessen maakt de ontwikkeling van een proces voor de epitaxiale groei van Si-O superroosters mogelijk. Kristallijne Si-O superroosters kunnen bekomen worden door epitaxiale groei voor zeer specifieke oppervlaktestructuren van de O laag. Deze specifieke oppervlaktestructuren kunnen bekomen worden door chemisorptie van ozon op een H-getermineerd Si(100) oppervlak, waarbij de hoeveelheid O atomen beperkt wordt tot minder dan een atoomlaag. De incorporatie van O atomen in de Si-Si bindingen aan het oppervlak veroorzaakt slechts minieme verstoringen van de oppervlaktestructuur, waardoor epitaxiale

uitlijning van het superrooster op het kristaloppervlak mogelijk blijft ondanks de aanwezigheid van de O atomen. Een lage depositiesnelheid van het Si CVD proces zorgt voor genoeg tijd voor oppervlaktediffusie van de Si oppervlaktedeeltjes, wat incorporatie in het kristalrooster bevordert. Bij het opbouwen van Si-O superroosters met meerdere periodes is controle van de hoeveelheid O in de atoomlagen essentieel, wat door passivering van het Si oppervlak met waterstof na de Si depositie verwezenlijkt wordt.

Wat betreft de elektrische eigenschappen wordt na integratie van de Si-O superroosters in transistoren geen mobiliteitstoename waargenomen. Superroosters met een groter aantal periodes en/of dikkere Si lagen geven ruwere oppervlakken. Dit versterkt Coulomb- en oppervlakteverstrooiing van de ladingsdragers waardoor hun mobiliteit afneemt. De afname kan beperkt worden door de dikte van de Si lagen in het superrooster te beperken. Dit inzicht geeft een interessante richting aan voor verder onderzoek naar de mobiliteit van de Si-O superroosters.

Contents

List of Publications

Journal Publications

1. Simoen E, **Jayachandran S.**, Delabie A, Caymax M, Heyns M "A deep-level transient spectroscopy study of silicon Schottky barriers containing a Si-O superlattice". Accepted in *Phys. Stat. Sol. Rapid Research Comminations* (Sep-2016).

2. Kolomiiets N, Afanas'ev V, **Jayachandran S.** , Delabie A, Heyns, M , Stesmans A. Valence band profile in two dimensional Silicon - Oxygen superlattices probed by internal photoemission. *ECS Journal of Solid State Science and Technology* 5(11) Q3008-Q3011 (2016).

3. **Jayachandran S.**, Martens K, Simoen E, Bender H, Caymax M, Meersschaut J, Vandervorst W, Heyns M, Delabie A. "Quasi two dimensional Si-O superlattices: atomically controlled growth and electrical properties". *ECS Journal of Solid State Science and Technology*, 5 (7) P396-P403 (2016).

4. **Jayachandran S.**, Billen A, Bender H, Douhard B, Conard T, Meersschaut J, Caymax M, Vandervorst W, Heyns M, Delabie A. "Growth mechanisms of Si epitaxy on O atomic layers: Impact of O-content and surface structure. *Applied surface science* 384, 152-160 (2016).

5. Simoen E, **Jayachandran S.**, Delabie A, Caymax M, Heyns M "Deep levels in silicon-oxygen superlattices", *Semicond. Sci. Technol.* 31 (2) 025015 (2016).

6. Simoen E, **Jayachandran S.**, Delabie A, Caymax M, Heyns M "Comparison between Si/SiO_2 mid-gap interface states and deep levels associated with silicon-oxygen superlattices in p-type silicon", *Physica Status Solidi C: Current topics in Solid state physics* 1-6 (2016).

7. **Jayachandran S.**, Billen A, Dekkers H, Douhard B, Conard T, Meersschaut J, Caymax M, Vandervorst Wand Heyns M "Deposition of O atomic layers on Si(100) substrates for epitaxial Si-O superlattices: investigation of the surface chemistry".*Applied Surface Science* 324, 251-257 (2015).

8. **Jayachandran S.**, Delabie A, Maggen J, Caymax M, Loo R, Meersschaut J, Lenka H, Vandervorst W and Heyns M "Chemical vapor deposition processes for the fabrication of epitaxial Si-O superlattices". *Thin Solid Films* 557, 36-41 (2014).

9. Delabie A, **Jayachandran S.**, Caymax M, Loo R, Maggen J, Pourtois G, Douhard B, Conard T, Meersschaut J, Lenka H, Vandervorst W and Heyns M "Epitaxial chemical vapor deposition of silicon on an oxygen monolayer on Si (100) substrates". *ECS Solid State Letters* 2(11), P104-P106 (2013).

Conference Contributions

1. Simoen E, **Jayachandran S.**, Delabie A, Caymax M, Heyns M "Comparison between Si/SiO_2 mid-gap interface states and deep levels associated with silicon-oxygen superlattices in p-type silicon", EMRS Spring Meeting - May (2016).

2. **Jayachandran S.**, Martens K, Simoen E, Caymax M, Vandervorst W, Heyns M, Delabie A "Quasi 2D epitaxial Si-O superlattices: Growth, device performance and defect analysis" MRS Spring Meeting and Exhibit, Arizona- USA, March (2016).

3. Simoen E, Dhayalan S.K, **Jayachandran S.**, Gupta S, Gencarelli F, Hikavyy A, Loo R, Rossel E, Caymax M, Langer R, Barla K, Vrielinck H, Lauwaert J "Study of electrically active defects in epitaxial layers on silicon" CSTIC, China 1-3 (2016).

4. **Jayachandran S.**, Martens K, Lu A, Nishio K, Pourtois G, Delabie A, Caymax M and Heyns M "Heterostructures by inserting oxygen monolayers in Si: 2D nanolattice growth, electronic properties and MOSFET device characteristics". APS March Meeting, Texas, USA (2015).

5. Nadiia K, Afanas'ev V.V, **Jayachandran S.**, Delabie A, Heyns M, Stesmans A "Valence band profile in Si-O superlattices probed by internal photoemission". EMRS Fall Meeting, Warsaw, Poland (2015).

6. **Jayachandran S.**, Delabie A, Lin D, Douhard B, Richard O, Meersschaut J, Moussa A, Bender H, Caymax M, Vandervorst W and Heyns M "Fabrication and characterization of epitaxial Si-O superlattices". E-MRS Fall Meeting, Warsaw, Poland (2014).

7. **Jayachandran S.**; Delabie, A.; Douhard, B.; Conard, T.; Meersschaut, J.; Bender, H.; Caymax, M.;Vandervorst, W. and Heyns, M. "Insight in bonding configuration of O atoms on Si(100) surface for epitaxial Si-O superlattices" ChemSYS, blankenberge, Belgium (2014).

8. Delabie A, **Jayachandran S.**, Billen A, Douhard B, Conard T, Meersschaut J, Bender H, Demeulemeester J, Vandervorst W, Caymax M, Heyns M. "Surface chemistry of deposition processes for epitaxial Si-O superlattices. 14^{th} International conference on atomic layer deposition Kyoto Japan (2014).

9. Delabie A, **Jayachandran S.**, Maggen J, Meersschaut J, Caymax M, Loo R, Vandervorst W and Heyns M "Deposition processes for the fabrication of epitaxial Si-O superlattices". ICSI-8, Fukuoka, Japan (2013).

List of Abbreviations

2D	Two-dimensional
AFM	Atomic force microscopy
AL	Atomic layer
ALD	Atomic layer deposition
APT	Atom probe tomography
ATR-FTIR	Attenuated transmission reflectance Fourier transform infrared spectroscopy
CB	Conduction band
C-V	Capacitance - Voltage characteristics
CVD	Chemical vapor deposition
DL	SIMS Detection limit
DLTS	Deep level transient spectroscopy
DOS	Density of states
EL	Electroluminescence spectroscopy
EOT	Effective Oxide thickness
ESR	Electron Spin resonance
F_{dis}	Fraction of displaced Si atoms
FGA	Forming gas anneal
FIB	Focused Ion beam
FT-DLTS	Fourier Transform - Deep level transient spectroscopy
FWHM	Full width at half maximum
GR	Growth rate

IPE	Internal photoemission spectroscopy
ISP	Intermediate surface passivation
I-V	Current - Voltage characteristics
MBE	Molecular beam epitaxy
MOSCAP	Metal oxide semiconductor capacitor
MOSFET	Metal oxide field effect transistor
PECVD	Plasma enhanced chemical vapor deposition
PL	Photoluminescence spectroscopy
RBS/C	Rutherford back scattering - channeling spectrometry
rms	root mean square
RT	Room Temperature
SOI	Silicon on Insulator
SIMS	Secondary ion mass spectroscopy
SL	Superlattice
SPER	Sold phase epitaxial regrowth
SSRW	Super steep retrograde well doping
STM	Scanning Tunneling Microscopy
TEM	Transmission electron microscopy
VB	Valence band
WCA	Water Contact Angle
XPS	X-ray photo-electron spectroscopy

List of Symbols

Symbol	Units	Description
A^*	A/cm^2K^2	Richardson constant
a_0	Å	Inter atomic distance of Si
A_{cap}	cm^{-2}	Area of the MOS capacitor
β		Energy resolution factor
b	nm	Si thickness sandwiched between O ALs
C_{acc}	pF	Accumulation capacitance
C_G	cm^{-2} s_{-1}	Concentration of silane in the gas stream
C_{gc}	F cm^{-2}	Gate to channel capacitance
C_{ox}	μFcm^{-2}	Oxide Capacitance
C_R	pF	Saturated capacitance
C_S	cm^{-2} s_{-1}	Concentration of silane on the Si wafer surface
ΔC	pF	DLTS amplitude
d	cm	Thickness of the CVD boundary layer
D	cm^2 s^{-1}	Diffusion Coefficient
D_T	cm^{-2} eV^{-1}	Density of states
E_1	eV	Optical Singularity along [111] direction of Si
E_2	eV	Optical Singularity along [100] direction of Si
E_{des}	eV	Activation energy for H_2 desorption
E_{diff}	eV	Activation energy for surface diffusion of Si adatom
E_g	eV	Si band gap
ϵ_a, ϵ_b, ϵ_c	%	Strain along [110] , [$\bar{1}$10 and [001] directions
ϵ_{Si}		Relative permittivity of Si
E_T	eV	Activation energy of the defect
E_V	eV	Top of valence band edge
f	eV/atom	Formation energy
F_{SiH_4}	cm^{-2} s^{-1}	SiH_4 flux rate

Symbol	Units	Description
g_{ds}	siemens	Channel conductance
g_m	siemens	Transconductance
h	m^2kgs^{-1}	Plank constant
I_{ds}	A	Channel current
κ		Dielectric constant
k	JK^{-1}	Boltzmann constant
k_{des}		Rate constant for desorption
L	μm	Length of the transistor
μ_{eff}	$(cm^2V^{-1}s^{-1})$	Effective carrier mobility
μ_n	cm^2/Vs	Electron Mobility
μ_o	cm^2/Vs	Hole Mobility
ν_{des}	s^{-1}	Attempt frequency of H_2 desorption
ν_{diff}	s^{-1}	Attempt frequency of Si adatom diffusion
M_{SiH_4}	mol^{-1}	Molar mass of SiH_4
m^*_{xx}		Longitudinal/Transport effective mass
m^*_{zz}		Transverse/Tunneling effective mass
Δm	g	Change in mass
n	-	Number of Si-O periods
N_A	mol^{-1}	Avogadro number
N_{dep}	cm^{-2}	Defect centers in the depletion region
N_{dop}	cm^{-3}	Substrate doping density
n1		Refractive index of ATR-crystal (Ge)
n2		Refractive index of Si
Φ_B	eV	Barrier height
Φ_e	eV	Spectral IPE threshold
p_{SiH_4}	mTorr	Partial pressure of SiH_4
P_{b0}		Si dangling bond defect types
ppO_2	mTorr	Partial pressure of O_2
ppO_3	mTorr	Partial pressure of O_3
ρ	gcm^{-3}	Si atom density
σ_p	cm^2	Hole capture cross section
τ_0	sec	Hole emission time constant ($\sim t_w/2.33$)
θ_c	degrees	Critical angle for internal reflection

Symbol	Units	Description
θ_H	AL	Surface Hydrogen coverage
q	C	Elemental Charge
Q_{inv}	C cm^{-2}	Inversion charge carrier density
ΔQ	C	change in depletion charge
S_p		Sticking probability
T	K	Temperature
t_p	sec	Pulse duration
t_w	sec	Sampling period
t_{ox}	nm	Gate oxide thickness
V_{ds}	volts	Drain-source voltage
V_{FB}	volts	Flat Band voltage
V_{gs}	volts	Gate-source voltage
V_R	volts	Reverse bias (volts)
V_{th}	volts	Threshold voltage of a transistor
V_p	volts	Bias pulse (depletion to accumulation pulse)
W	μm	Width of the transistor
x		Scaling factor
Y	eV	IPE Spectral Yield
$Y_{(channel)}$		Channeled back scattering Yield
$Y_{(rand)}$		Random back scattering Yield
$Y_{(surf)}$		Surface back scattering Yield

Chapter 1

Introduction

1.1 Physical scaling limits

The success of metal-oxide semiconductor field-effect transistor (MOSFET) devices is mainly attributed to their ability in scaling. For the past five decades, the physical dimensions of the transistor are scaled according to Moore's Law [1]. The scaling was not arbitrary and was explained by Dennard [2]. Enhanced performance, increased packing density, reduced power consumption and low cost per transistor are the motivations for scaling.

Consider a transistor, whose physical dimensions i.e., width (W), length (L) and gate oxide thickness (t_{ox}) are scaled by a factor of x (x > 1). Then the area of a transistor (W*L) is reduced by a factor of $1/x^2$ and hence the packing density is increased by a factor x^2. Scaling physical dimensions, necessitates scaling of operating voltages (V_{gs} and V_{ds}) to maintain a constant field in the device. Else, it leads to unacceptable leakage currents that in turn increase the power consumption. This is called the constant field scaling. Since the current scales with the voltage, the power (V*I) scales with the area of the transistor. As the physical dimensions are reduced, the gate capacitance is decreased by the factor of x, resulting in the decreased transition times. Thus the scaled transistor switches faster than an unscaled one. As the power dissipation is in proportion with the area, the power density remains constant for a scaled transistor. At present, down to 10 nm technology node with a printed gate length of 32 nm for high performance applications is reached [3].

Due to the short channel effects in a scaled transistor, the pace of scaling has been lowered beyond 28 nm technology node. The research on new materials

and novel CMOS architectures in maintaining the historical pace of scaling is extensive [4].

Thin-body transistor structures, such as planar ultrathin-thin body and buired oxide SOI MOSFETs [5], 3-D FINFETs [6] and gate all around nanowire MOSFETs [7] can mitigate the short channel effects due to their superior electrostatic integrity. However, these structures have significantly increased fabrication and/or design cost. The use of stressors below 45 nm technology node has saturated due to the reduced volume of stressor dimensions [8]. The alternative channel materials like Ge and III-V are promising, as they offer higher bulk mobility than silicon. However, the major bottleneck is the integration of these channel materials with suitable high-κ dielectric layers with sufficiently low electrical defect densities at and near the interface with the channel [9, 10].

Another approach is based on two dimensional (2D) materials, whose 2D nature provides extreme electrostatics with low dielectric constant for the overcoming short channel effects [11]. During the last decade, there has been extensive research on graphene in view of its remarkable transport properties [12, 13]. Yet the absence of a bandgap results in a low on-off current ratio which is at least one order-of-magnitude lower than the conventional Si technology. With time, there was a slow transition towards the silicon 2D counterpart called silicene, which circumvents graphene's gapless property by its buckled hexagonal atomic structure [14–16]. The fundamental problem with silicene is its instability in air [17], making it less promising for high-performance applications. Recently, other 2D layered materials such as transition metal di-chalcogenides (MX_2 – M is transition metal and X is chalcogen – MoS_2, WS_2) are gaining a huge interest, as devices show superior on-off current ratio at room temperature [18, 19]. However, the impediment is in obtaining high structural quality layers on a large area substrates [20–22]. **Hence most of the planar and the 2D materials encounter huge challenges before exploiting their properties for logic applications**.

1.2 Epitaxial Superlattices (SLs)

One of the alternative 2D technologies that could potentially overcome all of the above issues is **"Quasi-2D epitaxial superlattices (SLs)"** as schematically shown in Fig.1.1.

Quasi-2D Epitaxial SLs are composed of alternating periods of semiconductor (Si or Ge) layers and atomic layers (ALs) of hetero atoms (O,N or C). Recently, this concept is gaining momentum and is expected to provide a new opportunity to improve the electronic transport properties [23, 24]. The

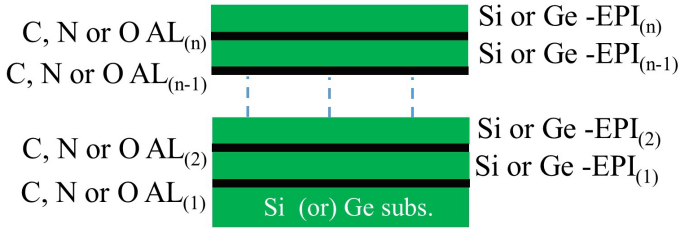

Figure 1.1: Schematic of quasi 2D epitaxial superlattices. It consists of alternating periods of semiconductor layers (Si,Ge) and atomic layers of hetero atoms (O,N or C). The "n" denotes the number of periods.

quasi-confinement, effective-mass engineering, change in valence band states and the dopant diffusion barrier are the paramount features of epitaxial Si-O SLs. These properties are capital for logical and optical applications. The physics of SLs is discussed below.

1.2.1 Physics of Epitaxial SLs

Effective mass Engineering and Wave function re-distribution

The SL consists of alternating periods of semiconductor (in this case **Si**) layers and atomic layers (ALs) of hetero atoms (e.g. **Oxygen**). The presence of O ALs in the Si channel cause multiple perturbations of the Si lattice potential. Fig.1.2 illustrates the schematic of 1 O AL inserted in Si channel and its potential distribution across its depth. The region with O layer has increased potential barrier where the charge carriers are blocked, while at the regions with periodic Si atoms, the charge carriers can leak through. This is called the **"Quasi confinement**. Thus the charge carriers are quasi-confined during their transport from source to drain.

1. The **effective mass of charge carriers is transformed to be anisotropic**. As the periodic symmetry of Si atoms across the channel direction is modified, the constant-energy ellipsoids of conduction band minima along {001} direction, shift to the zone center (in alignment with the valence band) and become anisotropic (Fig. 1.3). The transverse effective mass/tunneling effective mass (m_{zz}*) is increased in the gate direction and the longitudinal effective mass/transport effective mass (m_{xx}*) is reduced in the direction of transport. The enhanced m_{zz}* result

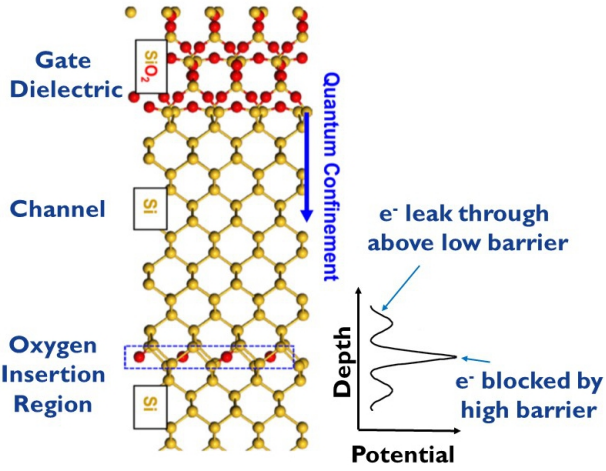

Figure 1.2: Schematic Si-O SL channel and the lattice potential perturbation across the channel direction [25].

in reduced gate leakage, while the reduced m_{xx}^* leads to the enhancement of charge carrier mobility.

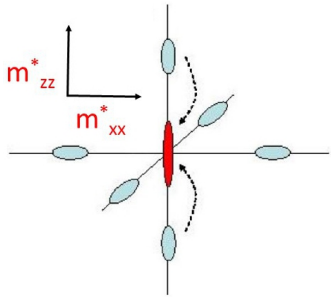

Figure 1.3: Effective mass band engineering with insertion of O ALs [26].

2. The inserted oxygen layers have been modeled as wide-band-gap layers whereby the resultant barrier height and width are fitting parameters [27]. For the inversion operation of a **n-MOSFET**, there is an increased separation between $\Delta 2$ and $\Delta 4$ sub-bands. This leads to an enhanced population of charge carriers at the lowest energy of $\Delta 2$ sub-band than $\Delta 4$ sub-band. Such **wave function re-distribution** results in **reduced inter sub-band scattering** and further enhancement of carrier mobility [27]. Fig.1.4b illustrates an increased population of inversion electron

density at $\Delta 2$ band by inserting O AL into the Si channel. For **p-MOSFET** the wave function of holes in the light-hole band is separated from the heavy hole band. As a consequence, the population of holes in heavy hole band is enhanced with reduced inter band scattering. [27]. Thus with the O inserted quasi confinement technology, the mobility of both electrons and holes are enhanced [25].

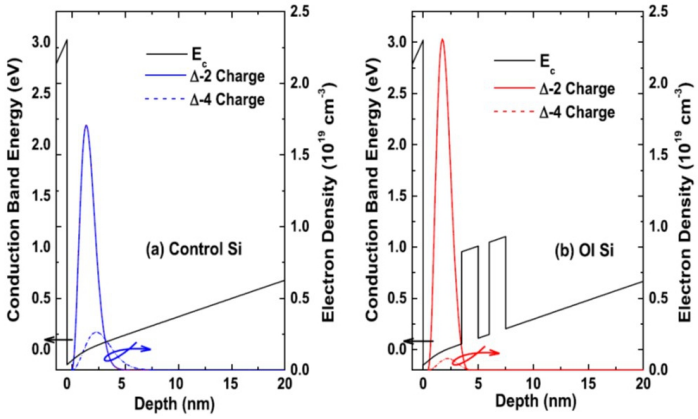

Figure 1.4: Simulated conduction band profiles of (a) Si channel (b) Si channel with inserted O ALs. The O ALs are modeled as wide-band-gap layers, enhancing the inversion electron density at $\Delta 2$ band (solid line) compared to the $\Delta 4$ band (dashed line) [25].

Shift of valence band edge with O ALs

Luo and co-workers have chemically designed the position of O layers in Si to shift the valence band edge of Si from the zone center ($\bar{\Gamma}$ to $\bar{Z}$). The O layer is placed in (8,1) configuration i.e. the bond structure consists of 1 AL of O atoms sandwiched between 8 ALs of Si atoms. The O atoms are placed at interstitial positions similar to the bond model shown in Fig.1.9. The insertion of O atoms at the given position has the following effect on the Si band structure as illustrated in Fig.1.5

The electronegative O atoms form a potential barrier that causes quantum confinement on the Si states. This will lower the energies of Si valence band (VB) states and increase the energies of the conduction band (CB) states, thereby increasing the band gap. If the O atoms are placed at the sites where the charge density is higher - then the quantum confinement effect is the largest. However the O atoms are placed at the sites where the charge density is minimum. This

results in lowering of the valence band maximum at $\bar{\Gamma}$ much more than at $\bar{Z}$ - in alignment with CB minimum resulting in a direct band gap (Fig.1.5b).

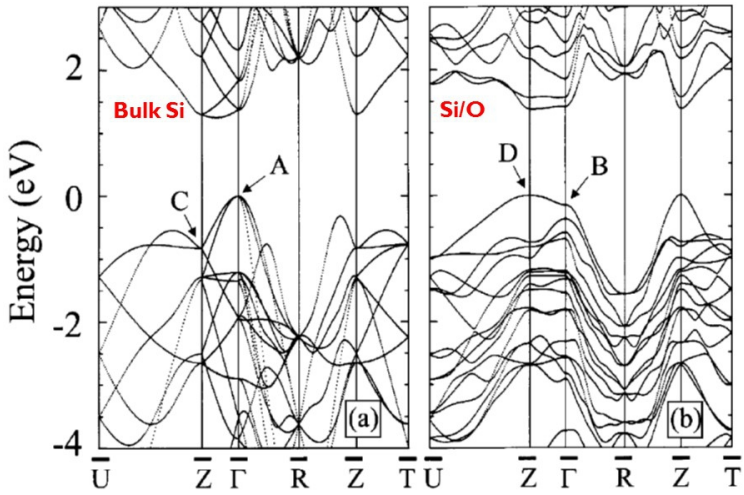

Figure 1.5: (a) Folded band structure of bulk Si (b) The band structure of (8,1) Si-O structure. The (8,1) indicates the 8 ALs of Si and 1 AL of O. The band structure was calculated using VASP and the pseudopotential codes using local density approximation [28].

1.2.2 Impact of heteroatoms

Among SL structures with different hetero atoms (Si-N, Si-C, Ge-N,Ge-C and Si-O), O based superlattice is chosen considering its structural stability and electronic properties.

The stability of the SL structures has been evaluated by computing the strain (lattice mismatch), induced by the hetero atoms in Si or Ge using density functional theory [29]. The computation was performed using quantum espresso package [30] based on the generalized gradient approximation for exchange correlation functional to obtain the quantitative insights on the ground state lattice parameters. As similar Si-O bond model,as proposed by Tsu *et.al* is shown in Fig.1.8 is considered for theoretical calculations [31].

1. Among different Si and Ge based SLs, the C and N structures result in large lattice strain (>4%) leading to the formation of either dislocations or other defects or even amorphization of the structures (Fig.1.6). Thus they are not studied.

2. Among O based SLs, **Si(Ge) atoms at 1+ oxidation state (One O atom at the Si(Ge) back bond)** result in **lattice strain less than 4%** compared to the SL structures with 2 O atoms at the back bonds (Si(Ge) atoms at 2+ oxidation state). The strain for the latter case varies from 5 to 35% depending on the direction of the measurement (Fig.1.6).

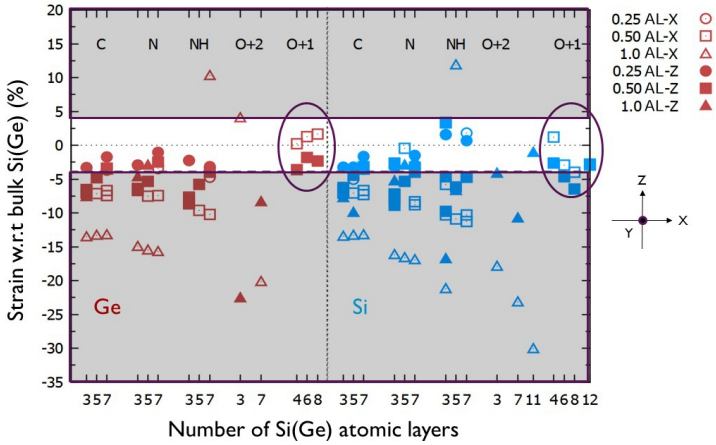

Figure 1.6: Evolution of strain computed with respect to the lattice constant of the bulk Si and bulk germanium. The number of layers used in the SL is labeled in the abscisse. The circle, square and triangle correspond to 0.25, 0.5 and 1 AL of hetero atoms introduced in the Si/Ge lattice. Filled and the empty symbols underline the strain along the X and Z axes of the superlattice [29].

Next, the electronic properties of these SL structures are considered in terms of their bandgap (Fig.1.7). As the density functional theory underestimates the band gap due to the poor description of non-local correlation effects, the hybrid exchange correlation functional [32] is considered. This approach has been shown to provide band gap values close to the experimental results.

1. The N and C based SLs are not considered, as the structures yield lattice strain greater than 4%. In addition, N based superlattices have zero bandgap (Fig.1.7).

2. For Si-O based superlattices, the Si atoms with 1+ oxidation state (1 O atom at Si back bonds) have band gap close to the bulk Si. While the structure with Si atoms at 2+ state (2 O atoms at Si back bonds) is ignored due to the larger variations in the strain.

3. For Ge–O based superlattices, the Ge atoms with 1+ oxidation state (1 O atom at Ge back bonds) have a band gap close to half of bulk Ge, while structures with 2 O atoms in Ge back atoms are ignored due to the larger strain in the structure.

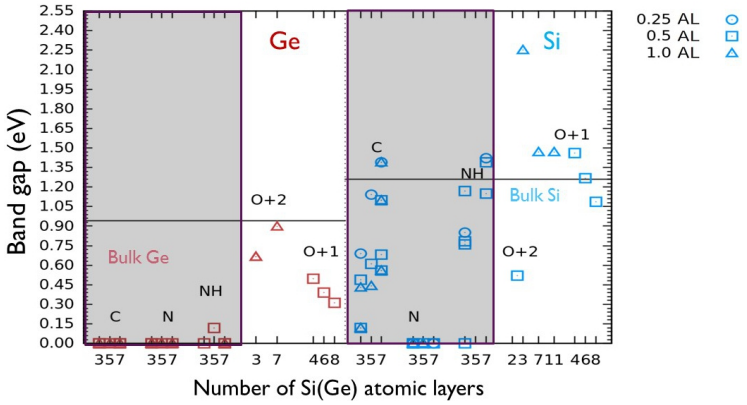

Figure 1.7: Evolution of electronic band gap computed with respect to the number of Si (blue) and Ge (red) layers. The horizondal line correspond to the bulk Si and Ge band gaps. All the computation have been carried out using Tran-Blaha exchange correlation functional [29].

Thus by considering the lattice strain due to the hetero atoms in Si(Ge) and the electronic bandgap, Si(Ge)-O SLs with Si(Ge) atoms at 1+ oxidation state are promising.

1.2.3 Si-O bond structure

In literature, different Si-O bond structures are proposed and are described below,

Tsu bond model

Structure: Tsu and his co-workers have proposed a Si-O model as shown in Fig.1.8. The hand built models are constructed considering a minimum structural strain. The bond length of Si–Si (0.235 nm) and Si–O (0.166 nm) are fixed, while the bond angles are varied to have an optimal geometry.

1. The first model is called the **Tsu/lofgren model**, whereby two O atoms are located at the interstitial position in [010] direction. The bond bending strain (Si–O–Si) and the stretching strain in the overall structure with the optimized geometry is ∼6.4% and ∼6.2% respectively (Fig.1.8a).

2. Another model is called the **Mirror model**, whereby the Si atoms are mirror imaged considering the O layer as the plane of reflection. With flexible O–Si–O and Si–O–Si bond angles, the in-plane strain is calculated to be ∼9% (Fig.1.8b).

O-content: 1.4×10^{15} atoms cm^{-2} (∼ 2 AL)

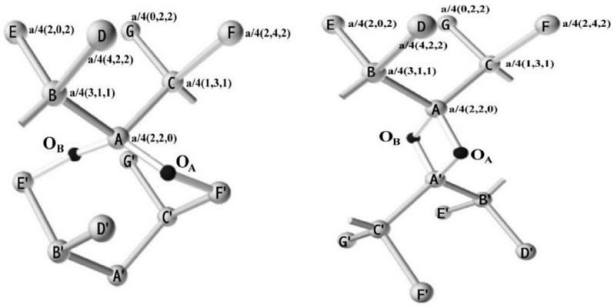

Figure 1.8: Hand built structures of Si-O interface in crystalline Si-O SL as proposed by Tsu. (a) Tsu/Lofgren Model with O atoms placed at (010) direction and (b) Mirror model, where the O layer is considered as the plane of reflection. The grey atoms are Si and black are O atoms [31].

Mears model

Rober J Mears has pioneered in Si-O SL technology and has patented his process flow, choice of precursors and the integration approaches.
Structure: He proposes that the O atoms are placed interstitially (Fig.1.9), to minimize the distruptions in the Si lattice and to not hinder subsequent epitaxial ordering of Si [33–37]. The O atoms at non-substitutional sites between the Si–Si bonds is also considered to be thermodyanmically meta-stable and can withstand high thermal budgets during CMOS processing [25].
O-content: 6.7×10^{14} atoms cm^{-2} (∼ 1 AL)

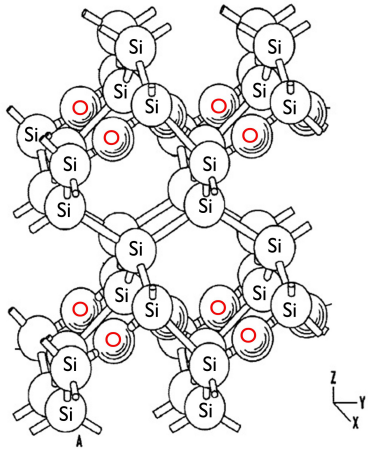

Figure 1.9: The atomic diagram of Si-O bond in a SL structure as proposed by Mears. The O atoms are placed at interesititial positions between Si – Si bonds. The O and the Si atoms are indicated [34].

Nishio model

Recently, Nishio *et.al* have compared the above bond structures and proposed two new Si-O structures resulting in low formation energies and reduced structural strain. These structures are promising with an anisotropic effective mass as required for the electron and hole mobility enhancements. They are summarized below.

Structure: The Nishio model of the Si-O bond structures is shown in Fig.1.10(a) and (b). The **Rec-I** model is constructed by connecting the reconstructed Si surfaces with Si – O – Si bridges. The amount of O-content in these structures is close to 1 AL (6.78×10^{14} atoms/cm^2). The **Rec-II** is tuned to have higher oxidation states with additional O atoms at the Si dimers. The amount of O-content in these structures is close to 2 AL. For the sake of comparison other Si-O bond models are indicated in Fig.1.10 (c) and (d). The notations I and II indicate the oxidation state of the Si atoms at Si-O-Si interface.

The stability of the structures was evaluated by calculating the formation energy per O atom. As seen from the Table.1.1, the formation energy is lowest for the Rec-II structure followed by the Rec-I structure. The Luo-II and Tsu-II models have higher formation energies, illustrating less stable structures. To further demonstrate the advantage of these structures, strain along unit cell vectors in [110], [$\bar{1}$10] and [001] directions are evaluated. The lattice mismatches

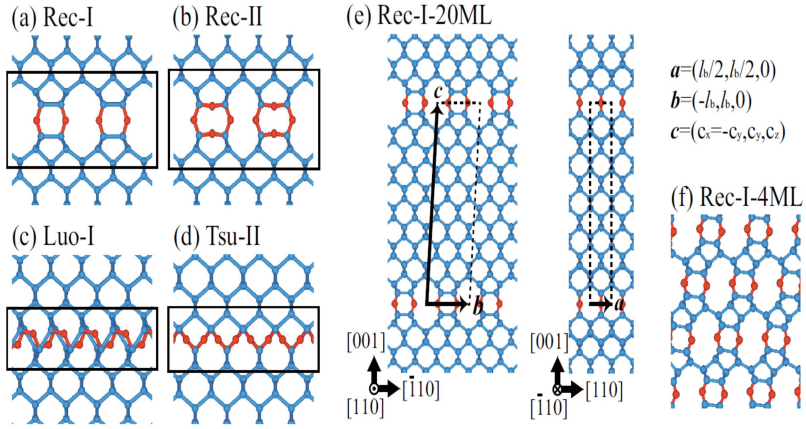

Figure 1.10: (a) Rec-I (b) Rec-II (c) Luo-I model same as () (d) Tsu-II same as Fig.1.8 (a). The (e) has a similar structure 20 ALs of Si between the O layer. The notations I and II indicate the oxidation state of the Si atoms [38]. The Si and O atoms are indicated in blue and red respectively.

of the Rec-I and Rec-II interfaces are at most 2.7%. On the other hand, the Luo-I interface has a mismatch of 8.6% along the b direction. This originates from the fact that the O atoms are forced into Si−Si bonds of the diamond structure. The Tsu-II interface has a mismatch of -18.6% in the angle made between the a and b unit cell vectors. These illustrate that the Rec-I and Rec-II demonstrate a higher stability than the so far proposed Si-O interfaces.

	f(eV/atom)	ϵ_a (%)	ϵ_b (%)	ϵ_c (%)
Free standing Rec-I 4 AL	-3.67	0.0	-1.5	0.0
Free standing Luo-I 4 AL	-3.19	-0.2	8.6	0.0
Free standing Rec-II 4 AL	-4.09	2.5	2.7	0.0
Free standing Tsu-II 4 AL	-3.52	4.9	4.9	18.6

Table 1.1: The formation energy (f in eV/atoms) and lattice mismatches calculated for differnt bond models. ϵ_a = (a-a_0/a_0). The a, b and c are the cell vectors along [110] ,[$\bar{1}$10] and [001] directions [38].

Though different Si-O interface bond models are proposed/theoretically evaluated, the experimental verification of bond structures for high mobility applications is not known. A well defined O-content and a controlled bond structure is required to realize band engineered Si-O SLs. This demands a fundamental study on the surface chemistry between O precursors and the Si(100)

substrate to understand the possible surface structures upon chemisorption. Next, the impact of O bonding structure on the epitaxial ordering of Si thereon needs to be understood. Unlike conventional Si homo-epitaxy where O atoms are considered as contamination, Si epitaxy has to be grown on O AL with minimum structural defects. One requires a thorough understanding on the Si kinetics for the epitaxial growth of Si on O AL.

Hence the section below will review the surface chemistry of O_3 and O_2 on H–Si(100) for the deposition of O AL and the kinetics of Si epitaxy for enabling epitaxial ordering of Si on O AL.
O-content: Rec - I = 6.7×10^{14} atoms cm^{-2} ($\sim$ 1 AL) and Rec - II = 1.4×10^{15} atoms cm^{-2} ($\sim$ 2 AL).

1.3 Surface chemistry for the deposition of O atomic layer (AL)

This section describes the initial stages of Ozone (O_3) and molecular Oxygen (O_2) chemisorption reactions on H-terminated Si for the deposition of O AL.

The distinction between the oxidation of silicon and deposition of O ALs is first clarified. The conventional thermal oxidation of silicon requires high temperature, whereby the O atoms diffuse into the Si lattice to form SiO_2. The Si atoms are predominantly in the Si^{4+} state. In contrast, during the deposition of O AL, the O atoms are chemisorbed on the surface and their bonding is effectively limited to the top 1-2 atomic layers of Si. The surface Si atoms are expected to be at the Si^{x+} (x < 4) oxidation state. This mandates a low temperature processes for limiting O diffusion into Si.

Choice of precursors: There are several oxygen sources like H_2O [39, 40], N_2O [41], O_2 [42] and O_3 [43], suitable for the deposition of O AL. There are two constraints to be considered before deciding on the choice of O precursor

1. Low temperature deposition is required to limit O diffusion in Si.
2. The Si surface prior to the deposition of O AL should be H-terminated, to avoid the interaction with ambient oxygen and/or with residual O contamination during processing.

The reaction of H-terminated Si with an O_2 molecule exhibits a higher activation energy of 0.3 eV and requires T > 290°C for chemisorption due to H abstraction from H–Si(100) [44]. The H_2O is considered to have similar

reaction rates to O_2 and does not react with H−Si(100) at low temperatures [45]. The chemisorption of N_2O on Si(100) at 300 K yields O atoms at dimer positions of 2×1 Si(100), which could be a potential candidate for the deposition of O AL [41]. However the reaction mechanism of N_2O on H−Si(100) is not yet known and therefore requires extensive investigation.

Amongst the above precursors, O_3 has a low activation energy and can chemisorb on H−Si(100) at low temperatures [43, 44, 46]. Hence the kinetics of O_3 surface reaction is investigated for the deposition of O AL. In addition to O_3, O_2 is also investigated for the deposition of O ALs at higher temperatures on H−Si(100). The motivation is to understand the impact of O precursors on the surface structures after its exposure on H−Si(100).

1.3.1 O_3 reaction on H-Si(100)

Fig.1.11, provides an atomistic insight in the surface reaction of O_3 on H−Si(100) using molecular dynamic investigation.

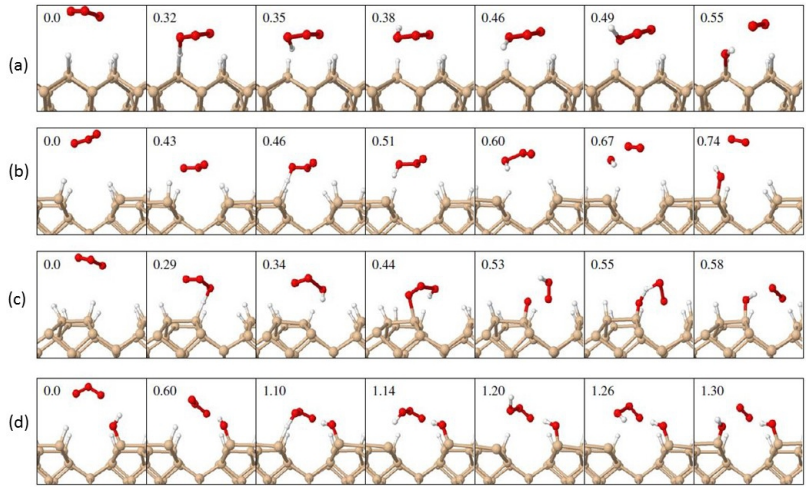

Figure 1.11: Molecular dynamic trajectories revealing how O_3 abstracts the surface hydrogen to form Si−OH. The thermal velocity of O_3 is 5 Å ps^{-1}. The trajectories (a)-(c) illustrate different dissociation pathways. The (d) describe the pathway with a preexisting surface Si−OH [46].

The reaction between O_3 and the surface hydrogen proceeds by an intricate radical-mediated adsorption mechanism, which enables O_3 to oxidize the Si−H bond (Fig. 1.11). O_3 abstracts a surface hydrogen atom and forms a $HO_3^{\bullet}$

radical. Due to the close proximity of an unpaired silicon surface dangling bond, which was created during the H-abstraction, the $HO_3^{\bullet}$ species exhibits only a short lifetime and binds to the surface dangling bond. Next, the adsorbed HO_3Si dissociates into surface hydroxyl (Si–OH) and the gaseous O_2.

The surface reaction of O_3 on H–Si(100) at a thermal velocity of 5 Å ps^{-1} is summarized in Fig.1.11 (a)-(c) and in Fig.1.12. The different reaction pathways ultimately lead to the same reaction product of gas-phase O_2 and a surface hydroxyl (Si–OH) [47]. In the case of partialy oxidised Si (Fig.1.11(d)),O_3 abstracts the H only from H–Si sites and the existing hydroxyls substantially enhances the likelihood for the further formation of surface hydroxyls [46]. This results in an uniform atomic layer of surface hydroxyls. The O_3 reaction mechanism proposed by Fink [46] is in partial agreement with the experiments by Cui *et.al*, where the detection of 1727 cm^{-1} IR peak corresponds to the O_3 adsorbed species [44]. Nevertheless, the complete reaction mechanism has not yet been fully verified through experiments.

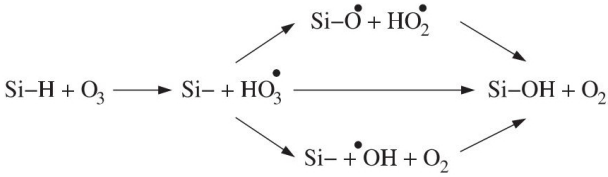

Figure 1.12: The surface reaction pathways for the initial oxidation of H-terminated Si(100) with O_3 via the $HO_3^{\bullet}$ radical intermediate [47].

In contrast to the above observations, Kurokawa concluded that the three backbonds of a Si atom are changed to Si–O–Si bridges simultaneously when the O_3 reaction proceeds on the hydrogen passivated surface. The observations are concluded by monitoring the O-1s and Si-2p XPS spectra as a function of the O_3 exposure [48].

To conclude, different reaction mechanisms and surface structures are proposed in litreature. The experimental verification of the possible surface structures after O_3 chemisorption is lacking and will be the subject of this PhD research.

1.3.2 O_2 reaction on H-Si(100)

The O_2 is less reactive on H–Si(100) as compared to O_3. The activation energy for O_2 reaction is 0.3 eV, which is an order of magnitude higher as compared to the O_3 reaction (0.05 eV) [49]. This necessitates a higher

temperature for surpassing the energy barrier. Fig.1.13 illustrates the molecular dynamic simulation of the O_2 reaction on H−Si(100). At a temperature of 500 K, the Si atoms of the dimers oscillate in a coordinated fashion resulting in change of bond angles. The dimer oscillations coupled with Si−H vibrations lead to a weakening of Si back bonds with an increase in Si−Si bond length from 2.32 to 2.42 Å. This disruption of bond lengths and bond angles facilitates O_2 dissociation and insertion of the O-atom in the Si−Si back bond. The reaction is highly exothermic with a reaction enthalpy of -8 eV (Fig. 1.14). The incorporation of O weakens the neighboring bonds guiding the insertion of a second O-atom (-10 eV) in the back bond of same Si atom. Finally, once all the back bonds are occupied, the disruption of the surface periodicity guides O atom insertion in the Si−H bond leading to the oxidation of Si(100).

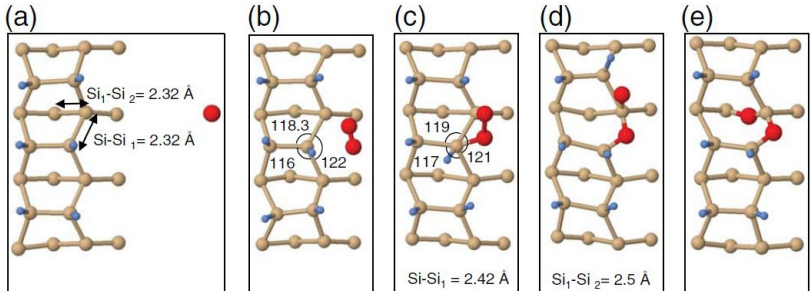

Figure 1.13: Molecular dynamic simulation of O_2 reaction at 500K followed by a O atom insertion in the Si back bonds of H−Si(100) [42].

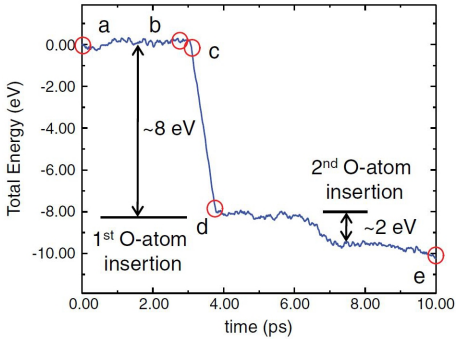

Figure 1.14: The total energy as a function of time during the molecular simulation of O_2 on H−Si(100) as described in Fig.1.13. [42].

1.4 Si epitaxy by chemical vapor deposition (CVD)

1.4.1 Si template and impact of pre-epi clean

The word epitaxy is coined from Greek ($\epsilon\pi\iota$ + $\tau\alpha\xi\iota$s) meaning "upon + to arrange". Epitaxy refers to the deposition of a crystalline material on top of an other crystalline material, such that the ordering and orientation of the underlying material (substrate crystal) is continued to the grown layer (epitaxial layer). If the epitaxial layers either forms a random orientation with respect to the substrate or does not form an ordered overlayer, it is termed as non epitaxial growth. If the epitaxial film is deposited on a substrate of the same composition, the process is called homo-epitaxy. The schematic is shown in Fig.1.15.

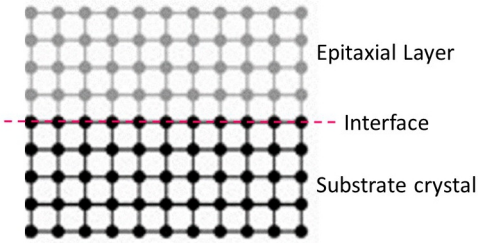

Figure 1.15: Schematic of an epitaxial layer with similar orientation and ordering as the substrate crystal. The black and gray dots in the figure are the Si atoms from substrate and epitaxial layer respectively.

Impact of pre-epi clean: The presence of interface contamination (O and C) affect the Si epitaxial quality by generating defects. The consequences of O contamination due to a poor pre-epi clean are summarized below

1. Finch *et.al* have demonstrated that stacking faults are generated due to the presence of SiOx patches at the interface. They are schematically shown in Fig.1.16. The patches of oxide can produce atomic steps at the substrate surface. The height of the steps may not be equal to the integral multiples of Si interplanar spacing. Now, when a Si layer is forced to grow on top of such steps, the lattice coherence is maintained by the formation of stacking faults [50].

   The above concept was experimentally observed by Matty Caymax. The Fig.1.17 shows the TEM image of epitaxial Si on Si(100) with the patches of oxide at the interface. It is clearly noticed that the regions between oxide patches are the nucleation sites for the epitaxial ordering, while the

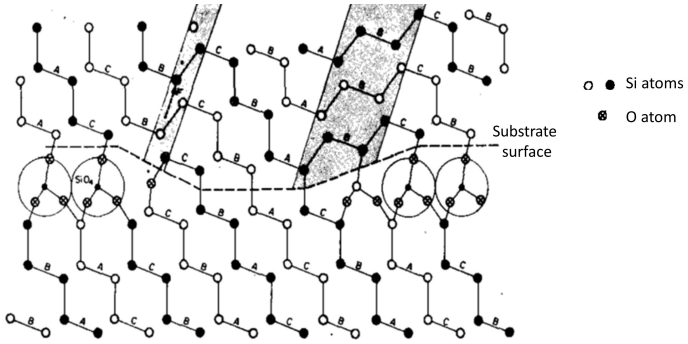

Figure 1.16: Schematic of stacking fault generation due to the presence of O patches at the epitaxial Si/Si(100) substrate interface. The complete black and white atoms are Si and the shaded are O atoms [50].

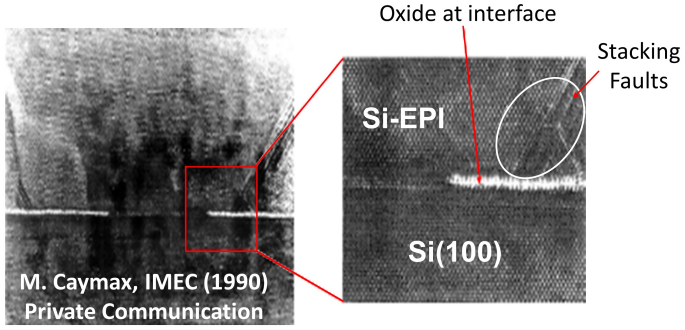

Figure 1.17: Stacking fault defect types occur at epitaxial Si/Si(100) interface due to the presence of patches of oxide. *TEM image is used with the permission from Matty Caymax, IMEC* [51].

stacking faults are detected in the regions directly above the oxide patches [51].

2. Gruhle *et.al* have shown that, for partial pressure of O_2 greater than 15×10^{-6} mbar, the epitaxial quality of Si is degraded with a rough surface morphology and surface defects. In addition, the quality of metal-Si Schottky diodes are degraded with ideality factor greater than 1.5 [52].

3. In addition to the structural defects, the O contamination lead to a non-radiative recombination of electron/hole pairs (excitons) and reduced the life time of minority charge carriers [53].

1.4.2 Si CVD Kinetics

The objective of this section is to review the elementary steps of Si CVD process and to determine the step controlling the deposition rates.

The overall chemical reaction of the Si CVD process using SiH_4 is given by equation 1.1.

$$SiH_4\,(g) \longrightarrow Si\,(s) + 2\,H_2\,(g) \tag{1.1}$$

The Si deposition process involves several elementary steps as schematically shown in Fig.1.18. The separation of the gas phase and surface reaction steps is an useful approach in describing the Si CVD chemistry. The gas phase reaction determines the fluxes of various species to the growth surface and the subsequent chemistry at the surface incorporates the Si adatoms into the growing film. The reaction by-products are desorbed enabling the dynamics of the deposition process.

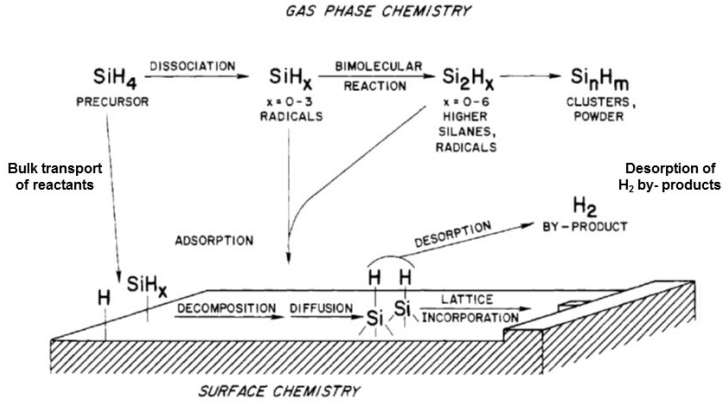

Figure 1.18: The surface hydride chemistry and the kinetics of a Si CVD film growth [54].

Bulk transport of reactants to the wafer surface

The first step is the transport of reactants by forced convection to the deposition region. The reactants diffuse from the main gas stream through the boundary layer to the wafer surface. The flux of the reactant species reaching the

wafer surface is the difference in concentration of the reactant species between the main gas flow and the wafer surface times the mass transfer coefficient[55].

Surface Adsorption

Once the reactants arrive at the wafer surface, they diffuse through the boundary layer and get adsorbed on the surface. The adsorption process depends on the pressure of the reactor. At very low pressure systems (e.g. UHVCVD - ultra high vacuum CVD), the gas-phase collisions between the molecules are unlikely and the molecular decomposition of SiH_4 will not occur. On the other hand, for high pressure systems (APCVD - atmospheric pressure CVD), the collisions and the SiH_4 decomposition in the gas phase are dominant. According to the kinetic theory, for low pressure systems the reactant flux of SiH_4 (F_{SiH_4}) striking the surface per area, per time is given by equation 1.2

$$F_{\mathrm{SiH_4}} = \left(\frac{N_{\mathrm{A}}}{2\pi k T M_{\mathrm{SiH_4}}}\right)^{0.5} \times p_{\mathrm{SiH_4}} \quad [cm^{-2}s^{-1}] \tag{1.2}$$

N_A is the Avagadro's number (6.022×10^{23} mol^{-1}), M_{SiH_4} is the molar mass of SiH_4 (32.11 $gmol^{-1}$), k is Boltzmann's constant (1.38×10^{-23} JK^{-1}), T is the absolute temperature and p_{SiH_4} is the partial pressure of SiH_4 (Pa). The rate of SiH_4 adsorption is evaluated in terms of sticking probability (S_p), i.e. the number of dissociatively adsorbed SiH_4 molecules reacted per molecule-surface collision. The S_p is measured from the slope of molecules adsorbed versus exposure. The S_p depends on the surface H-coverage (θ_H) and temperature [56, 57]. Hence the rate of adsorption per area (r_{ads}) is given by equation 1.3.

$$r_{\mathrm{ads}} = F_{\mathrm{SiH_4}} * S_p(\theta_{\mathrm{H}}, T) \quad [cm^{-2}s^{-1}] \tag{1.3}$$

SiH_4 Decomposition

Upon adsorption, the next step is the decomposition of SiH_4 into SiH_x surface species [58]. The decomposition of SiH_4 is sequentially shown in equations 1.4 - 1.8 [59]. The SiH_4 requires two dangling bonds to decompose into $\underline{Si}H_3$ and $\underline{H}$ (equation 1.4). The atom occupying the surface dangling bond is denoted as $\_$. At the deposition temperature of 400-500°C, $\underline{Si}H_3$ and $\underline{Si}H_2$ are unstable and readily decompose into $\underline{Si}H$ - mono-hydrides (equation 1.5 and 1.6). The $\underline{Si}H$ is further decomposed into atomic Si, which is now called the Si adatom (equation 1.7 - 1.8). The dangling bonds generated after H_2

desorption are required back for further SiH_4 adsorption process (equation 1.4). These dynamic processes lead to the growth of the Si film.

$$SiH_4\,(g) + 2\,\_ \longrightarrow \underline{H} + \underline{Si}H_3 \tag{1.4}$$

$$\underline{Si}H_3 + \_ \longrightarrow \underline{H} + \underline{Si}H_2 \tag{1.5}$$

$$2\,\underline{Si}H_2 \longrightarrow H_2\,(g) + 2\,\underline{Si}H \tag{1.6}$$

$$2\,\underline{Si}H \longrightarrow H_2\,(g) + 2\,\underline{Si} \tag{1.7}$$

$$\underline{Si} \longrightarrow Film + \_ \tag{1.8}$$

H_2 Desorption

The by-products of reaction 1.7 lead to the desorption of molecular H_2. Theoretically the rate constant for the desorption is thermally activated and is given by

$$k_{des} \sim \nu_{des}\; exp^{(-E_{des}/kT)} \tag{1.9}$$

where ν_{des} is attempt frequency and the E_{des} the activation energy for desorption. Different reaction mechanisms have been studied by using first principles [60], temperature programmed desorption and laser induced thermal desorption techniques [61, 62]. The H_2 desorption (equation 1.7) has a first order reaction behavior [62, 63]. Two hydrogen atoms from the same dimer undergo pairing and then desorb. Later it was investigated that, the H_2 desorption from the same dimer has large activation energy ($E_{des} \approx 120$ kcal/mol) and is unlikely. Instead, the H_2 desorb from two paired H atoms on the same side of two adjacent silicon dimers in the same row. This is considered to be the dominant mechanism [64].

Surface Diffusion

Once the SiH_x surface species are decomposed into Si adatoms, they are incorporated into the Si lattice by surface diffusion (equation 1.8). The Si

adatoms diffuse by 2D Brownian motion on the substrate surface. There are two possibilities in which the Si adatoms are incorporated into the Si lattice. The adatom meets an another adatom, forming a stable nucleus **(nucleation)**, or meets an existing island, thereby contributing to the **Si film growth**. The diffusion coefficient is determined by relation 1.10

$$D \sim (a_0)^2 \nu \; exp(\frac{-E_{\text{diff}}}{kT}) \;\; [cm^2 s^{-1}] \tag{1.10}$$

where a_0 is the inter-atomic distance, ν is the attempt frequency (10^{12} - 10^{13} s^{-1}) and E_{diff} is the activation barrier for the surface diffusion of Si adatoms. D also determines the outcome of the competition between the Nucleation and the Si growth process. The larger diffusion coefficient for instance, means a higher probability for an arriving adatom to find an existing island before another adatom is deposited in its vicinity to provide a chance for nucleation. Thus the island density is related to D. The D can also be experimentally measured using Scanning Tunneling Microscopy (STM) [65].

Si Growth rate determining step

In conventional CVD there are two growth regimes, mass transport limited of the reactants and the surface reaction rate limited. The former occurs at high temperatures and the latter occurs at low growth temperatures.

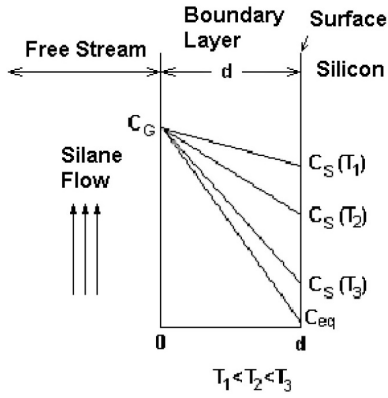

Figure 1.19: Silane flow concentration in a free stream (x=0) and on the Si surface (x=d) at different temperatures (T1>T2>T3) [66].

Figure 1.19 is used to understand the Si CVD kinetics, illustrating the change in silane concentration above the wafer surface at different temperatures.

On the x-axis, the 0 represents the interface between the gas-free stream and the boundary layer. The d represents the thickness of the boundary layer between the silicon surface and the gas stream. The concentration of the gas at free stream is denoted as C_G. The gas of C_G concentration diffuses through the boundary layer of distance d and reaches the wafer surface. The concentration of gas on the surface (C_S) is dependent on the deposition temperature. As the temperature increases, the surface reactions occur more readily and hence a decrease in C_S (i.e. $C_S(T3) < C_S(T2) < C_S(T1)$). When the temperature is high enough, the C_S is nearly zero, illustrating that the gas molecules reaching the surface reacts immediately. The diffusion rate across the boundary layer is weekly dependent on the temperature.

On the other hand, the surface reactions typically increase exponentially with temperature in an Arrhenius fashion. Thus at high temperature, the growth rate is limited not by the surface reactions on the growing surface, but by the diffusion of the reactants through the boundary layer. This is known as the mass transport regime (Fig.1.20). As the temperature is reduced, the surface reaction decrease faster than the diffusion through the boundary layer and hence the surface concentration increases with decreasing temperature. Thus the growth rate at low temperature is not dominated by the gas flow but the surface reactions. This is called as the kinetic regime.

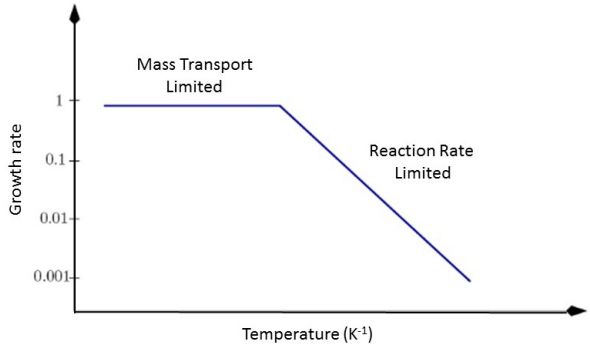

Figure 1.20: Arrhenius plot of growth rate versus 1/T for CVD process. The net growth rate is the result of the surface reaction and gas phase mass transfer processes acting in series so that the slowest of the two dominates for the given temperature.

1.5 Potential applications of Si-O SLs

High mobility Channel

The primary application, where one can exploit the sub-band engineering with reduced transport effective mass (m^*_{xx}) and a lower sub band scattering is to obtain **high mobility Si devices**. Until today, only the research group from Mears has pioneered in demonstrating the higher carrier mobility (both electrons and holes) with Si-O SL channel compared to the conventional Si channel [25, 27].

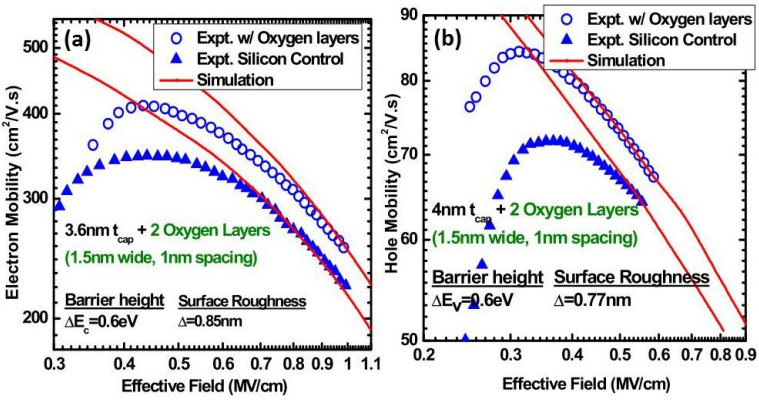

Figure 1.21: The enhancement in (a) electron mobility and (b) Hole mobility after inserting O ALs in the Si channel. Two period of Si-O SL with Si of 1.5nm thick and the top Si layer is 3.6nm thick. The red lines are simulated values of mobility after considering the phonon and surface roughness scattering mechanisms [27].

The simulation results in Fig.1.21 indicate that one can predict on a enhancements in Si hole mobility by inserting O ALs in Si with a confinement barrier of 0.6 eV. In Fig.1.21a, the steeper slope of the mobility with O ALs compared to conventional Si at low fields is the result of reduced impurity scattering due to the formation of a super steep retrograde well doping profile. As the Raman and the Rutheford back scattering-channeling measurements confirm negligible strain in Si-O SL, the latter cannot be explained for mobility enhancement [25]. However, as a consequence of the quasi confinement, the wave function is re-distributed resulting in low sub-band scattering. Thus the **Quasi confinement, SSRW profile and reduced inter sub-band scattering** are responsible for the observed mobility enhancement up to 30% in Si-O SL structure compared to the conventional Si.

Moving from the planar to non-planar technologies, a quasi confinement technology with the introduction of O AL is suggested for FINFETs [27]. As the carrier confinement in ultra thin channel along (110) direction is beneficial for holes [67], p-channel FINFETs are proposed as shown in Fig.1.22. The Si-O FINFETs are patented and are yet to be realized experimentally [33].

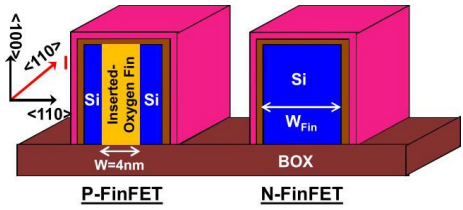

Figure 1.22: Schematic of implementing O AL inserted quasi confinement in FINFETs [24].

Optical Activity

In addition to the logical applications, Si-O SL are exploited for optical applications. As Si is an indirect band gap material, it requires phonon assistance for optical transitions. The intensity of such transitions is three orders of magnitude weak is as compared to direct optical transitions. Therefore researchers explore engineered Si structures such as Si quantum dots, clusters of Si in oxide matrix [68] and porous Si [69] for direct optical transitions.

Photoluminescence Properties: Several years ago, crystalline Si-O SLs were proposed as a barrier for Si quantum devices [70]. The O ALs sandwiched between epitaxial Si layers provide a barrier for **quantum confinement**. Such confinements induce direct optical transistions around 1.9 eV as shown in Fig.1.23c, [71, 72] i.e. optical transitions at a band gap greater than the Si band gap. In addition, a transition at 2.15 eV and 2.2 eV is speculated to be due to the **Si-O complex** [73]. The intensity of such sharp transitions is degraded during the anneal at 850°C for 30min, illustrating that the oxygen may have diffused into a different arrangement (dashed lines in Fig.1.23c).

An other possible mechanism that can explain the optical properties of Si is based on the defect engineering where by the O atoms **chemically shift the valence band edge of Si away from the zone center** [28]. The desired O bonding configuration and its corresponding changes in the band structure are discussed in the section 1.2.1.

Electroluminescence Properties: Electroluminescent (EL) properties are demonstrated using crystalline Si-O SLs as active layer in a conventional Si-O

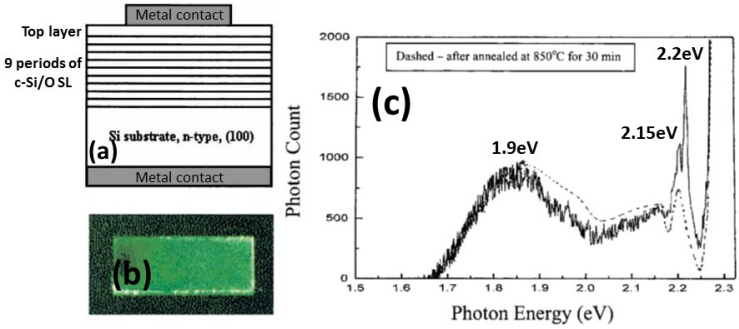

Figure 1.23: (a) Schematic of a EL diode with 9 period Si-O SL as an active layer (b) EL through the top Au electrode, emitting light in the yellow-green region (c) PL spectra. The transition at 1.9 eV is due to the qunatum confinement, while the transitions at 2.15 and 2.2 eV are speculated due to the formation of Si-O complex. The change in Si-O bond structure with anneal result in reduction of optical intensity at 2.15eV. [73].

Schottky diode (Fig. 1.23a) [31, 73]. During the reverse bias operation, the electrons are injected across the Schottky barrier. The injected hot electrons generate holes by avalanche in the active SL region and these holes in-turn participate in electron - hole recombination in the yellow-green region of the visible spectrum (Fig.1.23b), [74, 75]. The EL device after the passivation of dangling bonds demonstrate higher EL intensity without any degradation up to one year. Thus the stability of the crystalline Si-O SLs has a promising scope for integrated circuits and optics.

Alternative for SOI

Recently, it was shown that the Si-O SL can serve as a fully epitaxially grown insulating layer and as such as a possible replacement for Silicon on Insulator (SOI) [76]. Au-Schottky diodes with 5 periods Si-O SLs were fabricated and the Current - Voltage (I - V) characteristics were measured (Fig.1.24). Up to a bias of -60 V, **no breakdown** was observed indicating that the multilayer SL act as an epitaxial insulating barrier withstanding large electric fields in the direction perpendicular to the O ALs. Thus the electrical isolating behavior of SLs can be capitalized upon by fabricating devices on top of each other, ultimately realizing three-dimensional integrated circuits [77].

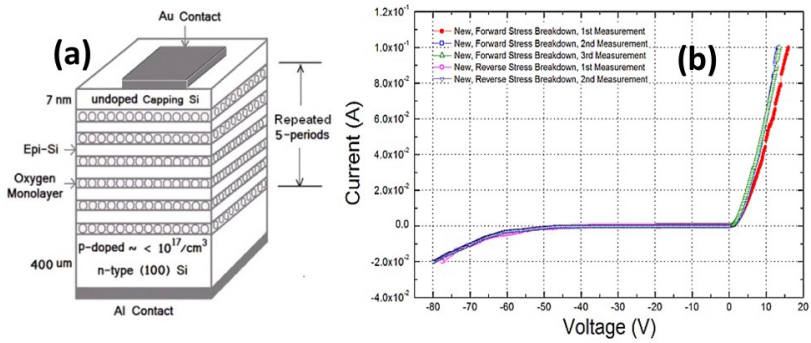

Figure 1.24: (a) Schematic of a Si-O SL Schottky diode with 5 period Si-O SL (b) I - V characteristics illustrating no breakdown during its reverse bias operation up to - 60V. This signifies the Si-O SL as an epitaxial insulating barrier used for isolating the devices [77].

Other Si based SLs

Other semiconductor/hetero atom SLs are well studied in the literature and are briefed below.

Si-N SLs: Nitrogen based SLs have been investigated by atomically controlled processing [78]. The epitaxial ordering of Si can be continued on N layers with the N-content of 3×10^{14} at/cm^2 or lower after a certain incubation period. The N-content higher than 3×10^{14} at/cm^2 cause amorphous Si due to the formation of Si_3N_4 at the interface. **Such δ doped Si layer with N act as donors, whose concentration increases with N-content up to 1×10^{14} at/cm^3. The measured Hall mobility is higher than that of the uniformly P doped Si with P concentration of 10^{19} cm^{-3}.** In addition, there is a possibility that the carrier mobility is enhanced by highly condensed strain near the N AL doped region. Since N atoms tend to diffuse, and part of them can segregate close the surface at 750°C, applications into device fabrication requires low thermal budget processing [79].

Si-P SLs: The atomic layer doping with P is promising for reducing the contact resisitivity between the metal and Si. At a low temperature of 450°C and a rather high partial pressure of SiH_4 (say 220 Pa), P incorporation into the Si film and the growth of Si film thereon have been achieved without any incubation period [79]. However the P concentration tailing towards the surface is observed as the P atoms segregate or desorb during the Si growth. A average P concentration of 6×10^{20} cm^{-3} is deposited with 7 nm of Si spacing between [80]. The average carrier concentration is as high as 3.6×10^{20} cm^{-3} and

the resistivity is as low as 2.7×10^{-4} Ω.cm. Such atomic layer doping technique with a very low contact resistivity of about 5×10^{-8} Ω.cm^2 is achieved between Ti and Si [81].

1.6 Problem statement

Theoretically, the Si-O SL technology is promising for the enhancement in the carrier mobility through effective mass engineering. Can we achieve such mobility enhancements through dedicated experiments?

1.7 Scientific research questions

The following research questions are encountered to understand the growth, structural and electrical properties of epitaxial Si-O SLs.

1. Oxygen atoms are usually considered as contamination and are avoided during epitaxy. However in SLs, the O layers are sandwiched between epitaxial Si layers. Thus the fundamental question to be answered is which O surface species can allow Si epitaxy? How do these O structures differ from O contamination that can result in Si deposition into defective epitaxial or poly-crystalline or amorphous?

2. Once the required O surface structure for the epitaxial Si deposition is known, what is the epitaxial seeding and nucleation mechanism for the Si growth on O AL? What is the impact of O-content and different O surface structures on the epitaxial quality of Si on O AL (Si/O AL)?

3. Once the process for the epitaxial Si/O AL is understood, the next question is whether the above process sequence can be repeated multiple times for SL growth or whether the defects propagate ultimately causing an epitaxial breakdown? What is the thermal stability of O ALs in Si?

4. What is the impact of SL parameters (number of Si-O periods and the Si thickness between O ALs) on the structural and electrical properties of SLs?

1.8 Research objectives

This PhD research involves a systematic study on epitaxial Si-O SLs. The objectives are

1. To gain insight on the fabrication processes of CVD grown Si-O SL structures.
2. To understand the impact of different process parameters on the structural properties (O bonding structures, Si epitaxial quality, surface morphology etc.) of SLs.
3. To understand the electrical activity of O ALs in Si and to evaluate the carrier mobility of Si-O SL transistors.
4. To understand the structural and electrical properties of Si-O SL as a function of the SL parameters (number of Si-O periods and Si thickness between O ALs).

1.9 Organization of this thesis

An insight in the fabrication process, investigation on the structural properties and their impact on electrical behavior of epitaxial Si-O SLs is required in this research work. The thesis is organized into the following chapters

Chapter 2 - Experiment and characterization techniques

This chapter summarizes the experimental procedures and the different physical and electrical characterization techniques that are employed for the understanding of Si-O SL structures. The measurement procedure of each technique is briefly described and their limitations are indicated.

Chapter 3 - Deposition of O AL

The first step during the fabrication of epitaxial Si-O SLs, is the deposition of O AL. The deposition of O AL is investigated for the case of O_3 exposure on H−Si(100). The impact of the precursors on the O surface structures is studied in comparison with O_2 exposure. The change in O surface structures as

a function of O-content is experimentally investigated and is correlated with bond structures reported in literature.

Chapter 4 - Epitaxial Si on O AL

The second step during the fabrication of SLs is the epitaxial deposition of Si on O AL. The Oxygen is usually considered as contamination during Si homo-epitaxy and an epitaxial Si on O AL is challenging. This chapter will describe the insight on three process parameters that determine the crystalline quality of Si on O AL (1) Atomic surface distortions caused by O atoms (2) Oxygen surface structures (3) Arrival rate of SiH_4 flux. With understanding on these three parameters, epitaxial Si on O AL with minimum structural defects is demonstrated.

Chapter 5 - Epitaxial Si-O SL growth

Once the epitaxial Si on O AL with minimum structural defects is demonstrated, the ability to repeat the process for the fabrication of Si-O SLs with multiple periods is explored. The challenges are linked with the surface properties of the Si layer at each period and requires a surface passivation for the growth of defect free Si-O SLs with 2 and 5 periods. More details on such interface engineering are given in Chapter 5.

Chapter 6 - Electronic properties of epitaxial Si-O SL

At last, the electronic properties of the epitaxial Si-O SL is evaluated using test structures (Schottky Diodes, MOS capacitors and MOS transistors). Deep level transient spectroscopy is employed to understand the electrical activity of the O layers in Si as a function of the SL parameters (number of Si-O periods and Si thickness between O ALs). MOS transistors are used to evaluate the carrier mobility.

The final chapter will summarize the conclusions of this research study. Suggestions for mobility improvements and alternative approaches are outlined.

Bibliography

[1] Probir K. Bondyopadhyay. Moore's law governs the silicon revolution. *Proc. IEEE*, 86(1):78–81, 1998.

[2] R.H. Dennard, F.H. Gaensslen, V.L. Rideout, Ernest Bassous, and A.R. LeBlanc. Design of ion-implanted MOSFET's with very small physical dimensions. *IEEE J. Solid-State Circuits*, 9(5):256–268, oct 1974.

[3] ITRS technology roadmap. ITRS, 2013.

[4] Suman Datta. Recent Advances in High Performance CMOS Transistors: From Planar to Non-Planar. *Electrochem. Soc. Interface*, pages 41–46, 2013.

[5] Yang-Kyu Choi, Kazuya Asano, Nick Lindert, Vivek Subramanian, Tsu-Jae King, Jeffrey Bokor, and Chenming Hu. Ultrathin-body SOI MOSFET for deep-sub-tenth micron era. *IEEE Electron Device Lett.*, 21(5):254–255, may 2000.

[6] Xuejue Huang, Wen-Chin Lee, Charles Kuo, Digh Hisamoto, Leland Chang, Jakub Kedzierski, Erik Anderson, Hideki Takeuchi, Yang-Kyu Choi, Kazuya Asano, Vivek Subramanian, Tsu-Jae King, Jeffrey Bokor, and Chenming Hu. Sub 50-nm FinFET: PMOS. In *Int. Electron Devices Meet. 1999. Tech. Dig. (Cat. No.99CH36318)*, pages 67–70. IEEE, 1999.

[7] Fu-Liang Yang, Di-Hong Lee, Hou-Yu Chen, Chang-Yun Chang, Sheng-Da Liu, Cheng-Chuan Huang, Tang-Xuan Chung, Hung-Wei Chen, Chien-Chao Huang, Yi-Hsuan Liu, Chung-Cheng Wu, Chi-Chun Chen, Shih-Chang Chen, Ying-Tsung Chen, Ying-Ho Chen, Chih-Jian Chen, Bor-Wen Chan, Peng-Fu Hsu, Jyu-Horng Shieh, Han-Jan Tao, Yee-Chia Yeo, Yiming Li, Jam-Wem Lee, Pu Chen, Mong-Song Liang, and Chenming Hu. 5nm-gate nanowire FinFET. In *Dig. Tech. Pap. 2004 Symp. VLSI Technol. 2004.*, pages 196–197. IEEE, 2004.

[8] S. Eneman, P. Verheyen, R. Rooyackers, F. Nouri, L. Washington, R. Degraeve, B. Kaczer, V. Moroz, A. De Keersgieter, R. Schreutelkamp, M. Kawaguchi, Y. Kim, A. Samoilov, L. Smith, P.P. Absil, K. De Meyer, M. Jurczak, and S. Biesemans. Layout impact on the performance of a locally strained PMOSFET. In *Symp. VLSI Technol. 2005.*, pages 22–23. Ieee, 2005.

[9] Christoph Adelmann, Daniel Cuypers, Massimo Tallarida, Leonard N. J. Rodriguez, Astrid De Clercq, Daniel Friedrich, Thierry Conard, Annelies Delabie, Jin Won Seo, Jean-Pierre Locquet, Stefan De Gendt, Dieter Schmeisser, Sven Van Elshocht, and Matty Caymax. Surface Chemistry

and Interface Formation during the Atomic Layer Deposition of Alumina from Trimethylaluminum and Water on Indium Phosphide. *Chem. Mater.*, 25(7):1078–1091, apr 2013.

[10] Hong Dong, Wilfredo Cabrera, Xiaoye Qin, Barry Brennan, Dmitry Zhernokletov, Christopher L Hinkle, Jiyoung Kim, Yves J Chabal, and Robert M Wallace. Silicon interfacial passivation layer chemistry for high-k/InP interfaces. *ACS Appl. Mater. Interfaces*, 6(10):7340–5, may 2014.

[11] Youngki Yoon, Kartik Ganapathi, and Sayeef Salahuddin. How Good Can Monolayer MoS 2 Transistors Be? *Nano Lett.*, 11(9):3768–3773, sep 2011.

[12] K. S. Novoselov. Electric Field Effect in Atomically Thin Carbon Films. *Science*, 306(5696):666–669, oct 2004.

[13] K S Novoselov, Andre Konstantin Geim, S V Morozov, D Jiang, M I Katsnelson, I V Grigorieva, S V Dubonos, and a a Firsov. Two-dimensional gas of massless Dirac fermions in graphene. *Nature*, 438(7065):197–200, nov 2005.

[14] Baojie Feng, Zijing Ding, Sheng Meng, Yugui Yao, Xiaoyue He, Peng Cheng, Lan Chen, and Kehui Wu. Evidence of silicene in honeycomb structures of silicon on Ag(111). *Nano Lett.*, 12(7):3507–3511, 2012.

[15] Antoine Fleurence, Rainer Friedlein, Taisuke Ozaki, Hiroyuki Kawai, Ying Wang, and Yukiko Yamada-Takamura. Experimental evidence for epitaxial silicene on diboride thin films. *Phys. Rev. Lett.*, 108(24):1–5, 2012.

[16] Li Tao, Eugenio Cinquanta, Daniele Chiappe, Carlo Grazianetti, Marco Fanciulli, Madan Dubey, Alessandro Molle, and Deji Akinwande. Silicene field-effect transistors operating at room temperature. *Nat. Nanotechnol.*, 10(February):1–5, 2015.

[17] Alessandro Molle, Carlo Grazianetti, Daniele Chiappe, Eugenio Cinquanta, Elena Cianci, Grazia Tallarida, and Marco Fanciulli. Hindering the oxidation of silicene with non-reactive encapsulation. *Adv. Funct. Mater.*, 23(35):4340–4344, sep 2013.

[18] B Radisavljevic, A Radenovic, J Brivio, V Giacometti, and Andreas Kis. Single-layer MoS_2 transistors. *Nat. Nanotechnol.*, 6(3):147–150, 2011.

[19] Branimir Radisavljevic and Andras Kis. Mobility engineering and a metal–insulator transition in monolayer MoS_2. *Nat. Mater.*, 12(9):815–820, jun 2013.

[20] Bo Zhou, L.X. Yang, Fei Chen, Min Xu, Tao Wu, Gang Wu, X.H. Chen, and D.L. Feng. Evolution of electronic structure in WS_2 and WSe_2. *J. Phys. Chem. Solids*, 72(5):474–478, may 2011.

[21] Yi Hsien Lee, Lili Yu, Han Wang, Wenjing Fang, Xi Ling, Yumeng Shi, Cheng Te Lin, Jing Kai Huang, Mu Tung Chang, Chia Seng Chang, Mildred Dresselhaus, Tomas Palacios, Lain Jong Li, and Jing Kong. Synthesis and transfer of single-layer transition metal disulfides on diverse surfaces. *Nano Lett.*, 13(4):1852–1857, 2013.

[22] Annelies Delabie, M. Caymax, Benjamin Groven, Markus Heyne, Karel Haesevoets, Johan Meersschaut, Thomas Nuytten, Hugo Bender, Thierry Conard, Patrick Verdonck, Sven Van Elshocht, Stefan De Gendt, M. Heyns, Kathy Barla, I. Radu, and Aaron Thean. Low temperature deposition of 2D WS_2 layers from WF_6 and H_2S precursors: impact of reducing agents. *Chem. Commun.*, 51(86):15692–15695, 2015.

[23] R J Mears, N Xu, N Damrongplasit, H Takeuchi, R J Stephenson, N W Cody, A Yiptong, X Huang, and M Hytha. Simultaneous carrier transport enhancement and variability reduction in Si MOSFETs by insertion of partial monolayers of oxygen. In *IEEE Silicon Nanoelectron. Work.*, volume 50, pages 33–34, 2012.

[24] Nuo Xu, Marek Hytha, Hideki Takeuchi, Xiangyang Huang, Robert J Stephenson, Nyles Cody, Robert J Mears, and Tsu-jae King Liu. Effectiveness of quasi-confinement technology for improving P-channel Si and Ge MOSFET performance. Technical report, 2013.

[25] Nuo Xu, Hideki Takeuchi, Marek Hytha, Nyles W. Cody, Robert J. Stephenson, Byungil Kwak, Seon Yong Cha, Robert J. Mears, and Tsu-Jae King Liu. Electron mobility enhancement in (100) oxygen-inserted silicon channel. *Appl. Phys. Lett.*, 107(12):123502, sep 2015.

[26] Robert J Mears, Marek Hytha, Ilija Dukovski, Augustin Yiptong, Xiangyang Huang, Samed Halilov, Andi Broka, Robert J Stephenson, Vivek Rao, Douglas R Webb, Rajesh Prasad, Scott A Kreps, Hideki Takeuchi, Shu Ikeda, Gabe Gebara, Ken Matthews, Jeff T Wetzel, Wade Xiong, Chris Bowen, Rick Wise, C Rinn Cleavelin, and Texas Instruments. Silicon superlattice for high mobility and reduced leakage. In *IEEE Int. SOI Conf.*, pages 23–24, 2007.

[27] N. Xu, N. Damrongplasit, H. Takeuchi, R. J. Stephenson, N. W. Cody, A. Yiptong, X. Huang, M. Hytha, R. J. Mears, and Tsu-Jae King Liu. MOSFET performance and scalability enhancement by insertion of oxygen layers. In *2012 Int. Electron Devices Meet.*, pages 6.4.1–6.4.4. IEEE, dec 2012.

[28] Xuan Luo, S B Zhang, and Su-Huai Wei. Chemical design of direct-gap light-emitting silicon. *Phys. Rev. Lett.*, 89(2):076802, 2002.

[29] Augustin Lu. *Private communications*, 2013.

[30] Paolo Giannozzi, Stefano Baroni, Nicola Bonini, Matteo Calandra, Roberto Car, Carlo Cavazzoni, Davide Ceresoli, Guido L Chiarotti, Matteo Cococcioni, Ismaila Dabo, Andrea Dal Corso, Stefano de Gironcoli, Stefano Fabris, Guido Fratesi, Ralph Gebauer, Uwe Gerstmann, Christos Gougoussis, Anton Kokalj, Michele Lazzeri, Layla Martin-Samos, Nicola Marzari, Francesco Mauri, Riccardo Mazzarello, Stefano Paolini, Alfredo Pasquarello, Lorenzo Paulatto, Carlo Sbraccia, Sandro Scandolo, Gabriele Sclauzero, Ari P Seitsonen, Alexander Smogunov, Paolo Umari, and Renata M Wentzcovitch. QUANTUM ESPRESSO: a modular and open-source software project for quantum simulations of materials. *Journal of Physics: Condensed Matter*, 21(39):395502, sep 2009.

[31] Raphael Tsu and John C Lofgren. Structure of MBE grown semiconductor–atomic superlattices. *J. Cryst. Growth*, 227-228:21–26, jul 2001.

[32] Audrius Alkauskas, Peter Broqvist, and Alfredo Pasquarello. Defect levels through hybrid density functionals: Insights and applications. *physica status solidi (b)*, 248(4):775–789, apr 2011.

[33] Richard A.Blanchard, Vivek Rao Kalipatnam, and Scott A.Kreps. US Patent - FINFET including a superlattice (US 7202494B2), 2007.

[34] Robert J Mears. Method for making semiconductor device including band engineered superlattice, 2004.

[35] Robert J. Mears, Jean Augustin Fook, Chan Sow, A. Yiptong, M. Hytha, and Ilija Dukovski. Semiconductor structures having improved conductivity effective mass and methods for fabricating the same.pdf, 2004.

[36] Robert J. Mears and Scott A.Kreps. semiconductor device including a superlattice having at least one group of substantialy undoped layers.pdf, 2005.

[37] Robert J. Mears, Marek Hytha, and SCott A Kreps. semiconductor device including the channel with non-semiconductor monolayer layer.pdf, 2007.

[38] Kengo Nishio, Augustin Lu, and Geoffrey Pourtois. Low-strain Si / O superlattices with tunable electronic properties : Ab initio calculations. *Phys. Rev. B*, 165303:1–10, 2015.

[39] G Ghidini and F W Smith. Interaction of H_2O with Si(111) and (100). Critical conditions for the growth of SiO_2. *J.Electrochem.Soc*, 131:2924–2928, 1984.

[40] Y. J. Chabal and S. B. Christman. Evidence of dissociation of H_2O on the Si(100)2 $\times$ 1 surface. *Phys. Rev. B*, 29(12):6974–6976, jun 1984.

[41] E G Keim. Adsorption of atomic oxygen (N_2O) on a clean Si(100) surface and its influence on the surface state density; A comparison with O_2. *Surf. Sci.*, 180:565–598, 1987.

[42] Bhavin N. Jariwala, Cristian V. Ciobanu, and Sumit Agarwal. Initial oxidation stages of hydrogen- and styrene-terminated Si(100) surfaces: A molecular dynamics study. *Surf. Sci.*, 605(21-22):L61–L66, nov 2011.

[43] Christian Fink and Stephen Jenkins. First-principles molecular dynamics of the initial oxidation of Si{001} by ozone. *Phys. Rev. B*, 78(19):195407, nov 2008.

[44] Zhenjiang Cui and Christos G. Takoudis. Initial Oxidation of H-Terminated Si(100) in O_3 (950 ppm)/O_2 and Pure O_2. *J. Electrochem. Soc.*, 150(11):G694, 2003.

[45] X. Zhang, E. Garfunkel, Y. J. Chabal, S. B. Christman, and E. E. Chaban. Stability of HF-etched Si(100) surfaces in oxygen ambient. *Appl. Phys. Lett.*, 79(24):4051–4053, 2001.

[46] Christian K. Fink and Stephen J. Jenkins. Radical-mediated adsorption: Ozone oxidation of passivated silicon. *Surf. Sci.*, 602(14):L100–L103, jul 2008.

[47] Christian K Fink, Ken Nakamura, Shingo Ichimura, and Stephen J Jenkins. Silicon oxidation by ozone. *J. Phys. Condens. Matter*, 21(18):183001, may 2009.

[48] A Kurokawa and S Ichimura. High purity ozone oxidation on hydrogen passivated silicon surface. *Appl. Surf. Sci.*, 100-101:436–439, jul 1996.

[49] Zhenjiang Cui, Jonathan M. Madsen, and Christos G. Takoudis. Rapid thermal oxidation of silicon in ozone. *J. Appl. Phys.*, 87(11):8181, 2000.

[50] R. H. Finch, H. J. Queisser, G. Thomas, and J. Washburn. Structure and Origin of Stacking Faults in Epitaxial Silicon. *J. Appl. Phys.*, 34(2):406, 1963.

[51] Matty Caymax. Private Communication. Technical report, 1994.

[52] A Gruhle, G. Schmidt, H. Beneking, and H. Holzbrecher. Influence of oxygen contamination during Si low presure vapour phase epitaxy on epitaxial layer quality. *J. Cryst. Growth*, 110(4):985–988, apr 1991.

[53] Roger Loo, Andriy Hikavyy, Frederik E. Leys, Masayuki Wada, Kenichi Sano, Brecht De Vos, Antoine Pacco, Mireia Bargallo Gonzalez, Eddy Simoen, Peter Verheyen, Wendy Vanherle, and Matty Caymax. Low temperature pre-epi treatment: critical parameters to control interface contamination. *Solid State Phenom.*, 145-146:177–180, 2009.

[54] Joseph M. Jasinski and Stephen M. Gates. Silicon chemical vapor deposition one step at a time: fundamental studies of silicon hydride chemistry. *Acc. Chem. Res.*, 24(1):9–15, jan 1991.

[55] Jan-otto Carlsson. Chemical Vapor Deposition. *Handbook of Deposition Technologies for Films and Coatings*, pages 400–459, 2010.

[56] S. M. Gates, C. M. Greenlief, D. B. Beach, and P. A. Holbert. Decomposition of silane on Si(111)-(7×7) and Si(100)-(2×1) surfaces below 500 °C. *J. Chem. Phys.*, 92(5):3144, 1990.

[57] S.M. Gates, C.M. Greenlief, D.B. Beach, and R.R. Kunz. Reactive sticking coefficient of silane on the Si(111)-(7×7) Surface. *Chem. Phys. Lett.*, 154(6):505–510, feb 1989.

[58] S.M. Gates. Kinetics and mechanisms of surface reactions in epitaxial growth of Si from SiH_4 and Si_2H_6. *J. Cryst. Growth*, 120(1-4):269–274, may 1992.

[59] S. M. Gates and S. K. Kulkarni. Kinetics of surface reactions in very low-pressure chemical vapor deposition of Si from SiH_4. *Appl. Phys. Lett.*, 58(25):2963, 1991.

[60] A Vittadini and A Selloni. Density functional study of H_2 desorption from monohydride and dihydride Si (100) surfaces. *Chem. Phys. Lett.*, 235(March):334–340, 1995.

[61] Kumar Sinniah, Michael G. Sherman, Lisa B. Lewis, W. Henry Weinberg, John T. Yates, and Kenneth C. Janda. Hydrogen desorption from the monohydride phase on Si(100). *J. Chem. Phys.*, 92(9):5700, 1990.

[62] Kumar Sinniah, Michael G. Sherman, Lias B. Lewis, W. Henry Weinberg, John T. Yates, and Kenneth C. Janda. New Mechanism for Hydrogen Desorption from Covalent Surfaces: The Monohydride Phase on Si(100). *Phys. Rev. Lett.*, 62(5):567–570, jan 1989.

[63] S. M. Gates, C. M. Greenlief, and D. B. Beach. Decomposition mechanisms of SiHx species on Si(100)-(2×1) for x=2, 3, and 4. *J. Chem. Phys.*, 93(10):7493, 1990.

[64] Christine J Wu and Emily A Carter. Adsorption of hydrogen atoms on the Si(100)-2×1 surface: implications for the H_2 desorption mechanism. *Chem. Phys. Lett.*, 185(1-2):172–178, 1991.

[65] Y. W. Mo, J Kleiner, M. B. Webb, and M. G. Lagally. Activation energy for surface diffusion of Si on Si(001): A scanning-tunneling-microscopy study. *Phys. Rev. Lett.*, 66(15):1998–2001, apr 1991.

[66] Keith H Chung. *Si based Epitaxy by Chemical vapor Deposition using novel precursor Neopentasilane*. PhD thesis, 2006.

[67] Ken Uchida and Masumi Saitoh. Carrier transport and stress engineering in advanced nanoscale MOS transistors. In *2009 Int. Symp. VLSI Technol. Syst. Appl.*, number 100, pages 6–7. IEEE, apr 2009.

[68] Raphael Tsu and Qi Zhang. Nanostructured Electronics and Optoelectronic Materials. In *Nanostructured Mater.*, pages 677–717. Elsevier, 2007.

[69] Peter Deák, Martin Rosenbauer, Martin Stutzmann, Jörg Weber, and Martin S. Brandt. Siloxene: Chemical quantum confinement due to oxygen in a silicon matrix. *Phys. Rev. Lett.*, 69(17):2531–2534, oct 1992.

[70] Tsu Raphael. Silicon-based Quantum wells. *Nature*, 364:19, 1993.

[71] Raphael Tsu, Jonder Morais, and Amanda Bowhill. Visible Light Emission in Silicon-Interface Adsorbed Gas Superlattices. In *Mater. Res. Soc. Symp. Proc. 358*, page 825, 1994.

[72] R. Tsu, D. Quinlan, and K. Daneshvar. Silicon–O–M–O–silicon superlattice. *Microelectronics J.*, 37(12):1519–1522, dec 2006.

[73] R. Tsu. Si Based Green ELD: Si-Oxygen Superlattice. *Phys. Status Solidi(a)*, 180(1):333–338, 2000.

[74] K Dovidenko, J.C. Lofgren, F. de Freitas, Y.J. Seo, and R Tsu. Structure and optoelectronic properties of Si/O superlattice. *Phys. E Low-dimensional Syst. Nanostructures*, 16(3-4):509–516, mar 2003.

[75] Q Zhang, A Filios, C Lofgren, and R Tsu. Ultra-stable visible electroluminescence from crystalline-Si/O superlattice. *Phys. E*, 8:365–368, 2000.

[76] Yong-Jin Seo, John C. Lofgrene, and Raphael Tsu. Transport through a nine period silicon/oxygen superlattice. *Appl. Phys. Lett.*, 79(6):788, 2001.

[77] Yong-jin Seo and Tsu Raphael. Epitaxially-Grown Multilayer Nanocrystalline Si-O Structure for Silicon-on-Insulator Applications. *J. Korean Phys. Soc.*, 45(1):120–123, 2004.

[78] Junichi Murota, Masao Sakuraba, and Bernd Tikkack. Atomic-Order Thermal Nitridation of Si, SiGe and Ge by NH_3. *ECS Transactions*, 61(2):97–104, 2014.

[79] Junichi Murota, Masao Sakuraba, and Bernd Tillack. Atomically Controlled Processing for Group IV Semiconductors by Chemical Vapor Deposition. *Japanese Journal of Applied Physics*, 45(9A):6767–6785, sep 2006.

[80] Y. Shimamune, M. Sakuraba, T. Matsuura, and J. Murota. Epitaxial growth of heavily P-doped Si films at 450 °C by alternately supplied PH_3 and SiH_4. *Le Journal de Physique IV*, 11(PR3):Pr3–255–Pr3–260, aug 2001.

[81] Jintae Noh, Masao Sakuraba, Junichi Murota, Shigeaki Zaima, and Yukio Yasuda. Contact resistivity between tungsten and impurity (P and B)-doped SiGeC epitaxial layer. *Applied Surface Science*, 212-213:679–683, may 2003.

Chapter 2

Experimental and characterization techniques

This chapter will summarize different physical and electrical characterization techniques that are employed for investigating Si−O SL structures. The purpose, background theory of each technique is briefed and their limitations are indicated.

2.1 Experimental details

The Si-O SLs are grown on Si(100) substrate after the surface preparations.

Surface Preparation: 200 mm boron-doped Si(100) wafers (1×10^{16} cm^{-3}) are used for the fabrication of Si−O SLs. A sequential cleaning of wafers is done before the deposition of SL structures. First, the wafers undergo a standard clean creating a thin oxide layer at the top [1]. Second, the wafers are cleaned in a 2% HF/H_2O solution for 30 seconds to remove the oxide and to passivate the surface with H-termination. Instantly, the wafers are loaded into the load ports of the polygon cluster (Fig.2.1). The load ports are maintained in inert N_2 ambient to avoid surface oxidation. As a last step of cleaning, a pre-epi bake is performed in the CVD chamber at 850°C for 2 minutes at 40 Torr in H_2 ambient [2]. The residual O contaminations and the surface hydrides are desorbed during this process [2–4]. The wafers are cooled down to 350°C in H_2 to terminate the wafer surface with hydrogen [5].

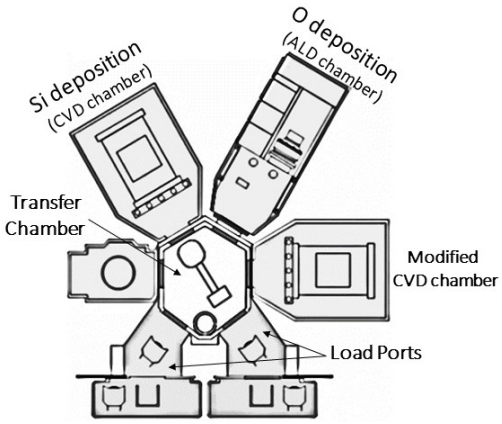

Figure 2.1: Schematic of 200 mm polygon cluster.

Si and O depositions: After the pre-epi bake, the wafers are transferred to the ALD chamber for the deposition of O ALs. Such transfers occur through a transport chamber maintained in N_2 to minimize the transport contamination. The amount of O contamination during the transport from CVD to the ALD chamber (without O deposition) has been measured to be 3×10^{13} O atoms/cm^2, which is an order of magnitude lower than the targeted O-content (1 O AL = 6.78×10^{14} O atoms/cm^2).

Two different precursors are studied for the deposition of O AL. Due to the high reactive nature on H–Si(100) at low temperatures, Ozone (O_3) is investigated. The O_3 is generated from O_2 in a TMEIC OP-250H O_3 generator, providing O_3 concentrations of 100-350 g/m^3 by electric discharge technology. The O ALs are deposited by the exposure of O_3 at a temperature of 50°C and at a partial pressure of 0.01-0.08 Torr with the regulated pulses varying from 50 milli seconds to 10 seconds. To investigate the impact of precursors on the O surface structures, the exposure of O_2 on H–Si(100) at 300°C for the several minutes (2-40 minutes) with a partial pressure of 0.21-0.44 Torr is studied. The pure O_2 is obtained by shutting down O_3 generation coupled with N_2 flushing of gas lines for 6 hours.

After the deposition of O AL, the wafers are transferred back to the CVD chamber for the epitaxial deposition of Si. The silane (SiH_4) is used for the Si deposition at a low temperature of 500°C-550°C at partial pressure of 20-150 mTorr. N_2 is used as the carrier gas. In some cases, an *in-situ* anneal in H_2 or N_2 ambient is performed. For H_2 anneal, the H_2 gas is introduced into the reactor with a partial pressure of 40 Torr at a temperature of 600°C for

a duration of 5 min. For N_2-anneal, as the Si layers are deposited using N_2 carrier gas, the SiH_4 gas is switched off and the N_2 is continued to flow at a similar anneal conditions as H_2 anneal. After the anneals, the structures are cooled down to 350°C in their respective ambient.

At the end, the wafers are shuttled between CVD and ALD reactors, until the "n" number of Si and O periods of the SL are fabricated. The epitaxial Si on Si (homo-epitaxy) are grown as references with similar deposition conditions as SL structures.

2.2 Physical Characterization

2.2.1 Characterization of O AL

Different complementary *exsitu* surface characterization techniques are employed in understanding the O surface structures formed upon O_3 or O_2 exposure on H–Si(100). They are summarized below

Secondary ion mass spectroscopy (SIMS)

Purpose: To measure the O,C depth profiles in Si and quantify them precisely.
Procedure: During the SIMS measurement, a primary energetic Cs^+ beam with the typical energy of 5 KeV is rastered over the sample surface to create the collision cascade and the secondary species from the surface. Among them, a small portion is ionized and is accelerated into the quadrupole mass spectrometer allowing sequential detection of different elements using mass to charge ratios. The detected counts are transformed into atomic concentrations (atoms/cm^3) using standards, while the sputter time is transformed into a depth scale using crater depth measurements. The conventional SIMS measurements are performed with the beam energy of 5 keV in a high vacuum chamber up to $4x10^{-10}$ mbar. The Si-O SL samples were measured in Atomika 4500.
Additional sample preparation: The quantification of the O layer requires a Si encapsulation of $\sim$ 100 nm to avoid the contribution of native oxide and the surface transients interfering with the O AL beneath.
Limitation: Unlike the conventional measurements at the beam energy of 5 keV, the layers are sputtered at 500 eV. This is advantageous as we could improve the depth resolution, however at the cost of the measurement time and higher detection limit.

Attenuated total reflectance Fourier transform infrared (ATR-FTIR) spectroscopy

Purpose: To determine the surface structures by monitoring Si – H bond vibrations.
Procedure: The sample surface, where the bonding structures are to be determined, is placed against the ATR crystal. An infrared beam is passed through the ATR crystal at an angle, such that it undergoes a total internal reflection in contact with the sample. The critical angle (θ_c) for the total internal reflection depends on the refractive index of the sample (n2) and the ATR crystal(n1).

$$\theta_{\mathrm{c}} = sin^{-1}(\frac{n2}{n1}) \tag{2.1}$$

For the Ge ATR crystal and the Si sample, the θ_{c} is around 60°. The total reflection forms an evanescent wave, which projects orthogonal into the sample up with the penetration depth of 0.5 microns. Some energy of evanescent wave is adsorbed by the structural vibrations, while the rest is transmitted to the detector. For this work, the ATR measurements are performed in a Nicolet 6700 spectrometer with the resolution of 2 cm^{-1} averaging over 64 spectra within 400-4000 cm^{-1} range. For every recorded spectrum, the background is subtracted and the baseline is corrected. The measurements are time coordinated with the depositions, and wafers are transferred in a vacuum sealed box. The measurement delay is limited to less than 25 minutes to minimize surface oxidation.
Additional sample preparation: None.
Limitation: The signatures from Si – O vibrations are difficult to detect, as they interfere with the atmospheric ambient. The depositions and the measurements need to be time coordinated.

X-ray photoelectron Spectroscopy (XPS)

Purpose: To measure the surface oxidation states after O_3 or O_2 exposure on H – Si(100).
Procedure: The XPS is a spectroscopic analysis, which is used for the elemental identification and the chemical state of the elements in a material. The X-ray beam illuminates a sample from which electrons are ejected by the photoelectric effect. The kinetic energy of the ejected electrons is then determined. As the energy of the X-ray is known, the binding energy of the electron is calculated. With the given binding energy, one can identify the elements from which the

electron originates. Depending on the chemical state of the elements, small variation of the binding energy are measured. In our case, mostly the binding of Si and the difference in binding energy due to the surface oxidation are investigated. The XPS measurements were carried out in an angle integrated-mode, where the spectrum contains electrons with an exit angle between 21 and 78° using a Theta300 system from Thermo Instruments. The measurements were performed using a mono-chromatized Al Kα X-ray source (1486.6eV) and a spot size of 400 μm. The individual Si sub-oxide contributions are quantified by peak fitting and by integrating the individual peak areas as described by Lu *et al.* [6].
Additional sample preparation: As O AL is very susceptible to surface oxidation upon exposure, a thin of Si layer (∼1.5 nm) is deposited above the O AL during the time coordinated XPS measurements.

Water Contact Angle (WCA)

Purpose: To measure the hydrophobicity of the surface after O_3 exposure.
Procedure: The water contact angle (WCA) is measured in a Dataphysics OCAH230L system using de-ionized water droplets at room temperature. As soon as the O AL is deposited, the wafers are time coordinated with a measurement delay of less than 10 minutes. Using a sessile drop technique, where the droplet with known surface energy (in this case, it is water) and with constant volume is used to determine the contact angle of the droplet. The droplets are circularly fitted during the WCA determination. The values are averaged over different positions on the wafer.
Additional sample preparation: None
Limitation: Requires sufficient statistics (5-6 measurements) across the wafer to conclude on the surface properties. The measurements have to be performed prior to the surface oxidation or the droplet evaporation.

2.2.2 Characterization of Si layer/ O AL

Mass Balance measurements

Purpose: To estimate the deposited Si thickness based on the relative change in mass (Δm) before and after Si deposition.
Procedure: Using equation 2.2, one can calculate the thickness of the deposited Si layer for a given Si density ($\rho = 2.32$ g/cm^3) and surface area of the wafer (A_{wafer}). The weight loss due to the HF clean (171 μg) is taken into account during the calculation of Si thickness.

$$Sithickness = \frac{\Delta m}{\rho * A_{wafer}} \tag{2.2}$$

Additional sample preparation: None
Limitation: The growth rate through mass balance could be overestimated due to the thickness non-uniformity over the 200 mm wafer,the deposition at the top and at back side of the wafers.

Channeling in Rutherford back scattering (RBS/C)

Purpose: To study on the epitaxial quality of the Si layer on O AL in terms of atoms displaced from lattice position. This is complementary to transmission electron microscopy (TEM) analysis.
Procedure: A well collimated He^+ beam at an energy of 1.22 MeV is created using a 6SDH Pelletron accelerator. The back-scattered ions are detected using a silicon surface barrier detector at a scattering angle of 170°. When the incoming beam is aligned with a major crystallographic axis, there is a drastic decrease of the backscattered yield as the incoming ions are guided through the channel with a low probability of direct collisions. This phenomenon is called as the ion beam channeling. From these channeling measurements, information on crystalline quality and whether the atoms are in its lattice position or being displaced is obtained.
Additional sample preparation: None.
Limitation: The depth resolution of the RBS/C measurements is limited.

Transmission electron microscopy

Purpose: To obtain the structural insight on the grown Si-O SL structures i.e. to investigate the epitaxial ordering, defects, Si thickness between O ALs.
Procedure: The electrons are transmitted through a sample to form an image. The image is magnified, focused onto an fluorescent screen and captured by the camera. The TEM is kept in vacuum to have a high mean free path, typically on the order of 10^{-4} Pa. The contrast in the image arises from the diffraction effects and material density variations. At high magnification and for very thin foils, interference of transmitted and diffracted electrons gives rise to phase contrast used for high resolution TEM.
Additional sample preparation: The thickness of the sample required for TEM is less than 300 nm. The sample thinning is performed by dicing, polishing followed by ion milling. The thinned sample is attached to the special Cu grid of 3 mm in diameter. On top, a low temperature (150°C) CVD SiO_2 is deposited

to protect the top surface. The standard focused ion beam procedure involves milling with a 30 kV Ga ion beam from the substrate side. It has the advantage that the sample thickness will be more uniform below the structures. As final step, the samples are normally milled with a 5kV ion beam to reduce the surface damage.
Limitation: It is difficult to distinguish the lattice distortions, caused by O ALs sandwiched between thin Si layers of thickness <2 nm.

Atom probe tomography (APT)

Purpose: To investigate the spatial distribution of O atoms in the O AL and in the Si layer.
Procedure: A very sharp needle shaped sample is placed in an ultra high vacuum chamber. The sample is reduced to cryogenic temperatures (80 K) and placed such that the needle's point is aimed towards an ion detector. A high voltage is applied to the sample and a laser pulse is applied with pulse repetition rate of 400 fs at a wavelength of 515 nm (green). The application of the pulse to the sample allows individual atoms to be ejected as an ion at a known time. Typically the pulse amplitude and the high voltage on the specimen are adjusted to ionize only one atom in a given time. The delay between the application of the pulse and the detection of the ion(s) at the detector allow for the computation of the mass-to-charge ratio. The atomic three dimensional profile is reconstructed by applying a geometry based reconstruction method, relying on the tip shape.
Additional sample preparation: The tip for APT analysis, having an initial apex radius of about 50 nm, was prepared by annular focused ion beam (FIB) milling, using the lift out method [7]. The initial top of the shank was covered with 400 nm of a Pt containing polymer to avoid contamination from the 30 keV Ga beam during the milling process. Once the desired tip shape and size was obtained, the remaining Pt was removed by a low energetic (5 keV) Ga beam, limiting Ga and defect contamination at the surface.

Atomic force microscopy (AFM)

Purpose: To investigate the surface morphology of the Si layers on O AL.
Procedure: The cantilever used in an AFM has a sharp tip, which is often less than 10 nm in diameter at the apex. Forces between the tip and the sample surface cause the cantilever to deflect. A detector measures the cantilever deflections as the tip is scanned over the sample. As the cantilever bends, the position of the laser beam on the detector changes. The ratio of the path length between the cantilever and the detector to the length of the cantilever itself

produces amplification. As a result, the system can detect sub-angstrom vertical movement at the free end of the cantilever, where the tip is located.
Additional sample preparation: None.

2.3 Electrical characterization

2.3.1 Schottky diodes

Fabrication

Schottky diodes are fabricated with Si−O SL interfaced between the metal and the Si substrate. Metals with varying work function (Cr,Al) are thermally evaporated on the sample using a shadow mask with a diameter between 500 to 50 μm.

I-V and C-V measurement setup

The current - voltage (I-V) measurements are performed using HP4156 parametric analyzer in a voltage range between +5 to -5 volts and in steps of 0.1 volt. The voltage is given at the top electrode and the bottom electrode is grounded. The integration time during the measurement is 10 μs with the current compliance of 100 mA. The capacitance - voltage (C-V) measurements with same configuration is performed using the LCR meter (E4980A) from Agilent technologies at a frequency of 1 MHz. The I-V and C-V measurements are performed in room temperature.

2.3.2 MOS capacitors

Fabrication

The metal oxide semiconductor capacitors (MOSCAPs) are fabricated with a thin SiO_2 ($\sim$ 1 nm) deposited on Si−O SLs followed by an Al_2O_3 ($\sim$ 4 nm) gate dielectric deposited at 300°C. The Pt electrode is e-beam evaporated through a shadow mask with a diameter between 500 to 50 μm. Fourier Transform Deep Level Transient Spectroscopy (FT-DLTS) is employed to characterize the presence of deep defect levels in Si bandgap.

FT-DLTS measurement conditions

Fourier-transform DLTS (FT-DLTS)[8] has been performed at a fixed measurement frequency of 1MHz. Spectra have been recorded either isothermally, by sweeping the sampling period t_w (pulse period) or by scanning the temperature from 75K to RT. Before cooling the sample in the flow cryostat, C–V and I–V characteristics are recorded at room temperature.

Internal Photoemission Spectroscopy (IPE)

Purpose: IPE enables straightforward barrier determination at the SL/Al_2O_3 interface as the onset of the photoexcited transition of electrons from SL valence band into the Al_2O_3 conduction band by analyzing the spectral dependence of the quantum yield (Y). This technique may also probe both the electron density of states as well as the field induced band bending inside the Si-O SL region.
Procedure: IPE can be defined as a process of optically induced transitions of mobile carriers (electron or hole), from emitter into collector across the interface between them [9]. The minimal energy offset between the occupied electron states of the emitter and the empty states of the collector corresponds to the spectral threshold of photoemission (Φ_e). The IPE quantum yield, defined as the number of emitted electrons normalized to the number of exciting photons, expressed as a power function of the excess photon energy above Φ_e (equation 2.3).

$$Y(h\nu) = A(h\nu - \Phi_e)^p \tag{2.3}$$

For $h\nu > \Phi_e$, where exponent p reflects the functional form of the excited carrier energy distribution at the emitter surface. In case of the electron excitation from the semiconductor valence band, the IPE quantum yield follows the ($h\nu$ - Φ_e)^3 law [10]. The procedure of spectral threshold determination is based on the linear extrapolation of the yield spectral curve ($Y^{\frac{1}{p}}$ vs $h\nu$) to a zero value. The IPE measurements were performed in dc current mode in which the IPE current was determined as the difference between the photocurrent measured under illumination and the one measured in darkness, using Keithely 6517 electrometer. The light is emitted by a Xe-arc lamp which provides the photons in the energy range of $h\nu$ = 1.5 -6.2 eV. Fig.2.2 shows the band diagram of semiconductor/insulator interface. When the sample is illuminated with photon of energy $h\nu$, exceeding the energy barrier for electrons (Φ_e) under forward bias or the barrier of holes under negative gate bias, charge carriers are injected into the oxide producing a photocurrent as the carriers drifting towards the opposite metal electrode.

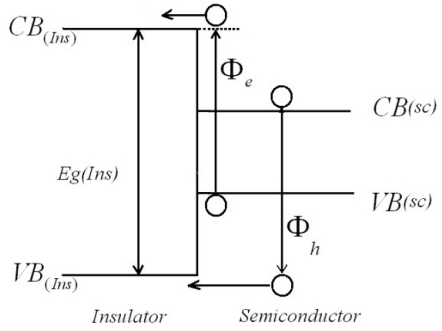

Figure 2.2: Schematic of semiconductor/Insulator band diagram, indicating the electron (Φ_e) and hole transitions (Φ_h) from the semiconductor into the insulator.

Additional sample preparation: MOSCAP structures with 20 nm of Al_2O_3 is deposited on the native oxide/Si-O SL using ALD technique. This is followed by the thermal evaporation of 10 nm thick semitransparent Au gate electrodes of area 0.5 mm^2 as a top electrode. The quantum yield of IPE was determined as the photocurrent across the oxide, normalized to the incident photon flux. The IPE experiments are investigated in the photon energy range of 1.5 - 7 eV.

2.3.3 Si-O SL transistors

The transistors with Si – O SL as channel are fabricated in a conventional CMOS process flow. The details of the individual steps during integration are given in Appendix C.

Bibliography

[1] Marc Meuris, Sophia Arnauts, Ingrid Cornelissen, K Kenis, M Lux, Stefan Degendt, P. Mertens, I. Teerlinck, R. Vos, L. Loewenstein, M.M. Heyns, and K. Wolke. Implementation of the IMEC-clean in advanced CMOS manufacturing. In *1999 IEEE Int. Symp. Semicond. Manuf. Conf. Proc. (Cat No.99CH36314)*, pages 157–160. IEEE, 1999.

[2] Roger Loo, Andriy Hikavyy, Frederik E. Leys, Masayuki Wada, Kenichi Sano, Brecht De Vos, Antoine Pacco, Mireia Bargallo Gonzalez, Eddy Simoen, Peter Verheyen, Wendy Vanherle, and Matty Caymax. Low temperature pre-epi treatment: critical parameters to control interface contamination. *Solid State Phenom.*, 145-146:177–180, 2009.

[3] P. Gupta, V. L. Colvin, and S. M. George. Hydrogen desorption kinetics from monohydride and dihydride species on silicon surfaces, 1988.

[4] A Vittadini and A Selloni. Density functional study of H_2 desorption from monohydride and dihydride Si (100) surfaces. *Chem. Phys. Lett.*, 235(March):334–340, 1995.

[5] H. Bender, S. Verhaverbeke, M. Caymax, O. Vatel, and M. M. Heyns. Surface reconstruction of hydrogen annealed (100) silicon. *J. Appl. Phys.*, 75(2):1207, 1994.

[6] Z. H. Lu, S. P. Tay, T. Miller, and T.-C. Chiang. Process dependence of the SiO_2/Si(100) interface structure. *J. Appl. Phys.*, 77(8):4110, 1995.

[7] M.K. Miller, K.F. Russell, K. Thompson, R. Alvis, and D.J. Larson. Review of atom probe FIB-based specimen preparation methods. *Microsc. Microanal.*, 13(6):428–436, 2007.

[8] S Weiss and R Kassing. Deep Level Transient Fourier Spectroscopy (DLTFS)—A technique for the analysis of deep level properties. *Solid. State. Electron.*, 31(12):1733–1742, 1988.

[9] V.Valery Afanas'ev. *Internal Photoemission Spectroscopy. Principles and Applications*, volume 1. Afanasev2008, 2008.

[10] R. J. Powell. Interface Barrier Energy Determination from Voltage Dependence of Photoinjected Currents. *J. Appl. Phys.*, 41(6):2424, 1970.

Chapter 3

Deposition of O atomic layer on Si(100)

Problem Statement: As the first step in the growth of Si-O SLs, the O AL is deposited on Si(100) substrate. The fundamental questions to be answered are, despite O being considered as contamination, will it be possible to control the O deposition at atomic layer level? What are the surface structures formed upon the deposition of O AL? Is there is any impact on the O precursors on the Si-O surface structures at atomic level?

Objective: The objective of this chapter is to investigate the O surface structures formed upon the O_3 and O_2 exposure on Si(100) for the deposition of O AL.

Organization of this chapter: The above questions are addressed in this chapter. First section will describe the Si surface structures prior to the deposition of O AL. The second section will investigate on the exposure of O_3 and O_2 on H−Si(100) for the deposition of O AL. The various O surface structures after the deposition of O AL are determined using complementary surface characterization techniques, as discussed in the third section. The last section proposes the Si−O bond models from our experimental understandings in comparison with the literature.

3.1 Si surface prior to the deposition of O AL

As the surface termination has a strong influence on the adsorption of O_3 or O_2, we need to investigate the surface structures prior to the deposition of O AL. They are monitored using ATR-FTIR in the range of 2000-2300 cm^{-1}. These wavenumbers correspond to the vibration modes of Si−H bonds. The surface structures are dictated by the HF clean (2% for 30 seconds) and the pre-epi bake (850°C for 2 minutes in H_2 at 40 Torr) performed during the sample preparation stage.

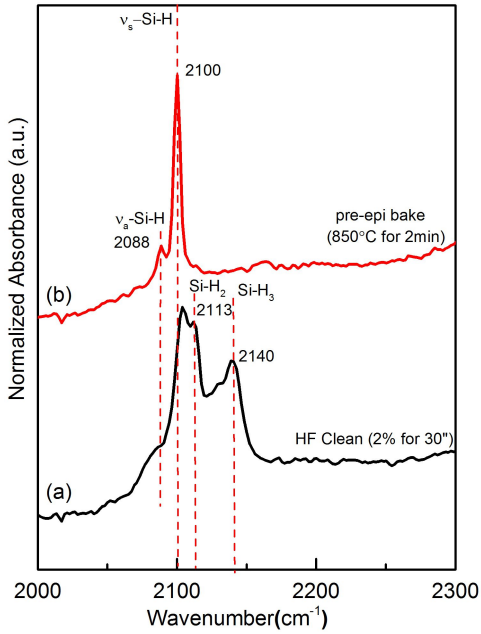

Figure 3.1: ATR-FTIR spectra of Si−H stretching vibration modes of (a) Si(100) surface after HF clean (2% for 30 seconds) with three distinct signatures corresponding to mono-(SiH), di-(SiH_2) and tri-(SiH_3) hydrides. (b) After pre-epi bake at 850°C for 2 min in H_2, the prominent peak at 2100 cm^{-1} indicate a uniform coverage of Si mono-hydrides [1].

The ATR-FTIR spectra immediately after the HF clean show three distinct Si−H stretching vibration modes at 2100, 2113 and 2140 cm^{-1} (Fig. 3.1a). The shoulder at 2088 cm^{-1} and a peak at 2100 cm^{-1} correspond to the asymmetric and symmetric stretching vibrations of coupled mono-hydrides (HSi−SiH) respectively [2, 3]. The peak at 2113 cm^{-1} corresponds to the asymmetric stretching vibrations of Si di-hydrides ($-Si-H_2$) [4]. The adjacent peak at higher

frequency (2140 cm^{-1}) indicates the presence of tri-hydrides ($-Si-H_3$)[5]. The occurrence of these mixed hydrides indicates that the surface is microscopically rough [6]. The broad peak widths at half maximum illustrates that the hydrides are not well ordered on the Si(100) surface.

After the pre-epi bake in H_2, the peak at 2100 cm^{-1} becomes prominent and sharp (Fig.3.1b), indicating the surface ordering for the H-terminated Si surface [7]. The asymmetric (2088 cm^{-1}) and symmetric (2100 cm^{-1}) Si–H stretching vibration modes are recorded, indicating the presence of only mono-hydrides. The higher order hydrides (di- and tri-) are unstable at temperatures beyond 350°C [8, 9]. During the pre-epi bake, the surface hydrides after HF clean are desorbed and the Si surface atoms undergo a 2×1 reconstruction. The wafers are cooled down in H_2 ambient to restore the H-termination [10]. The H-termination of the Si(100) surface is further confirmed from the water contact angle (WCA) measurements. The HF clean and the H_2 pre-epi bake sample yielded a WCA of 74±4° and 88±1°, respectively. The high value of the WCA indicates that the surface is hydrophobic, as expected for a H–Si(100).

3.2 Deposition of O ALs

Cui and co-workers have demonstrated Si oxidation using O_3 at low temperatures (50°C) leading to a 1 nm SiO_2 layer [11]. The deposition time for this process is 5-60 minutes leading to a large dose of O atoms responsible for the oxidation. For the deposition of O AL, we limit the supply of O atoms by lowering the deposition times in the range of a few milliseconds. This lowers the dose with a precise control of O atoms close to AL content. The Si surface atoms are less than 4+ oxidation state.

Fig.3.2 shows the O-content after O_2 and O_3 exposure on H–Si(100) at 300°C and 50°C respectively. The O_3 reaction at 50°C allows us to precisely control the O-content between 0.7 and 1.6 ALs [12]. The activation energy for the O_3 reaction on H–Si(100) is 0.05 eV, an order of magnitude lower than the O_2 reaction (0.3 eV) [13]. The difference is primarily due to the higher bond dissociation energy of molecular O_2 (O=O) compared to O_3 (O=O–O).

Thus the O_2 mandates a higher temperature for surpassing the barrier and to react with H–Si [11]. At temperature $\geq$ 300°C, the O_2 exposure yields layers with an O-content between 0.4 and 1.7 ALs for times between 3 and 30 min respectively. The H-content at the Si–O–Si interface is found to vary between 0.03 to 0.2 ALs. The interface C contamination is below the detection limit of SIMS.

From Fig.3.2, two distinct regimes of deposition are noticed. The first is the uptake of O atoms in proportion to the deposition time, which corresponds to the chemisorption of O atoms to the top 1-2 ALs. The second is the saturation regime corresponding to the onset of oxide film growth. The first regime is the region of interest for the deposition of O AL without permitting SiO_2 nucleation. The different activation energies and the reaction kinetics (discussed in Chapter 1) of O_3 and O_2 on H−Si(100), hints on the formation of different surface structures upon adsorption. The O deposition curves are difficult to fit with the Langmuir adsorption model, as it was not possible to compute the exact O fluence from the O_3 or from O2 molecules reacting on the H−Si(100) surface. The experimental investigation of surface structures after O_3 or O_2 adsorption is discussed in the following section.

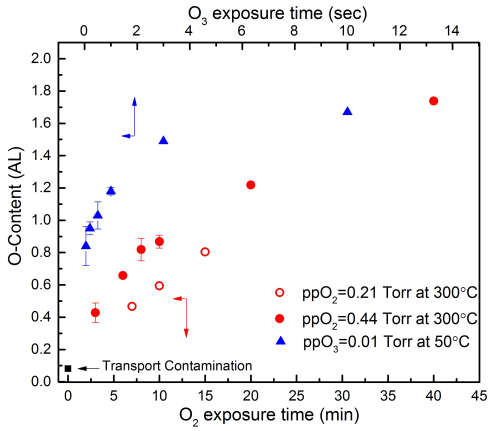

Figure 3.2: Deposited O-content as a function of partial pressure of O_3 or O_2 (ppO_3 or ppO_2) and exposure time quantified from SIMS (1 AL = 6.78×10^{14} atoms/cm^2). Error bars indicate the statistical control of the O-content. Transport contamination is 3×10^{13} O atoms/cm^2[1]. The O_3 was deposited at 50°C at partial pressure of 0.01 Torr. The O_2 was deposited at 300°C at partial pressure of 0.21 and 0.44 Torr. *NOTE: The units of X-axis are different for O_2 and O_3 processes.*

3.3 Characterization of the Si−O−Si interface

This section will describe the O surface structures formed by O_3 and O_2 exposures on H−Si(100).

As the O deposition is controlled below atomic layer content, most of the Si atoms at the Si–O–Si interface remain in 1+ oxidation state. This is indicated by the XPS Si-2p spectra of Si(1.5 nm)/O/Si(100) structures (Fig.3.3). The binding energy for different Si oxidation states are indicated by the dashed lines [14]. The individual sub-oxide contributions are quantified by peak fitting and by integrating the individual peak area as described elsewhere [14]. The quantitative evolution of the Si sub oxides as a function of the O-content is shown in Fig.3.4.

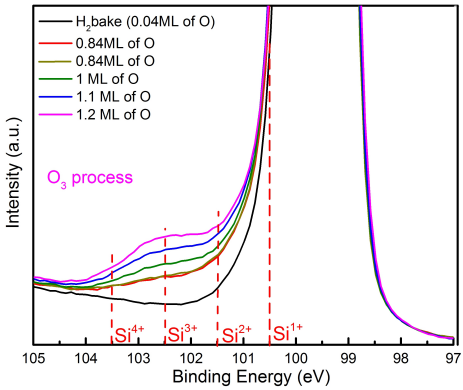

Figure 3.3: XPS spectra of Si ($\sim$ 1.5 nm)/O AL/Si(100) structures as a function of average O-content deposited using O_3 process. With increase in O-content, higher oxidation states appear in intensity. The binding energies for different Si oxidation states are marked with dashed lines [14].

After O_3 exposure at an O-content less than 1 AL, the primary oxidation state of Si is 1+. The quantities of Si^{2+}, Si^{3+} and Si^{4+} are less than 10%. This indicates that the O atoms are well dispersed at the Si–O–Si interface, as the presence of SiOx islands would be indicated by higher Si oxidation states [15]. When the O-content increases and exceeds 1 AL, then oxide component in the XPS Si-2p spectra increases in intensity and shifts towards higher binding energy, indicating an increased fraction of Si atoms at higher oxidation states. For much higher O_3 exposures,the SiO_2 is formed [16].

In contrast, for the O_2 process, the structure of the Si–O–Si interface is clearly different. At quite low O-contents, Si already exists in higher oxidation states, i.e. at 0.4 O AL there is around 47% of Si^{1+}, 25% of Si^{2+} and Si^{3+} coexist. At 0.8 AL of O-content, Si^{1+}, Si^{2+}, Si^{3+} as well as Si^{4+} coexist in similar concentrations. This indicates that the O atoms are less uniformly distributed, with the formation of small SiO_x clusters [15].

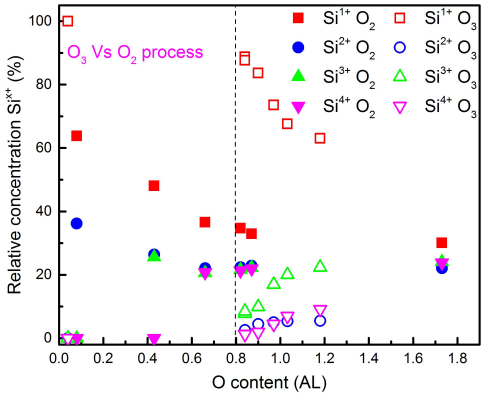

Figure 3.4: The relative distribution of Si sub oxides (Si^{x+}) as a function of average O-content for O_3 (open symbols) and O_2 (closed symbols) processes.

To further investigate the exact O surface species after O_3 or O_2 exposure, we employ ATR-FTIR spectroscopy. Compared to the spectrum at Fig.3.1, we observe the following changes after the O deposition from O_3 process (Fig.3.5). At an O-content of 0.84 AL, a shoulder peak at 2121 cm^{-1} appears, corresponding to the incorporation of single O atom either in the Si dimers (HSi−O−SiH) or in the Si back bonds (−Si−O−SiH) [17, 18] (Fig.3.5(c)). At an O-content higher than one atomic layer, a new peak appears at 2165 cm^{-1}, which gradually increases in intensity indicating Si−H vibrations with two O atoms in the back bonds [19] (Fig.3.5(d) - (f)).

The peak at 2100 cm^{-1} is still prominent, illustrating some Si−H bonds (mono-hydrides) are preserved even after the deposition of 0.84 O AL. It shifts from its original position of 2100 cm^{-1} towards higher wavenumbers (2106 cm^{-1}) and decrease in intensity. The shift is attributed to an increase in the σ-bond character of Si−H bonds due to electron withdrawal by the O atoms in the back bonds. The electronegativity of O is greater than that of Si, causing such electron withdrawals [20]. From calculations, the Si−H bond lengths before and after O-atom insertion is 1.49 and 1.46 Å respectively [21]. The broadening of the peaks at 2165, 2121 and 2106 cm^{-1} for 1.2 AL of O (Fig.3.5(f)) illustrate that the Si−H bonds at the surface are distorted due to the incorporation of more than one O atom at the back bonds.

Next, the possibility of O atom incorporation in the Si−H bonds, i.e. the formation of hydroxyl groups (−Si−OH) as proposed by Fink [23] is investigated with self limiting $HfCl_4$ chemisorption reaction. The surface OH density is estimated in combination with RBS and WCA measurements. More details on

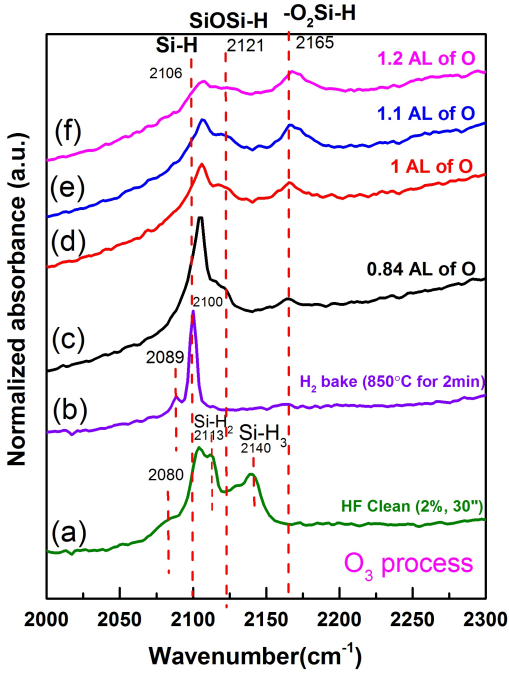

Figure 3.5: Normalized (normalized to maximum) ATR-FTIR spectra illustrating the evolution of Si–H peak (2100 cm^{-1}), SiOSi–H (2121 cm^{-1}) and $-O_2Si-H$ (2165 cm^{-1}) peak as a function of the deposited O-content after O_3 exposure.

the OH density estimation from $HfCl_4$ chemisorption is described in Appendix **??** and by Nyns [22]. Fig.3.6 shows the surface –OH density, estimated from the Hf-content, as a function of the total O-content. On the H–Si(100) surface, the estimated OH density is very low (0.03 atomic layers), which indicates the lack of suitable reactive sites (–OH groups) for $HfCl_4$ chemisorption [24]. Up to one O atomic layer, there is no significant increase in the Hf-content, indicating little or no formation of hydroxyl groups on the surface. This is in agreement with our above XPS and FTIR spectra, illustrating the presence of O atoms only at the back bonds. At an O-content > 1 AL, a linear increase in the OH-content is noticed.

It is concluded that at an O-content less than 1 AL, most of the O atoms are incorporated either in the dimer or at the back bonds. For O-content > 1 AL, the O atoms are incorporated in both the Si backbonds as well as in the Si–H bonds to form Si–OH groups. The reason of O atom insertion at

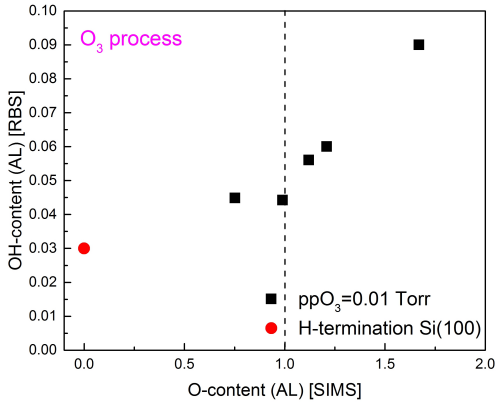

Figure 3.6: Estimated surface OH density (measured by $HfCl_4$ reaction) as a function of the deposited O-content [22]. Significant increase in OH density is observed for O-content > 1 AL. The estimation procedure is described in appendix **??**.

Si–H bond can be due to the disruption in the surface periodicity caused by the O atoms in back bonds, thereby weakening the Si–H bonds [21]. The WCA measurements are in agreement with the Hf experiments as shown in Fig. 3.7. Drastic degradation of WCA is observed for O >1 AL, illustrating an hydrophilic surface with escalated surface hydroxyl (Si–OH) density.

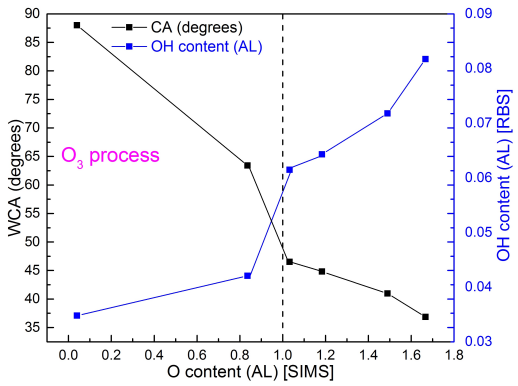

Figure 3.7: WCA and surface–OH density as a function of deposited O-content. Up to 1 AL of O-content, the surface is hydrophobic and there is no significant increase in the surface OH density.

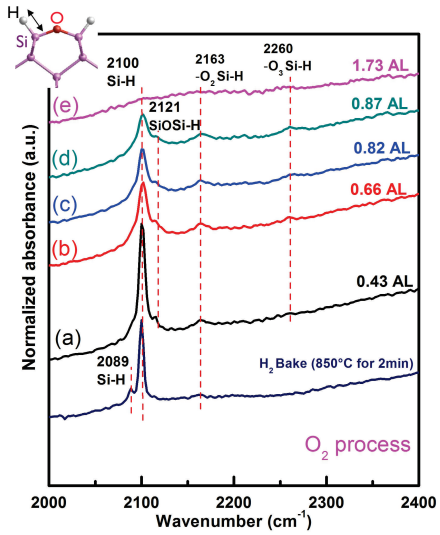

Figure 3.8: Normalized (normalized to maximum) ATR-FTIR spectra after O_2 chemisorption illustrating the evolution of Si–H (2100 cm^{-1}), SiOSi–H (2121 cm^{-1}), $-O_2Si-H$ (2165 cm^{-1}) and $-O_3Si-H$ (2260 cm^{-1}) peak as a function of the deposited O-content.

Similar ATR-FTIR analysis is investigated after O_2 exposure as shown in Fig.3.8. At a lowest O-content of ∼0.4 AL (Fig.3.8(a)), two features appear noticeable. One at 2121 cm^{-1} and another at 2163 cm^{-1} corresponding to the presence of one and two O atoms in the Si back bonds (–Si–O–SiH)/ Si dimer bonds (HSi–O–SiH) respectively [19]. With further increase in the O-content (from 0.66 to 0.87 AL), an additional peak appears at higher wave number (2260 cm^{-1})) corresponding to O_3Si-H vibrations [25, 26] (Fig.3.8(b)-(d)). The prominent peak of H–Si monohydride at 2100 cm^{-1} decreases in intensity and the peak width at half maximum increases. This suggests a decreased concentration of monohydrides distributed non-uniformly over the surface. In addition, the Si–H bond length remain unchanged, as noticed with a constant peak position (2100 cm^{-1}) irrespective of the O-content. At the highest O-content of 1.73 AL (Fig.3.8 (e)), the spectrum becomes featureless, indicating that all H atoms from the Si–H bonds are distorted yielding no signatures.

For a similar O-content of 0.8 AL, the insight on the difference surface structures after O_3 and O_2 exposure are illustrated in Fig.3.9. Two major differences are apparent

1. After O_2 reaction, the peak at 2260 cm^{-1} indicate the presence of O_3Si-H

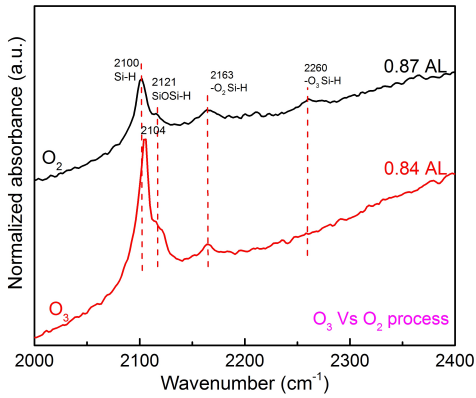

Figure 3.9: Comparison between the surface structures using ATR-FTIR spectra between O_2 reaction at 300°C and O_3 reaction at 50°C with similar O-contents on the surface.

surface species, where a clustering of 3 O atoms to a single Si atom [27]. On the other hand, the O_3 reaction yield a uniform distribution of O atoms at dimer and back bonds with Si−H vibrations at 2121 cm^{-1}.

2. After O_3 reaction, there is a shift in Si−H vibration frequency from 2100 to 2106 cm^{-1}. This is due to the change in Si−H bond length, caused by the higher electronegativity of O atoms uniformly distributed over the back bonds. Such a frequency shift is not observed for O_2 process, indicating a no change in the non-oxidized Si−H bond length despite the presence of O atoms [1, 21].

   Thus unlike O_3, after O_2 reaction, the appearance of the O_3Si−H vibrational mode together with the lack of frequency shift from H−Si indicate the existence of SiOx clusters as well as regions of H-terminated Si on the surface. The reason of such structure could be possibly due to the high O_2 process temperature of 300°C, which could have accelerated the surface oxidation. However, such interpretation is not been verified with O_3 and O_2 reaction at the same temperature of 300°C.

3.4 Experimental Si−O bond models

From the above complementary experimental characterization techniques, the following bond models after O_3 exposure (Fig.3.10) is proposed.

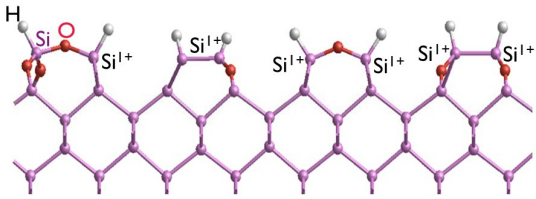

(a) 0.84 AL

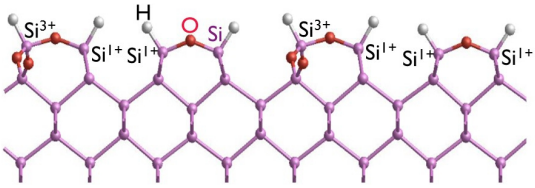

(b) 1 AL

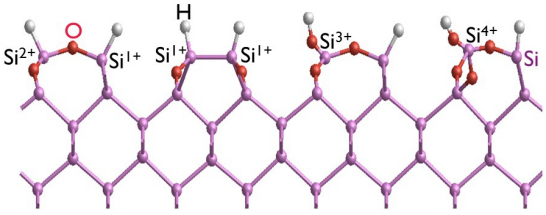

(c) 1.2 AL

Figure 3.10: Schematic of Si–O bond models at different O-contents after O_3 reaction on H–Si(100). (a) For $O < 1AL$, most Si atoms at 1+ oxidation state with O atoms mostly at back/dimer bonds of Si. (b) At 1 O AL, other back bonds of Si are populated resulting in higher Si oxidation states. (c) For O >1 AL, O atoms react with Si–H bonds forming surface hydroxyls (Si–OH). *NOTE: The structures are not optimized at their energy minima.*

After O_2 exposure, the simultaneous presence of O_3Si–H (in the form of SiOx clusters) and the un-strained Si–H result in O surface structures as shown in Fig.3.11.

By comparing experimental bond models with the Si-O structures in literature (discussed in Chapter 1), the Mears model [28] and the Tsu model [29] have similar structure. However, the structures are different from Nishio model (Rec-I and Rec-II) [30], who claims to have thermodynamic stable structures with less formation energies. The Nishio model structures are experimentally challenging.

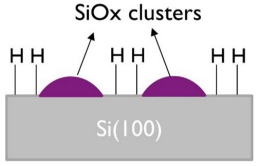

Figure 3.11: Si−O bond model after O_2 reaction on H−Si(100) at O-content <1 AL. The presence of O_3Si−H surface structures coupled with ideal Si−H bond lengths, indicate the presence of SiOx clusters as well as regions of H-terminated Si between them. The O-content > 1 AL lead to SiO_2 formation.

The experimental bond structures are compared with the theoretical simulation, where the formation energy of the O bonding structures at various bond position of 2×1 structure is calculated. From Table 3.13, the formation energy of O atom insertion in dimer is the lowest. This is followed by O atom at the back bonds of B1 and B3 positions as shown in Fig. 3.12. The insertion of O atoms at Si−H is difficult due to the higher formation energy. The O atoms at B4 and B5 positions are also difficult, as they are sterically protected.

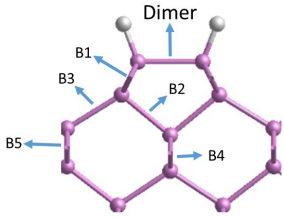

Figure 3.12: Schematic of formation energy calculation at different positions (B1 to B5 back bonds, dimer and at Si−OH).

Bond position	f(eV/atom)
Si−H	-3.50081
Dimer	-4.27154
B1	-3.40156
B2	-3.15275
B3	-3.74531
B4	-2.83745
B5	-3.14365

Figure 3.13: The formation energy (f in eV/atoms) of O bonding structures on 2×1 Si structure.

3.5 Conclusions

This chapter explains the O surface structures obtained after O_3 or O_2 exposure on H−Si(100) at 50°C and 300°C respectively for the deposition of O AL.

As the starting surface, after the pre-epi bake process, the surface consists of uniform distribution of strained mono-hydrides (Si−H). For O_3 process with O-content < 1 AL , most Si atoms exist is 1+ oxidation state with O atoms distributed uniformly at back (−OSiH) and/or dimer (HSi-O-SiH) bonds. This is the energetically favorable configuration, as the O atoms can overcome Si−Si bonding energy compared to the Si−H bond. It is further evident from the frequency shift of Si−H peak, corresponding to the strong Si−H bond caused by the electronegativity of O atoms in Si back bonds. With further increase in O-content, more O atoms at Si back bonds weaken the structure leading to incorporation of O atom at H−Si position. Unlike uniform distribution of O atoms, O atoms in the form of SiOx clusters (Si^{x+} with x>1) after O_2 chemisorption illustrate the impact of temperature (300°C) accelerating the surface oxidation. A simultaneous detection of both the O_3Si−H and the ideal Si−H bond length indicate the surface with SiOx clusters and also an un-strained Si−H bond structures on the surface.

Bibliography

[1] Suseendran Jayachandran, Annelies Delabie, Arne Billen, Harold Dekkers, Bastien Douhard, Thierry Conard, Johan Meersschaut, Matty Caymax, Wilfried Vandervorst, and Marc Heyns. Deposition of O atomic layers on Si (100) substrates for epitaxial Si-O superlattices: investigation of the surface chemistry. *Appl. Surf. Sci.*, 324:251–257, jan 2015.

[2] M. K. Weldon, K. T. Queeney, a. B. Gurevich, B. B. Stefanov, Y. J. Chabal, and Krishnan Raghavachari. Si–H bending modes as a probe of local chemical structure: Thermal and chemical routes to decomposition of H_2O on Si(100)-(2×1). *J. Chem. Phys.*, 113(6):2440, 2000.

[3] Olivier Vatel, Steven Verhaverbeke, Hugo Bender, Matty Caymax, Frederic Chollet, Bert Vermeire, Paul Mertens, Elie André, and Marc Heyns. Atomic Force Microscopy and Infrared Spectroscopy Studies of Hydrogen Baked Si Surfaces. *Jpn. J. Appl. Phys.*, 32(Part 2, No. 10B):L1489–L1491, oct 1993.

[4] H. Bender. Hydrogen Passivation of HF-Last Cleaned (100) Silicon Surfaces Investigated by Multiple Internal Reflection Infrared Spectroscopy. *J. Electrochem. Soc.*, 141(11):3128, 1994.

[5] V. A. Burrows, Y. J. Chabal, G. S. Higashi, K. Raghavachari, and S. B. Christman. Infrared spectroscopy of Si(111) surfaces after HF treatment: Hydrogen termination and surface morphology. *Appl. Phys. Lett.*, 53(11):998, 1988.

[6] Y. J. Chabal. Infrared spectroscopy of Si(111) and Si(100) surfaces after HF treatment: Hydrogen termination and surface morphology. *J. Vac. Sci. Technol. A Vacuum, Surfaces, Film.*, 7(3):2104, may 1989.

[7] Y.J. Chabal, E.E. Chaban, and S.B. Christman. High resolution infrared study of hydrogen chemisorbed on Si(100). *J. Electron Spectros. Relat. Phenomena*, 29(1):35–40, jan 1983.

[8] Y.J.Chabal Raghavachari. Surface Infrared study of Si(100)- (2x1)H. *Phys. Rev. Lett.*, 53(3):282–285, 1984.

[9] C. C. Cheng and J. T. Yates. H-induced surface restructuring on Si(100): Formation of higher hydrides. *Phys. Rev. B*, 43(5):4041–4045, feb 1991.

[10] H. Bender, S. Verhaverbeke, M. Caymax, O. Vatel, and M. M. Heyns. Surface reconstruction of hydrogen annealed (100) silicon. *J. Appl. Phys.*, 75(2):1207, 1994.

[11] Zhenjiang Cui and Christos G. Takoudis. Initial Oxidation of H-Terminated Si(100) in O_3 (950 ppm)/O_2 and Pure O_2. *J. Electrochem. Soc.*, 150(11):G694, 2003.

[12] Suseendran Jayachandran, Annelies Delabie, Jens Maggen, Matty Caymax, Roger Loo, Johan Meersschaut, Haraprasanna Lenka, Wilfried Vandervorst, and Marc Heyns. Chemical vapor deposition processes for the fabrication of epitaxial Si-O superlattices. *Thin Solid Films*, 557:36–41, apr 2014.

[13] Christian K Fink, Ken Nakamura, Shingo Ichimura, and Stephen J Jenkins. Silicon oxidation by ozone. *J. Phys. Condens. Matter*, 21(18):183001, may 2009.

[14] Z. H. Lu, S. P. Tay, T. Miller, and T.-C. Chiang. Process dependence of the SiO_2/Si(100) interface structure. *J. Appl. Phys.*, 77(8):4110, 1995.

[15] Y Enta, H Nakazawa, S Sato, H Kato, and Y Sakisaka. Silicon thermal oxidation and its thermal desorption investigated by Si 2p core-level photoemission. *J. Phys. Conf. Ser.*, 235:012008, jun 2010.

[16] G. Hollinger. Oxygen chemisorption and oxide formation on Si(111) and Si(100) surfaces. *J. Vac. Sci. Technol. A Vacuum, Surfaces, Film.*, 1(2):640, 1983.

[17] Michio Niwano, Nobuo Miyamoto Koji Kinashi, and Koji Honma Michio Niwano Jun ichi Kageyama. Infrared spectroscopic study of initial stages of ultraviolet ozone oxidation of Si(100) and (111) surfaces. *J. Vac. Sci. Technol. A Vacuum, Surfaces, Film.*, 12(2):465, mar 1994.

[18] Mathew D. Halls and Krishnan Raghavachari. Infrared Intensities of (SiH) on HSi(100)-2x1: Effect of O Incorporation and Agglomeration. *J. Phys. Chem. B*, 108(50):19388–19391, dec 2004.

[19] M. K. Weldon, K. T. Queeney, Y. J. Chabal, B. B. Stefanov, and K. Raghavachari. Mechanistic studies of silicon oxidation. *J. Vac. Sci. Technol. B Microelectron. Nanom. Struct.*, 17(4):1795, 1999.

[20] Douglas B. Mawhinney, John A. Glass, and John T. Yates. FTIR Study of the Oxidation of Porous Silicon. *J. Phys. Chem. B*, 101(7):1202–1206, feb 1997.

[21] Bhavin N. Jariwala, Cristian V. Ciobanu, and Sumit Agarwal. Initial oxidation stages of hydrogen- and styrene-terminated Si(100) surfaces: A molecular dynamics study. *Surf. Sci.*, 605(21-22):L61–L66, nov 2011.

[22] L. Nyns, A. Delabie, M. Caymax, M. M. Heyns, S. Van Elshocht, C. Vinckier, and S. De Gendt. HfO_2Atomic Layer Deposition Using $HfCl_4$ \ H_2O: The First Reaction Cycle. *J. Electrochem. Soc.*, 155(12):G269, 2008.

[23] Christian Fink and Stephen Jenkins. First-principles molecular dynamics of the initial oxidation of Si{001} by ozone. *Phys. Rev. B*, 78(19):195407, nov 2008.

[24] M. L. Green, M.-Y. Ho, B. Busch, G. D. Wilk, T. Sorsch, T. Conard, B. Brijs, W. Vandervorst, P. I. Raisanen, D. Muller, M. Bude, and J. Grazul. Nucleation and growth of atomic layer deposited HfO_2 gate dielectric layers on chemical oxide (Si–O–H) and thermal oxide (SiO_2 or Si–O–N) underlayers. *J. Appl. Phys.*, 92(12):7168, 2002.

[25] Marcus K Weldon, Boris B Stefanov, Krishnan Raghavachari, Y J Chabal, Bell Laboratories, Lucent Technologies, and Murray Hill. Initial H_2O-induced Oxidation of Si (100)- (2x1). *Phys. Rev. Lett.*, 79(15):2851–2854, 1997.

[26] Michio Niwano, Jun-ichi Kageyama, Kazunari Kurita, Koji Kinashi, Isao Takahashi, and Nobuo Miyamoto. Infrared spectroscopy study of initial stages of oxidation of hydrogen-terminated Si surfaces stored in air. *J. Appl. Phys.*, 76(4):2157, 1994.

[27] A Kurokawa and S Ichimura. High purity ozone oxidation on hydrogen passivated silicon surface. *Appl. Surf. Sci.*, 100-101:436–439, jul 1996.

[28] Nuo Xu, Hideki Takeuchi, Marek Hytha, Nyles W. Cody, Robert J. Stephenson, Byungil Kwak, Seon Yong Cha, Robert J. Mears, and Tsu-Jae King Liu. Electron mobility enhancement in (100) oxygen-inserted silicon channel. *Appl. Phys. Lett.*, 107(12):123502, sep 2015.

[29] Raphael Tsu and John C Lofgren. Structure of MBE grown semiconductor–atomic superlattices. *J. Cryst. Growth*, 227-228:21–26, jul 2001.

[30] Kengo Nishio, Augustin Lu, and Geoffrey Pourtois. Low-strain Si / O superlattices with tunable electronic properties : Ab initio calculations. *Phys. Rev. B*, 165303:1–10, 2015.

Chapter 4

Growth of Epitaxial Si on O ALs

Problem Statement: A second challenge during the growth of Si–O SLs is to obtain epitaxial Si layer on O AL/Si(100). The presence of oxygen on the Si surface can lead to the formation of oxide or precipitates, which can disturb the template of the Si substrate. This further results in growth of either non-crystalline layers or highly defective crystalline films with stacking faults and hillock structures [1–3]. Although the epitaxial deposition of Si on O AL has been realized by certain research groups [4, 5], the detailed understanding on the epitaxial seeding and the growth mechanisms of Si on O AL has been lacking

Objective: In this work, we investigate the influence of O surface structure and O-content on the epitaxial seeding and growth of Si layers on O AL. The epitaxial ordering of Si on O AL is understood, by addressing the following questions (i) Does the interface O-content has an impact on the epitaxial ordering of Si? If yes, (ii) How does the epitaxial seeding and growth proceed on different O surface structures? Then, (iii) Considering a low temperature epitaxial process, does the Si growth rate has any influence on the epitaxial quality of Si?

Organization of this chapter: The purpose of this chapter is to answer the above questions and to obtain insight in the epitaxial ordering of Si on O AL. The first section will describe the processes for Si homo-epitaxy at low temperature of 500°C. The second section focuses on the requirement of surface **O-content** less than 1 AL for enabling the epitaxial ordering of Si. Upon

seeding, the epitaxial ordering of Si is improved by **lowering the Si growth rate** compared to the Si homo epitaxy process. The latter is described in the third section. The impact of different **O surface structures** on the epitaxial nucleation and growth mechanism is studied in the last section.

4.1 Si homo-epitaxy

Choice of precursors: Among several Si precursors (SiH_4, Si_2H_6, Si_3H_8, SiH_2Cl_2, $SiHCl_3$), SiH_4 is used for the deposition of Si on O AL/Si(100). The choloro silanes are avoided for two reasons. First, the strong binding energy between Si – Cl bond require a high temperature process for the deposition. This is detrimental, as it can result in O diffusion during SL processing. Second, the foreign atoms other than Si and O might affect the sub-band engineering. Next, the motivation of using higher order silanes (Si_2H_6, Si_3H_8), is to obtain a high growth rate at low temperatures. However, as will be shown in the later sections that the lowest possible growth rate is required for realizing epitaxial Si on O AL with less structural defects. Hence the hgiher order silanes are not investigated for the SL work. The N_2 is used as carrier gas, as it was previously demonstrated that a high growth rate and low defect density is obtained compared to the H_2 carrier gas [6].

Si CVD is based on the dissociative adsorption of SiH_4 and H_2 desorption [7, 8]. Both these processes are controlled by the deposition temperature, which determines the Si growth rate. The growth rate of Si is enhanced from 0.4 nm min^{-1} to 2 nm min^{-1}, for the temperatures of 500°C to 550°C (Fig.4.1).

The H_2 desorption rate is the rate limiting step dictating the growth rate of Si. The activation energy of 40 kcal mol^{-1} is calculated (Fig.4.2) and is close to the reported value in litreature [9]. It corresponds to the activation barrier for the irreversible excitation of the H adatom. Thus for the given process conditions, the GR (growth rate) of Si is dictated by the H_2 desorption reaction, dominant for a low temperature process.

An additional process parameter that determines the growth rate and as such the quality of Si epitaxy, is the SiH_4 flow rate. The Si growth rate increases with the increase in SiH_4 flow (Fig.4.3), primarily due to the increase in the rate of adsorption. At 500°C, a smooth Si layers are obtained at a growth rate smaller than the critical value of 0.5 nm min^{-1} (corresponding to a SiH_4 flow of 100 sccm). A growth rate less than 0.5 nm min^{-1}, result in a slow arrival of the SiH_4 reactants as compared to the time required for surface diffusion and incorporation in the Si lattice. This results in epitaxial layers with smooth surface as observed from the optical microscopic images (inset in Fig.4.3). On

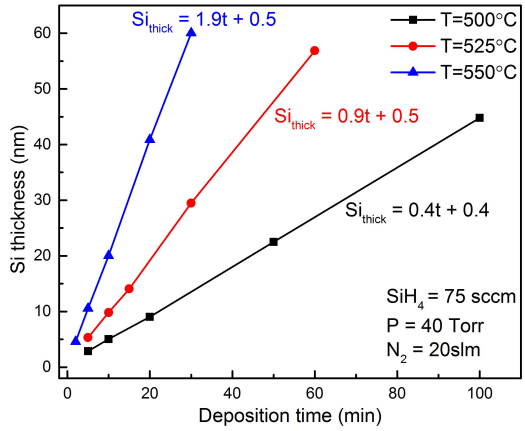

Figure 4.1: The deposited Si thickness at different deposition time and temperatures using SiH_4 flow of 75 sccm at P=40 Torr using N_2 carrier gas. The Si thickness is estimated from the mass balance measurements [10].

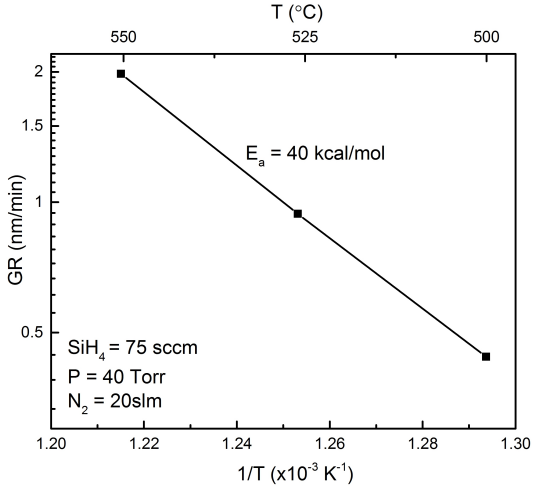

Figure 4.2: Arrhenius plot of Si GR. The activation energy of a Si CVD is estimated to be 40 kcal/mol. This value corresponds to the activation barrier for H_2 desorption mechanism [10].

the other hand at a growth rate of Si greater than 0.5 nm/min (SiH_4 flow rate $>$ 100 sccm), the Si layers are defective, as noticed on the microscopic images. An higher GR is observed at atmosphere pressure for a similar SiH_4 flow, could

be due to the SiH_4 decomposition in the gas phase than at the surface. Hence the SiH_4 flow rate, temperature and the total pressure of the reactor collectively determine the epitaxial quality of Si. The impact of carrier gas on the epitaxial quality is not investigated and is beyond the scope of this study.

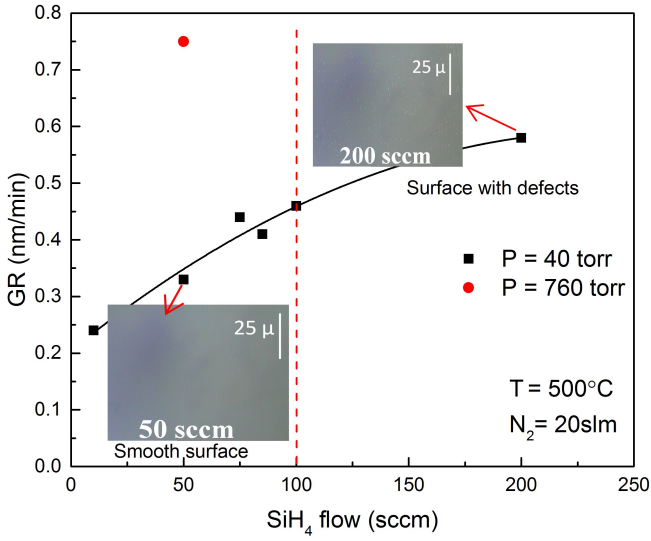

Figure 4.3: The Si GR vs SiH_4 flow at the temperature of 500°C using N_2 carrier gas at different pressures (40 and 760 Torr). The presence of surface defects are visualized from the optical microscopic images (inset) [10].

Crystalline Quality

The crystalline quality of the epitaxial Si layers is investigated using channeling in Rutherford Back scattering (RBS/C) spectra (Fig.4.4). If the ions are channeled through the sample, a negligible back scattering except from the surface atoms is detected. Then the grown layers are perfectly epitaxial. Otherwise, the displaced Si atoms are probed with increasing surface peak intensity corresponding to a poly- Si or an amorphous Si layers. In Fig.4.4, we notice the channeling spectrum (in red) with negligible back scattering yield, corresponding to a perfect crystalline Si layers on Si substrate. As the surface is indicated with an arrow, the Fig.4.4 indicates a depth profile of Si crystalline ordering.

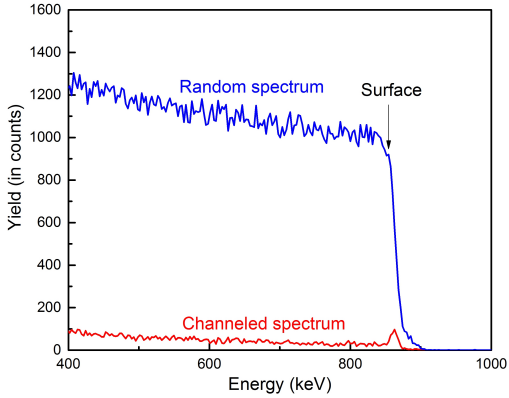

Figure 4.4: RBS/C spectra (in red) illustrating a defect free epitaxial Si layer on the Si (100) substrate at T = 500°C, SiH_4 = 75 sccm, N_2 = 20 slm and P = 40 Torr.

Interface Contaminations

It is well known that, the oxygen and carbon contaminants at the starting surface can degrade the epitaxial quality during growth [1, 3]. Fig.4.5, shows the depth profile of O and C at the epitaxial Si/ Si(100) interface. The contamination levels are close to the detection limit of SIMS, illustrating an epitaxial deposition is free from contamination.

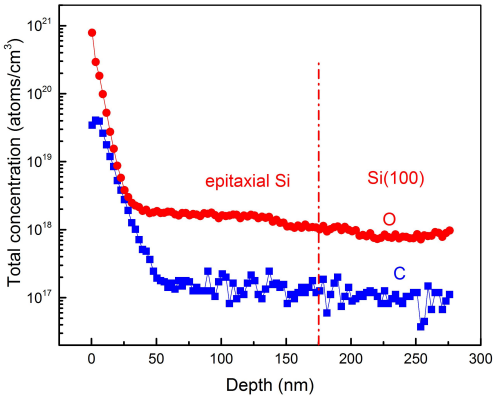

Figure 4.5: The depth profile of oxygen and carbon contaminations across the epitaxial Si/Si (100) interface [T = 500°C, SiH_4 = 75 sccm, N_2 = 20 slm and P = 40 Torr].

4.2 Impact of surface distortions on epitaxial quality of Si

For the growth of epitaxial Si – O SLs, the epitaxial ordering of Si is continued on O AL. I.e. the disruptions in the template due to the presence of O atoms at dimer/back bonds should be sufficiently minimal to allow the epitaxial seeding of Si. With increase in O-content,the distortions in the surface template is monitored by evaluating the epitaxial ordering/quality of Si layers.

Epitaxial ordering of Si on O AL, deposited by O_3 exposure is achievable in a narrow window of O-content between 0.7-0.9 AL at a given Si growth rate of 0.4 nm min^{-1}. For the O-content greater than 1 AL, the Si layers result in an amorphous deposition.

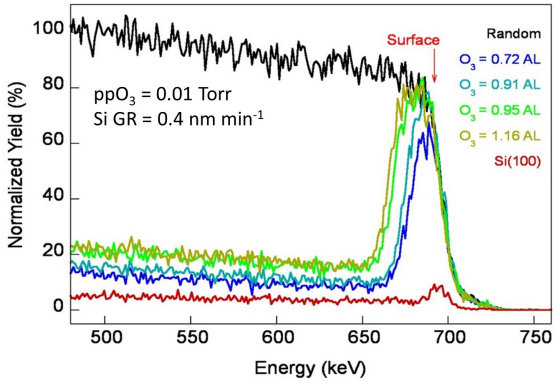

Figure 4.6: RBS/C spectra for the stack Si(60nm)/O AL/Si(100), at varying interface O-content. Enhanced back scattering yield with O-content is observed illustrating a transition to an a-Si layer [11]. The Si layers are deposited at T = 500°C, SiH_4 flow = 75 sccm, N_2 = 20 slm and at P = 40 Torr.

Fig.4.6 illustrate the RBS/C spectra of Si(60nm)/O AL/Si(100) layer as a function of the interface O-content. The Si(100) substrate is the reference with back scattering only from the surface atoms, a signature for a perfect epitaxial ordering of Si. With increase in interface O-content (from 0.72 to 1.16 AL), the back scattering yield increases in intensity illustrating an amorphous Si deposition. The surface distortions increases with O-content, resulting in Si adatoms at non-lattice sites strengthening the back scattering yield. The surface distortions primarily arise from the distortions in the template due to the incorporation of O atoms at dimer/back bonds of Si [11]. The surface distortions

were also visualized from the progressive frequency shift of the non-oxidized Si–H bond vibrations, as discussed in the section 3.3 [11, 12].

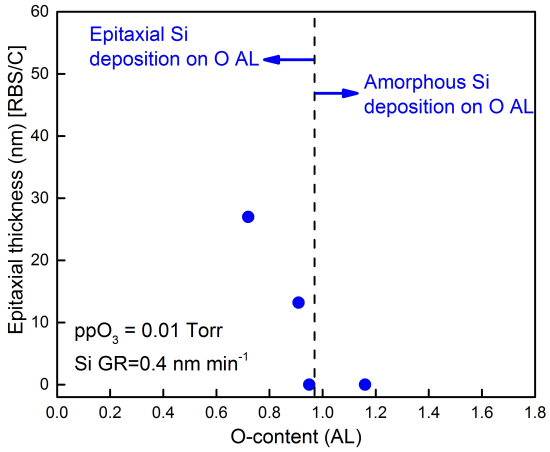

Figure 4.7: Epitaxial thickness obtained from RBS/C as a function of the deposited O-content after O_3 exposure. Epitaxial ordering on O AL is achieved between 0.7-0.9 O AL [10].

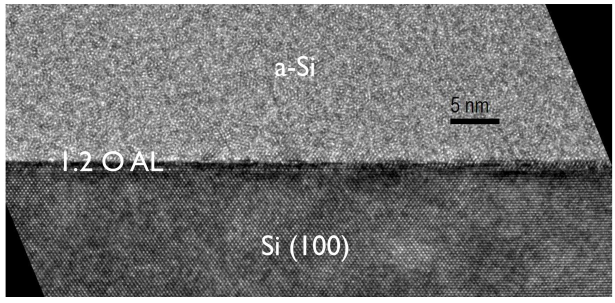

Figure 4.8: TEM image of Si layer grown at 0.4 nm min^{-1} on 1.2 O AL. The deposited layer is completely amorphous. A contrast change with a perfect lattice ordering of Si is noticed for Si(100) substrate [10].

The fraction of displaced Si atoms (F_{dis}), a measure to quantify the disorderliness of the deposited Si layer. It is calculated from the ratio of channeling yield to the random yield [13] as described in Eq. 4.1. The $Y_{(channel)}$ and $Y_{(rand)}$ are the back scattering yields by channeling and by incidence of ions with sample titling of 2° off axis respectively. $Y_{(surf)}$ is the back scattering yield due to the surface atoms. F_{dis} value of 0 and 1 indicate that the deposited layer

is completely crystalline and amorphous/poly-crystalline respectively. However the TEM investigations reveal that the layers are amorphous. F_{dis} values between 0 and 1 are related to the Si layers that consist of an epitaxial part at the bottom and an amorphous part on top. The epitaxial thickness can be estimated from the total thickness (60 nm) and F_{dis}, by assuming that the back-scattered ions are only from the amorphous top layer [14]. The thickness of the epitaxial Si layer is limited by the interface O-content as illustrated in the Fig.4.7. With increase in interface O-content, the surface distortions of the template increases, contributing to a lower epitaxial thickness. For O-content greater than 1 AL, the distortions are large enough to inhibit epitaxial seeding of Si leading to amorphous depositions.

$$F_{dis} = \frac{Y_{(channel)} - Y_{(surf)}}{Y_{(rand)}} \tag{4.1}$$

The TEM image indicates an amorphous deposition of Si on 1.2 O AL. The deposited O AL is continuous, as only a continuous O layer can completely prevent epitaxial ordering of Si with the substrate (Fig.4.8). The presence of any discontinuities would be revealed by the formation of Si crystal grains, aligned in epitaxy with the Si substrate, as the same process results in epitaxial deposition in the absence of O layer(section 4.1).

To conclude, the O-content < 1 AL plays a crucial role for enabling the epitaxial ordering of Si from the Si(100) substrate beneath. For O-content greater than 1 AL, the distortions are large enough with O atoms at Si–H bonds, inhibiting the epitaxial seeding of Si thereon.

4.3 Impact of Si growth rate

Besides the interface O-content, the Si growth rate play a crucial role in determining the epitaxial quality of Si on O AL. An epitaxial instead of amorphous Si deposition (Fig.4.8) on an O layer can be obtained by providing the adatoms a sufficient time for the surface diffusion during the initial stages of the Si deposition. This is achieved by lowering the Si growth rate from 0.4 nm min^{-1} to 0.2 nm min^{-1}. As such, the Si adatoms have more time to diffuse on the surface and to relax in an energetically favorable position and get incorporated in the Si crystal lattice. The deposition at 0.2 nm min^{-1} rate results in Si layers with a better epitaxial quality, as similar to the Si homo-epitaxial processes [6].

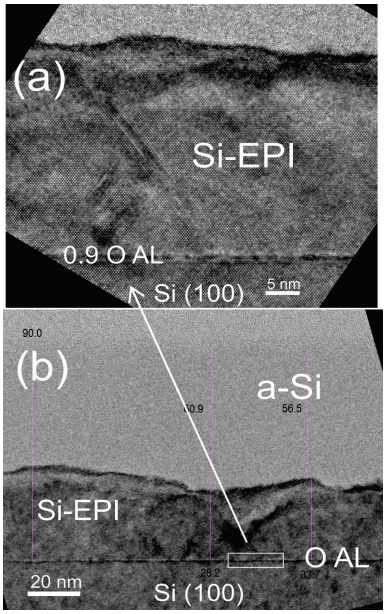

Figure 4.9: TEM image of epitaxial Si on 0.9 AL. The Si growth rate is lowered to 0.2 nm/min (SiH_4 flow = 10 sccm at T=500°C, P=40 Torr) for first 10 minutes enabling epitaxial ordering of Si on 0.9 AL. Later the Si growth rate is increased to 0.4 nm/min (SiH_4 flow = 75 sccm).(a)is the enlarged view of (b).

Thus a sub-AL interface O-content coupled with a sufficient time for surface diffusion of Si adatoms is a key for obtaining epitaxial Si deposition on O AL. Fig.4.9(b) shows the TEM image of epitaxial ordering of Si on O.9 O AL/Si(100) stack. The Si is grown at 0.2 nm min^{-1} for the first 10 minutes of deposition. As soon as a fully epitaxial Si layer of ∼2 nm is deposited, the growth rate is increased to its standard value of 0.4 nm min^{-1} in order to reach more reasonable deposition times.

Although quite some defects are still present, an epitaxial alignment of the deposited Si lattice with the Si(100) substrate can be clearly noticed from the magnified TEM image (Fig.4.9a). The epitaxial layer is quite defective with stacking faults in the [111] direction. Also, the epitaxial ordering is continued only until ∼30 nm of the total 90 nm deposited Si layer. The top part of the Si layer is amorphous.

A crystalline to amorphous phase transition well observed for a low temperature CVD process [18]. Eaglesham and co-workers linked the break in epitaxy to the surface roughening [19], while other arguments exist. Potential

explanations of breakdown other than surface roughening have been suggested by Thiesen and co-workers [20] who proposed that H buildup in the film bulk leads directly to the breakdown and by Platen and co-workers [21] who implicate the buildup of both bulk hydrogen and strain in the breakdown of CVD-grown films. Till date there are few reports that focused on the mechanisms of epitaxy, which have not conclusively determined the cause of breakdown [21, 22]. In our case, we suspect the breakdown in epitaxy is related to the epitaxial seeding of Si layers on O AL, which in turn depends on the O surface structures at Si/O/Si interface. This will be detailed in the section 4.4.

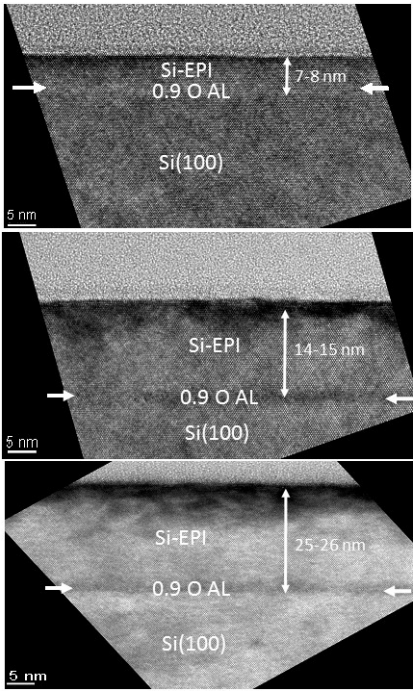

Figure 4.10: TEM image of epitaxial Si on 0.9 AL at varied Si thickness (a) 7-8 nm (b) 14-15 nm (c) 25-26 nm. The Si layers are grown at the lowest growth rate of 0.2 nm/min(SiH_4 flow = 10 sccm at T=500°C, P=40 Torr using N_2 carrier gas), ensuring sufficient time for diffusion and lattice incorporation [10].

Interestingly, the Si thickness required for the envisioned fabrication of Si-O SLs is much lower than the observed epitaxial thickness. Thus a series of samples with Si thickness of 7.5, 15 and 25 nm on the 0.9 AL are fabricated. The Si deposition rate was fixed at 0.2 nm min^{-1} during the complete deposition process in order to further minimize the defect density by allowing more time

for surface diffusion and lattice incorporation. The cross sectional TEM images however confirm that the layers are crystalline and epitaxially aligned with the Si(100) substrate (Fig.4.10 (a)-(c)). As no defects are detected from TEM images, the defect density is assumed to be below 1×10^{9} cm^{-2}.

The interface between the Si substrate and the epitaxial Si layer can be observed, indicating where the O AL should be. The growth rate is calculated to be 0.18 nm min^{-1}. The value does no seem to be much affected by the O atoms, but with a slight incubation period of ∼9 min (Fig.4.11) within the error limits of determining the Si thickness from TEM images. This is similar to the reported results for Si epitaxy on N sub-monolayers, where the incubation was attributed to decreased SiH_4 adsorption and/or decreased reaction rates at the nitrated sites [17].

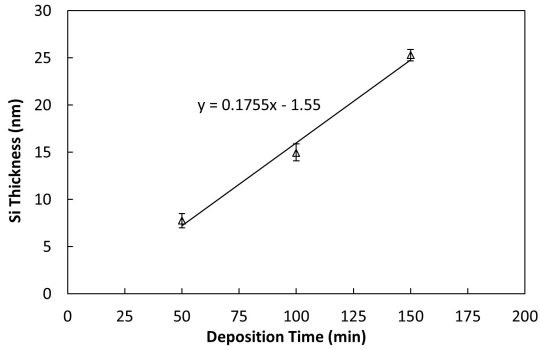

Figure 4.11: Si thickness measured by TEM as a function of the deposition time. The incubation period (x-intercept) for the Si deposition on the O AL (O_3 process) is ∼9 min [10].

The epitaxial thickness in Fig.4.7 is an estimation by assuming the F_{dis} is predominantly from the amorphous part of the Si layer, which is always not true. In practice, one can even expect a $F_{dis} = 1$ for a perfect poly-crystalline Si with the ions being completely de-channeled [23]. In this case, the argument on epitaxial thickness becomes invalid. For further considerations in this thesis, the epitaxial quality of Si is evaluated from the relative F_{dis} values instead of the epitaxial thickness.

The Fig. 4.12 summarizes the dependence of interface O-content and the Si growth rate on F_{dis}.

1. With similar process parameters, the Si growth rate is lowered from 0.4 to 0.2 nm min^{-1}. The t_{dep} is increased by 8 times, which seems to be sufficient for obtaining complete epitaxial Si layers ($F_{dis} = 0$). We clearly

notice a down shift of all the F_{dis} values by reducing the Si growth rate to 0.2 nm min^{-1}. Thus better quality of epitaxial layers are obtained at 0.2 nm min^{-1} than 0.4 nm min^{-1}.

2. Second, at Si growth rate of 0.2 nm min^{-1}, it is remarkable that epitaxial Si can be obtained even for the O-content slightly higher than 1 AL. On the one hand, this could indicate that the O layer is still not completely closed due to some non-uniformity in the O incorporation, allowing epitaxial seeding of the Si layer in the area of the holes [10]. On the other hand, it could be that the obtained O layer still contains some order from the Si(100) substrate, as previously suggested for other thin SiOx layers [24, 25]. The epitaxial seeding could as such be realized directly on such an ordered O layer even for O-contents exceeding 1 AL.

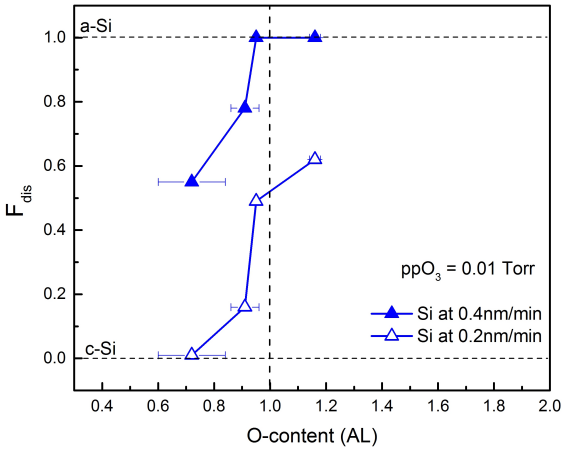

Figure 4.12: F_{dis} as a function of interface O-content (O_3 process) and the Si growth rate. [O AL: ppO_3=0.01 Torr at 50°C. Si deposition: $ppSiH_4$ = 20 and 150 mTorr, T= 500°C, N_2 carrier gas].

4.4 Growth mechanism of Si epitaxy on O surface structures

As discussed in Chapter 3, different O surface structures are deposited by exposure of O_3 or O_2 on H–Si(100). This section will describe the nucleation and growth of epitaxial Si on these O surface structures and their impact on the epitaxial quality.

Proposed Growth mechanism

The models for the epitaxial seeding of Si in the presence of O atoms with different surface structures are proposed. They are schematically shown in Fig.4.13 and Fig.4.14. For O_3 process, the epitaxial seeding of Si is possible at low O contents by a direct epitaxial growth mechanism (Fig.4.13). At a low O-content, the O atoms are configured in the Si−Si back/dimer bonds of the H-terminated Si (100) and distributed uniformly over the Si surface. Most of the Si−H bonds will not have any bonding to the O atom [11]. Despite the presence of O atoms, the surface can still provide a well-ordered template for epitaxial seeding of Si thereon. Nucleation can occur by H desorption from both the H−SiOSi and H−Si sites, after which SiH_4 can adsorb, react, diffuse and incorporate into the lattice.

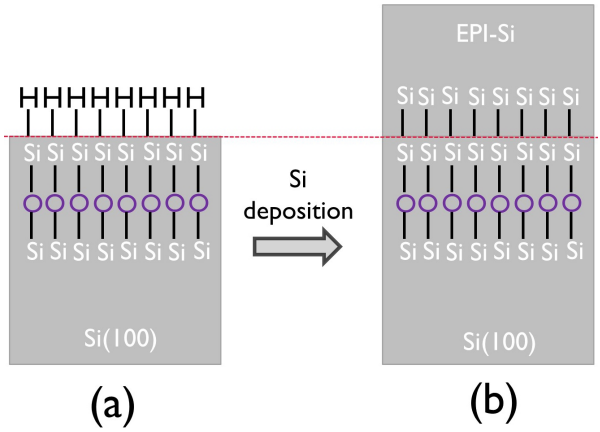

Figure 4.13: (a) Schematic of O AL on Si (100) after O_3 exposure at 50°C. The O atoms are at dimer/back bonds of 2×1 H-terminated Si (100). (b) Schematic of direct epitaxial growth mechanism, where the O atoms at dimer/back bond structures, still provide an ordered template for the epitaxial seeding of Si thereon [26].

For the O atomic layers after O_2 reaction, the surface consist of regions with SiOx clusters and regions of H-terminated Si. Epitaxial seeding can proceed, but only from the H-terminated regions between the SiOx clusters (Fig.4.14(b)). On the SiOx clusters, the SiH_4 molecules lack an ordered template and hence an epitaxial seeding cannot occur. Any Si deposited directly on the SiOx clusters is expected to be amorphous or polycrystalline. However, as we will show below the epitaxial Si layers can be formed by epitaxial lateral overgrowth if the SiOx

clusters are sufficiently small, similar as previously suggested by Tsu and his co-workers [5].

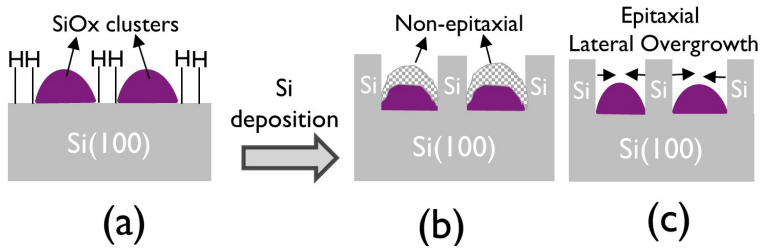

Figure 4.14: Schematic representation of epitaxial seeding of Si on O AL deposited by O_2 process. (a) After O_2 exposure on H−Si (100) at 300°C, the surface results in regions with SiOx clusters and regions with (non-oxidized) H-terminated Si. (b) Epitaxial seeding on H-terminated regions. (c) Growth of epitaxial Si on SiOx clusters by epitaxial lateral overgrowth mechanism [26].

Experimental verification

The above growth models and the impact of different O surface structures are investigated by monitoring the roughness evolution of the Si layer grown thereon at a constant growth rate of 0.2 nm min^{-1} on a fixed interface O-content of 0.7±0.2 AL. For the O_3 process, the surface is rather uniformly distorted after the O deposition, inducing minor surface roughness during Si growth. On the other hand, for the O_2 process, the SiOx clusters create local distortions of the structure and thus create the surface undulations [1]. These structural deformations create roughness during the Si growth and thus the evolution of surface roughness with thickness is representative of the epitaxial seeding and growth mechanisms of Si on O AL (Fig. 4.15 and 4.16).

Based on the AFM images shown in Fig.4.15, we can calculate the rms roughness as a function of Si thickness (Fig.4.16). The O_3 process with a Si deposition rate of 0.2 nm min^{-1}, there is no significant increase in the surface roughness for a Si thickness up to 25 nm. With a further increase in thickness up to 75 nm, the surface roughness increases only to 0.7 nm. The large size particles/defects of maximum of 80 nm in height and 300 nm in diameter are excluded during the root mean square (rms) roughness calculation, since coverage is less than 3% over the surface. The increase in roughness is similar to the roughness evolution for low temperature homo-epitaxial Si on an O-free Si surface obtained after a standard pre-epi H_2 bake. This illustrates that the presence of O AL has only has a minor impact on the epitaxial ordering of Si

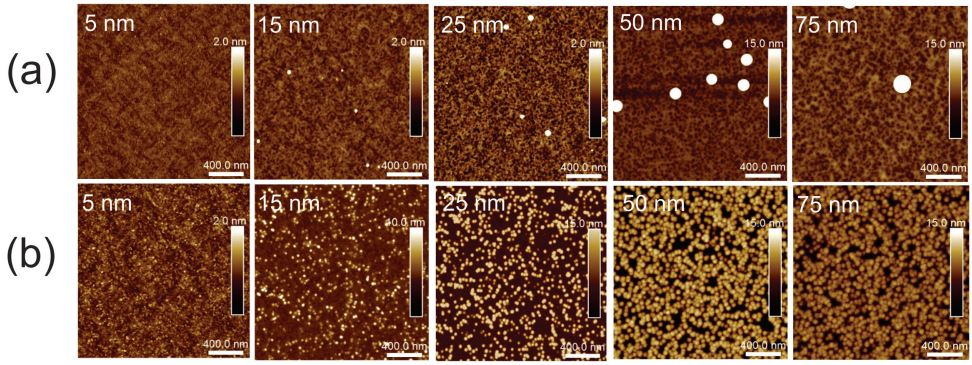

Figure 4.15: Surface morphology of Si grown at 0.2 nm min^{-1} on 0.7±0.2 O AL at different Si thickness. The Si thickness are indicated on the images (a) For O_3 process (b) For O_2 process.

as the surface still represents a template for epitaxial seeding. Most likely, the single O atoms in the Si−Si back bonds/dimer bonds have only la imited impact on the adsorption of SiH_4 molecules and the surface diffusion of Si adatoms, yielding epitaxial Si layers with similar roughness. The increase in roughness after 25 nm of homo-epitaxial Si, is presumed to be due to kinetic factors related to the low temperature process. Indeed at low temperature epitaxial processes the adatoms have limited surface mobility i.e. some Si adatoms do not have sufficient relaxation time to reach their energetically minimum position contributing to the surface roughness at atomic scale [27].

In contrast, for the O_2 process, the roughness of the Si layer increases drastically as a function of the thickness. As seen from Fig.4.15(b), from 15 nm of Si, defects start to appear on the surface. With increasing thickness up to 50±5 nm, the bearing percentile of the defects increase from 25% to 80 %, indicating the defects are distributed more uniformly over the surface contributing to the global increase in surface roughness (Fig.4.16). The origin of surface roughness is further analyzed. First, the presence of the SiOx clusters on the Si surface can contribute to the higher roughness. Second, during the Si deposition, the epitaxial seeding occurs effectively on the regions of H-terminated sites, but not on the SiOx clusters. The presence of the SiOx clusters leads to the formation of stacking fault defects originating from the interface with the SiOx clusters, contributing to the increase in surface roughness [1]. On the SiOx clusters, the deposited Si is either non-epitaxial or epitaxial as grown by a lateral overgrowth mechanism from the Si deposited on the H-terminated area. In addition, the possible existence of different Si phases as well as a difference in lateral versus vertical growth rate can also explain the increased

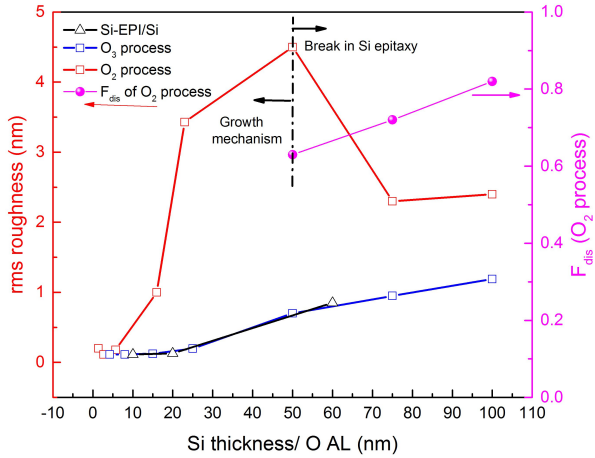

Figure 4.16: Surface roughness evolution of Si deposited at a growth rate of 0.2 nm/min (SiH_4 flow = 10 sccm at T=500°C, P=40 Torr using N_2 carrier gas) on 0.7±0.2 O AL after O_3 and O_2 exposure. On the right y axis, show the increase in F_{dis} with Si thickness for O_2 based process.

surface roughness. One or a combination of the above mechanisms can explain the increased surface roughness as observed in Fig.4.16. After 50±5 nm of Si deposition, a decrease in the absolute roughness is measured corresponding to the break in epitaxial ordering of Si. The surface roughness remains constant after 75 nm of Si due to the further growth of amorphous Si.

As shown experimentally here, the break in epitaxial ordering of Si is primarily due to the accumulation of surface roughness during growth. The roughness arises from the defects, which are nucleated during the epitaxial seeding of Si between SiOx clusters.

Epitaxial breakdown of Si on O AL

The break in Si epitaxy on O AL for O_2 process is confirmed by RBS/C spectra. For a 23 nm of Si layer deposited on O AL, the F_{dis} of 0.2 indicates that the layer is almost (80%) epitaxial (magenta curve in Fig.4.17). With increasing thickness to 50±5 (green curve in Fig.4.17) and to 100±15 nm (red curve in Fig.4.17), the F_{dis} increases approximately from 63 to 82 nm respectively. This indicates that the thickness of the amorphous part of the layer increases with Si thickness. This is in agreement with the decreased surface roughness with

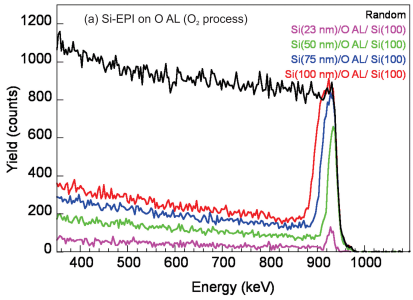

Figure 4.17: Si at different thickness (23-100 nm) on O AL (O_2 process). The transition from epitaxial to a-Si is observed.

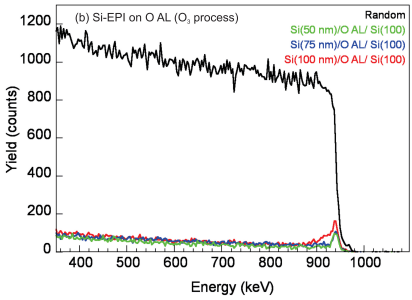

Figure 4.18: Si at different thickness (50-100 nm) on O AL. All the samples are mainly epitaxial.

increase in Si thickness from 50±5 to 100±15 nm as discussed from AFM studies.

In contrary for the O_3 process with similar Si growth rate, the deposited Si layers up to 75±15 nm is fully crystalline while for 100±15 nm is mostly crystalline except a few monolayers of a-Si at the top, as confirmed by the low back scattering yield (Fig.4.18). The cause for such a break in epitaxial ordering of Si on O AL from O_2 process can be attributed to the higher surface roughness, i.e. due to the stacking faults and/or defects created by epitaxial seeding of Si between SiOx clusters [1]. These results can be in agreement with the observations of kinetic surface roughening and defect accumulation models proposed by Karpenko and Jorke respectively for the MBE based processes [27–29]. However it is still debatable on the possible mechanism for epitaxial breakdown as Teplin and co-workers concluded that neither the accumulation of the surface roughness nor the strain causes a break in epitaxial ordering of Si during hot-wire CVD processes [30]. The further investigation on the break in epitaxial ordering is beyond the scope of this thesis.

The F_{dis} of Si layers on O ALs, deposited by O_3 and O_2 are compared in Fig.4.19. At first instance, the F_{dis} increases with increase in interface O-content for O_3 and O_2 processes. This is in agreement with our above understandings. Second, For the O_2 process, following observations were recorded in comparison with the O_3 process,

1. For a Si growth rate of 0.4 nm min^{-1}, the F_{dis} values are lower for the O_2 process as compared to the O_3 process.

2. For a Si growth rate of 0.4 nm min^{-1}, the O_2 process can enable epitaxial

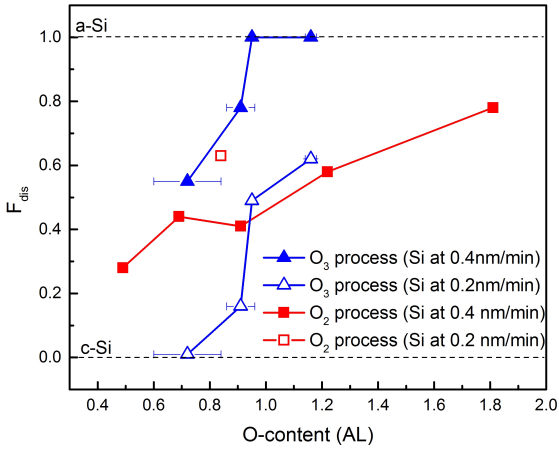

Figure 4.19: Fraction of displaced atoms (F_{dis}) as a function of interface O-content and Si growth rate (closed symbols for 0.4 nm min^{-1} and open symbols for 0.2 nm min^{-1}) for O_2 (red) and O_3 (blue) process.

ordering of Si ($F_{dis} < 1$) up to O-contents as high as 1.8 AL. On the other hand, the O_3 process results in complete amorphous Si deposition ($F_{dis} = 1$) for O AL with an O-content greater than 1 AL.

3. Unlike O_3 process, we observe less dependence of the Si growth rate on epitaxial quality of Si for the O_2 process.

These experimental observations are in agreement with our proposed epitaxial lateral overgrowth mechanism. For the O_2 process, the epitaxial ordering can be obtained by epitaxial seeding from H-terminated Si area in between the SiOx clusters. For the Si growth rate of 0.4 nm min^{-1}, this enables epitaxial Si with enhanced quality as compared to the O_3 process, resulting in a lower F_{dis} values. In addition, a partial epitaxial layer ($F_{dis} < 1$) can be grown at O-contents significantly higher than 1 AL (e.g. up to 1.8 AL), as long as the SiOx does not form a closed layer. As expected, no significant effect of the Si growth rate on epitaxial ordering is noticed, as both low and high Si growth rate can enable epitaxial ordering on H-terminated Si regions between SiOx clusters.

4.5 Conclusion

The understanding on the growth of epitaxial Si layers on O AL is described in this chapter. The (a) surface distortions due to O atoms (b) Si growth rate (c) the O surface structures have crucial impact on the epitaxial quality of Si. They are enumerated below

1. The growth temperature and the SiH_4 flow rate are one of the significant parameters that determine the growth rate for Si homo epitaxy.

2. Epitaxial ordering of Si on O AL deposited by O_3 reaction is achievable only with the interface O-content less than 0.9 AL. For the O-content greater than 1 AL, the Si layers result in an amorphous deposition. With increasing interface O-content, the surface distortions increases, thereby yielding Si adatoms at non lattice sites contributing to a lower epitaxial thickness. The surface distortions primarily arise from the distortions in the template due to the incorporation of O atoms at dimer/back bonds of Si. For O-content greater than 1 AL, the distortions are large enough inhibiting the epitaxial seeding of Si thereon. The surface distortions were visualized from the progressive frequency shift of the non-oxidized H−Si bond vibrations.

3. Another parameter impairing the epitaxial quality of Si is by providing sufficient time for the surface diffusion of Si adatoms. This is achieved by lowering the SiH_4 flux rate. As such, the Si adatoms have sufficient time to diffuse on the surface and to relax in an energetically favorable position and contribute to the growth. Unlike Si homo-epitaxy, epitaxial Si on O AL is deposited with an incubation time of $\sim$9 min.

4. Different O surface structures after O_3 and O_2 reactions result in different growth mechanism of epitaxial Si thereon. After the O_3 chemisorption, the epitaxial growth of Si can occur by a direct epitaxial growth mechanism on H−Si and H−SiOSi sites by H_2 desorption and SiH_4 adsorption. On the other hand, after O_2 chemisorption, epitaxial seeding of Si can occur on the H-terminated regions between SiOx clusters and the epitaxial growth continues further by an epitaxial lateral overgrowth mechanism.

5. The latter epitaxial seeding mechanism generate defects at the interface with the SiOx clusters, contributing to much higher surface roughness leading to an epitaxial breakdown. The epitaxial lateral overgrowth mechanism can enable epitaxial ordering even on O-contents greater than 1 AL and has a less dependence on the arrival rate of SiH_4 flux.

Bibliography

[1] R. H. Finch, H. J. Queisser, G. Thomas, and J. Washburn. Structure and Origin of Stacking Faults in Epitaxial Silicon. *Journal of Applied Physics*, 34(2):406, 1963.

[2] K.V.Ravi. *Imperfections and Impurities in Semiconductor Silicon*. Wiley-Interscience publication, illustrate edition, 1981.

[3] S. W. Bedell, T. N. Adam, a. Turansky, and D. K. Sadana. Role of interfacial oxygen on the quality and strain stability of pseudomorphic silicon-germanium layers grown on Si substrates. *Journal of Crystal Growth*, 316(1):101–105, 2011.

[4] R Tsu, A Filios, C Lofgren, K Dovidenko, and C G Wang. Silicon Epitaxy on Si (100) with Adsorbed Oxygen. *Electrochemical and Solid state letters*, 1(2):80–82, 1998.

[5] Raphael Tsu and John C Lofgren. Structure of MBE grown semiconductor–atomic superlattices. *Journal of Crystal Growth*, 227-228:21–26, jul 2001.

[6] P. Meunier-Beillard, M. Caymax, K. Van Nieuwenhuysen, G. Doumen, B. Brijs, M. Hopstaken, L. Geenen, and W. Vandervorst. N_2 as carrier gas: An alternative to H_2 for enhanced epitaxy of Si, SiGe and SiGe:C. *Applied Surface Science*, 224(1-4):31–35, 2004.

[7] S.M. Gates. Kinetics and mechanisms of surface reactions in epitaxial growth of Si from SiH_4 and Si_2H_6. *Journal of Crystal Growth*, 120(1-4):269–274, may 1992.

[8] Martin L Hammond. *Silicon Epitaxy by Chemical Vapor Deposition*.

[9] Kumar Sinniah, Michael G. Sherman, Lias B. Lewis, W. Henry Weinberg, John T. Yates, and Kenneth C. Janda. New Mechanism for Hydrogen Desorption from Covalent Surfaces: The Monohydride Phase on Si(100). *Physical Review Letters*, 62(5):567–570, jan 1989.

[10] Suseendran Jayachandran, Annelies Delabie, Jens Maggen, Matty Caymax, Roger Loo, Johan Meersschaut, Haraprasanna Lenka, Wilfried Vandervorst, and Marc Heyns. Chemical vapor deposition processes for the fabrication of epitaxial Si-O superlattices. *Thin Solid Films*, 557:36–41, apr 2014.

[11] Suseendran Jayachandran, Annelies Delabie, Arne Billen, Harold Dekkers, Bastien Douhard, Thierry Conard, Johan Meersschaut, Matty Caymax, Wilfried Vandervorst, and Marc Heyns. Deposition of O atomic layers on

Si (100) substrates for epitaxial Si-O superlattices: investigation of the surface chemistry. *Applied Surface Science*, 324:251–257, jan 2015.

[12] Boris B. Stefanov and Krishnan Raghavachari. Oxidation of Si(100)2 × 1: thermodynamics of oxygen insertion and migration. *Surface Science*, 389(1-3):L1159–L1164, nov 1997.

[13] Qiang Zhao Dingyu Chen, Xiting Lu, Zhonghuang Xia, Xuemei Wang. Damage production in silicon by MeV Si cluster irradiation. *Nuclear Instruments and methods in Physics Research B*, 129:392–396, 1997.

[14] H P Lenka, B Joseph, P K Kuiri, G Sahu, P Mishra, D Ghose, and D P Mahapatra. Study of low energy Si and Cs implantation induced amorphization effects in Si(1 0 0). *Journal of Physics D: Applied Physics*, 41(21):215305, nov 2008.

[15] D W Greve. UHV / CVD and related growth techniques for Si and other materials. pages 1–20.

[16] Robert Hull. *Properties of Crystalline Silicon*. 1999.

[17] Junichi Murota, Masao Sakuraba, and Bernd Tillack. Atomically Controlled Processing for Group IV Semiconductors by Chemical Vapor Deposition. *Japanese Journal of Applied Physics*, 45(9A):6767–6785, sep 2006.

[18] Charles W. Teplin, Eugene Iwaniczko, Bobby To, Helio Moutinho, Paul Stradins, and Howard M. Branz. Breakdown physics of low-temperature silicon epitaxy grown from silane radicals. *Physical Review B - Condensed Matter and Materials Physics*, 74(December):4–8, 2006.

[19] D J Eaglesham, H Gossmann, and M Cerullo. Limiting thickness hepi for epitaxial growth and room temperature Si growth on Si(100). *Physical Review Letters*, 65(10):1227–1230, 1990.

[20] Jack Thiesen, Howard M. Branz, and Richard S. Crandall. Explanation of the limiting thickness observed in low-temperature silicon epitaxy. *Applied Physics Letters*, 77(22):3589, 2000.

[21] J. Platen, B. Selle, I. Sieber, S. Brehme, U. Zeimer, and W. Fuhs. Low-temperature epitaxial growth of Si by electron cyclotron resonance chemical vapor deposition. *Thin Solid Films*, 381:22–30, 2001.

[22] J. Schwarzkopf, B. Selle, W. Bohne, J. Röhrich, I. Sieber, and W. Fuhs. Disorder in silicon films grown epitaxially at low temperature. *Journal of Applied Physics*, 93(9):5215–5221, 2003.

[23] F. Benyaich, F. Priolo, E. Rimini, C. Spinella, and P. Ward. Kinetic and structural study of the epitaxial realignment of polycrystalline Si films. *Journal of Applied Physics*, 71(2):638, 1992.

[24] K. T. Queeney, N. Herbots, Justin M. Shaw, V. Atluri, and Y. J. Chabal. Infrared spectroscopic analysis of an ordered Si/SiO_2 interface. *Applied Physics Letters*, 84(4):493–495, 2004.

[25] N Herbots, J.M Shaw, Q.B Hurst, M.P Grams, R.J Culbertson, David J Smith, V Atluri, P Zimmerman, and K.T Queeney. The formation of ordered, ultrathin SiO_2/Si(100) interfaces grown on (1×1) Si(100). *Materials Science and Engineering: B*, 87(3):303–316, 2001.

[26] Suseendran Jayachandran, Arne Billen, Bastien Douhard, Thierry Conard, Johan Meersschaut, Alain Moussa, Matty Caymax, Hugo Bender, Wilfried Vandervorst, Marc Heyns, and Annelies Delabie. Growth mechanisms for Si epitaxy on O atomic layers: Impact of O-content and surface structure. *Appl. Surf. Sci.*, 384:152–160, oct 2016.

[27] Cao Zexian. *Thin Film Growth Physics, material science and applications*, volume 103. 2011.

[28] O P Karpenko and D J Eaglesham. Surface roughening during low temperature Si(100) epitaxy. *J. Appl. Phys.*, 82(August):1157–1165, 1997.

[29] D. J. Eaglesham. Semiconductor molecular-beam epitaxy at low temperatures. *Journal of Applied Physics*, 77(8):3597, 1995.

[30] Charles W. Teplin, Matthew Page, Eugene Iwaniczko, Kim M. Jones, Robert M. Ready, Bobby M. To, Helio M. Moutinho, Qi M. Wang, and Howard M. Branz. Roughness, impurities and strain in low-temperature epitaxial silicon films grown by tantalum filament hot-wire chemical vapor deposition. *MRS Proceedings*, 910:12–14, 2006.

Chapter 5

Growth of Epitaxial Si-O SLs

Problem Statement: As the process for the epitaxial growth of Si on O AL is understood, the next question is whether the Si and O deposition process sequence can be repeated multiple times for SL growth or the defects propagate ultimately causing an epitaxial breakdown? How does the epitaxial quality, surface morphology, Si-O bond structures vary with the SL parameters (number of Si-O periods, Si thickness between O ALs).

The schematic of epitaxial Si-O SL is shown in Fig.5.1. As the epitaxial seeding and growth of Si on O ALs deposited by O_2 process is defective, only the O_3 process is considered for SL growth. The O AL on Si (100) substrate is hereafter mentioned as O $AL_{(1)}$ and the first epitaxial Si layer on O $AL_{(1)}$ is mentioned as Si-$EPI_{(1)}$. The nomenclature for the subsequent periods follow the appropriate subscripts.

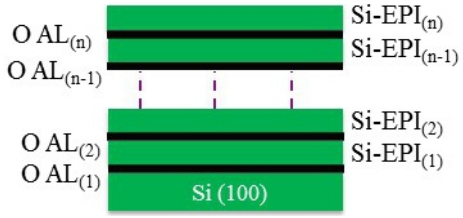

Figure 5.1: Schematic of Si – O SL structure. The "n" denotes the number of Si – O periods i.e. O $AL_{(n)}$ and Si-$EPI_{(n)}$ correspond to the n^{th} period of SL [1].

Objective: The first objective is to obtain insight in the processes for the fabrication of epitaxial Si-O SLs with multiple periods. The controlled deposition

of "n" multiple O ALs (O $AL_{(1)}$, O $AL_{(2)}$...O $AL_{(n)}$) and the impact of Si thickness sandwiched between O ALs (Si–$EPI_{(1)}$, Si–$EPI_{(2)}$...Si–$EPI_{(n)}$) on the epitaxial quality of the entire SLs is the subject of this chapter. The second objective is to investigate the surface morphology and the bonding structures as a function of the SL parameters.

Organization of this chapter: The repeat of the Si and O deposition process results in epitaxial breakdown. To understand the cause we investigate the surface termination of Si-$EPI_{(1)}$ as discussed in the first section. Second, we demonstrated that the surface termination of Si-$EPI_{(1)}$ has an impact on the O_3 reaction and hence the deposited O-content (O $AL_{(2)}$). Third, the epitaxial quality of Si-$EPI_{(2)}$ grown thereon was investigated by RBS/C linking epitaxial quality with the deposited O-content of O $AL_{(2)}$. At last, with these understandings, we develop a growth process leading to structures containing n=2 to n=5 periods of fully crystalline Si–O SL with good epitaxial quality.

5.1 Si-O repeat process

A complete crystalline structure is not obtained when the O and Si deposition processes described in our previous chapters (Chapter 3 and Chapter 4) are solely repeated [2, 3]. Fig.5.2(a) shows a cross sectional TEM image of Si and O layers repeated twice. Above the Si (100) substrate, a thin line representative for O $AL_{(1)}$ is observed. Although there is a continuation of crystalline ordering for Si–$EPI_{(1)}$ on O $AL_{(1)}$, the structure is rather defective with many stacking faults. It is difficult to distinguish O $AL_{(2)}$ on Si-$EPI_{(1)}$. The Si-$EPI_{(2)}$ is partly amorphous with a thickness variation of 10 ± 2 nm. This indicates the loss of an ordered template for the epitaxial seeding.

Previously we have demonstrated that the epitaxial ordering of Si is strongly dependent on the interfacial O-content [4]. The Si deposition on an O-layer with an O-content greater than 1 AL will lead to an amorphous deposition due to the increased surface distortions caused by the O atoms [1, 3, 5] (section 4.2).

Therefore, we have analyzed the O content of O $AL_{(1)}$ and O $AL_{(2)}$ of similar structures after Si encapsulation (Fig. 5.2(b)). The O $AL_{(1)}$, deposited directly on the Si (100) substrate, corresponds to an O-content of 0.5 AL. As the H–Si(100) surface is perfectly flat and chemically uniform after wet and high temperature pre-epi bake, a controlled chemisorption reaction of O_3 will result in a sub-AL O-content enabling the epitaxial ordering of Si-$EPI_{(1)}$ layer [2, 3]. In contrast, the O $AL_{(2)}$ corresponds to an O-content of 1.1 AL. As the Si-$EPI_{(1)}$ layer is grown at a temperature of 500°C using N_2 carrier gas, the surface is chemically more reactive as compared to the well-ordered H

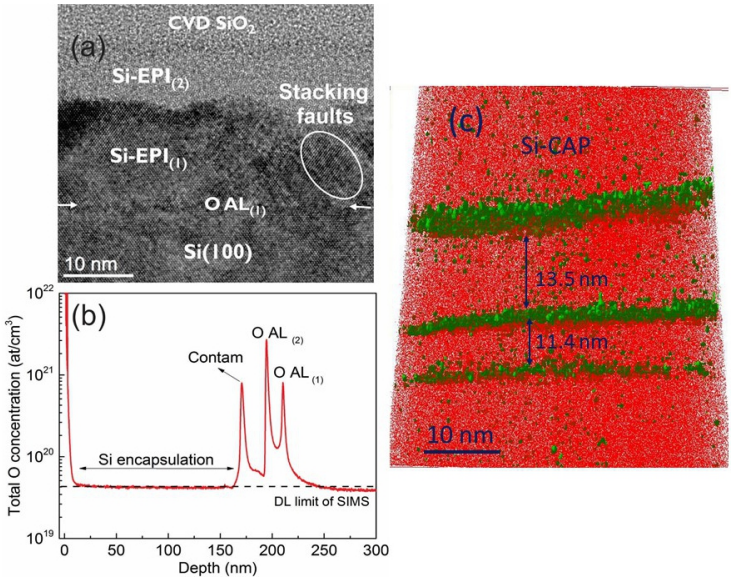

Figure 5.2: (a) Cross section TEM image of a Si-O SL (x2). The position of the O $AL_{(1)}$ is indicated by the arrows. The Si-$EPI_{(1)}$ is crystalline with thickness of 12 $\pm$ 2 nm and Si-$EPI_{(2)}$ is amorphous with thickness of 10 $\pm$ 2 nm. (b) Oxygen depth profile measured with SIMS. The O $AL_{(2)}$ (1.1 AL) is higher as compared to the O $AL_{(1)}$ (0.5 AL). The contamination peak marks the interface between Si-$EPI_{(2)}$ layer and the encapsulated Si-layer. DL - detection limit of SIMS. (c) 3D reconstruction of O atoms using APT.

terminated Si(100) surface, which can explain the higher O content of O $AL_{(2)}$ layer. Hence, the O content of the O $AL_{(2)}$ is too high to allow epitaxial ordering of Si-$EPI_{(2)}$. Additional reasons for the epitaxial breakdown of Si-$EPI_{(2)}$ could be a high concentration of defects and surface roughness generated during the non-uniform nucleation of the Si-$EPI_{(1)}$ layer [4, 6–8]. Although we believe that the combination of all these effects could cause a break in epitaxial ordering, we will show in the sections below that the O-content at higher periods (O $AL_{(2)}$ ... O $AL_{(n)}$) plays a dominant role in controlling the epitaxial quality of entire SL structure.

It is noticed that, SIMS could detect a clear and confined peak of O $AL_{(2)}$, while its corresponding lattice distortions are not detected from TEM. To confirm the presence of O AL and to visualize the uniformity of O atom distribution in each period, we perform APT analysis whose sensitivity is down to an atom level (Fig.5.2(c)). Clear distinction between 2 O ALs are noticed.

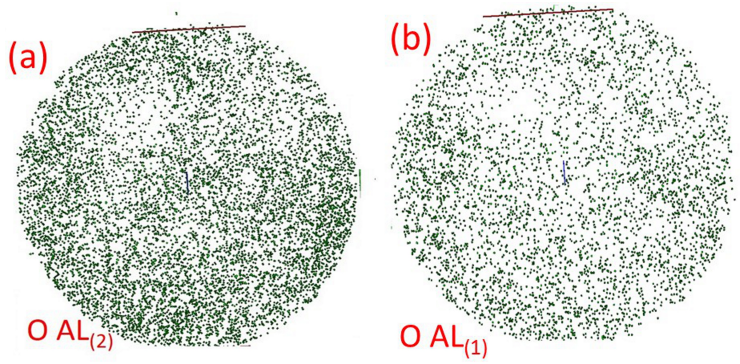

Figure 5.3: 2D view of O $AL_{(2)}$ and O $AL_{(1)}$, illustrating the uniformity of the O atoms. They are obtained by slicing at the position of O ALs from Fig.5.2(c).

The O concentration, obtained by O depth profiles in APT and SIMS are in agreement with each other. The uniformity of the O atoms are noticed from the cross sectional view of Fig.5.2(c), exactly at the position of O ALs. In Fig.5.3, the O $AL_{(2)}$ has more O atoms than O $AL_{(1)}$. A less uniform distribution of O atoms is noticed at both the layers. Thus unlike SIMS, APT is more advanced with the additional insight on the uniformity of the O layers.

5.2 Intermediate surface passivation (ISP) of Si-$EPI_{(1)}$

The growth of defect free epitaxial Si – O SLs is possible with O $AL_{(2)}$...O $AL_{(n)}$ layers at sub AL O-content. This is achieved by H-passivation of Si-$EPI_{(1)}$... Si-$EPI_{(n-1)}$ surface prior to deposition of O $AL_{(2)}$...O $AL_{(n)}$ layers respectively. In other words, we try to mimic the Si-$EPI_{(1)}$ surface similar to a chemically uniform H – Si(100) surface. Thus the potential to induce H-passivation by *in-situ* H_2 anneals directly after the Si-$EPI_{(1)}$ deposition is investigated.

The relative concentration and ordering of Si mono-hydrides are estimated from FTIR spectroscopy. Fig.5.4(a) shows the FTIR spectra for Si – H vibrations (2000-2200 cm^{-1}) of Si(100) surface after the pre-epi bake. The sharp peak at 2100 cm^{-1} corresponds to the symmetric vibrations of strained monohydrides (Si_3 – H) [8, 9]. This is considered as a reference with 100% of ordered Si – H concentration. The peak width at half maximum (FWHM) of 6 cm^{-1}, as determined from Lorentzian fitting, illustrates a uniform distribution of

homogenous monohydrides [8, 10]. After the low temperature epitaxial growth of Si (Si-EPI), the FWHM remains the same, but the relative concentration of ordered monohydrides decreases to 28% (Fig.5.4(b)).

In order to increase the concentration of ordered mono-hydrides on Si-EPI$_{(1)}$/O AL$_{(1)}$ surface, a post-deposition *insitu* H_2 anneal at 600°C for a duration of 5 min is performed. A well-defined sharp peak (FWHM = 7 cm^{-1}) is detected and the ordered monohydride concentration increases to 46% (Fig. 5.4(d)). The H_2 adsorption is limited by the reaction of H_2 and the surface dangling bonds. The concentration of surface monohydrides is dependent on the H_2 partial pressure and the thermal budget [11, 12]. In contrast, by N_2 anneal at similar conditions, the concentration of surface hydrides remain similar to the Si-EPI/Si (100) surface. Yet the ordering is impaired with a FWHM of 22 cm^{-1}, illustrating a less uniform distribution of the monohydrides (Fig.5.4(c)).

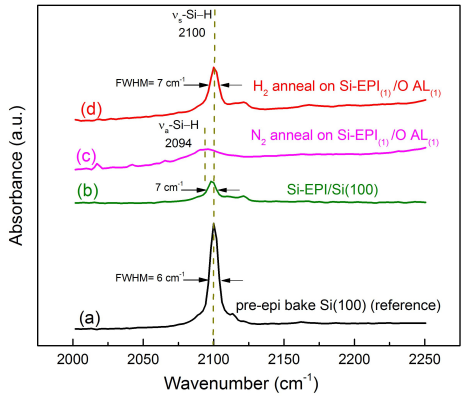

Figure 5.4: ATR-FTIR spectra on the (a) Si(100) surface after high temperature pre-epi bake at 850°C for 2 minutes (reference). (b) Si-EPI/Si (100) surface (c) Si-EPI$_{(1)}$/O AL$_{(1)}$/ Si(100) surface after N_2 anneal. (d) Si-EPI$_{(1)}$/O AL$_{(1)}$/ Si(100) surface after H_2 anneal. The Si-EPI$_{(1)}$ of 3 nm thick. Anneal is performed at 600°C for 5 minutes.

5.3 Impact of ISP on O-content and epitaxial ordering

Next, we investigate the role of the H_2 and N_2 surface treatments on the deposited O-content and the crystalline ordering of the subsequent Si layer. For this purpose, we investigate these processes on an homo-epitaxial Si surface (Si-

EPI), as shown in Fig.5.5. The new set of samples and their process conditions are summarized in Table 5.1.

Figure 5.5: Schematic of Si (50-75nm)/O AL/Si-EPI/Si (100) structure under RBS/C investigation. The sample description is summarized in Table 5.1.

The Si(100) surface after pre-epi bake (reference) contains the highest concentration of mono-hydrides. After the O_3 chemisorption reaction, the O-content is 0.7 $\pm$ 0.1 AL. For an homo-epitaxial Si surface (Si-EPI) without any post-deposition anneals (sample A), the deposited O-content is 1 AL. The increased O-content can be explained by a higher O_3 reactivity due to a reduced surface monohydrides (section.5.2). After a post-deposition anneal in N_2 (sample B), the deposited O-content increases further to 1.3 $\pm$ 0.1 AL. This is due to the lack of ordered surface monohydrides [13, 14]. Finally, after the post-deposition anneal in H_2 (sample C), the O_3 reaction results in an sub- AL O-content of 0.6 $\pm$ 0.1 ALs. This is primarily due to the surface passivation of ordered monohydrides, thereby lowering the O_3 sticking probability and hence a sub-AL O-content.

Thus, for a similar O deposition process (ppO_3 = 0.01 Torr and a deposition time of 50 ms), different O-contents are deposited, as the surface reactivity depends on the concentration and ordering of surface mono-hydrides. In other words, the number of reaction sites altered by surface termination.

The different O-content caused by different surface terminations, has an impact on the epitaxial ordering of Si(50-75 nm) thereon (Fig.5.6). For the reference and for sample C, with the lowest surface O-content, the Si layer is mainly epitaxial as only a surface peak representative at the top most layer is detected. On the other hand for sample A and B, with an increased O-content, the back scattering yield as a function of energy follows the random spectra. This illustrate an amorphous Si layer [3], whose thickness is indicated in Table 5.1.

Most of the deposited Si layers (88%) are amorphous for Sample A and B. For the reference and sample C, the layers are epitaxial. Thus, the Si layer deposited on an O AL with O-content $\geq$ 1 AL result in amorphous deposition.

Sample	Stack	Post-deposition Anneal	Relative Si−H conc. (%)	O-content (AL)	Total-Si thick-ness (nm)	a-Si thick-ness (nm)
Reference	H−Si(100) surface	-	100	0.7±0.1	75	1.3
Sample A	Si-EPI/Si	No-Anneal	28	1	71	33
Sample B	Si-EPI/Si	N_2(600°C 5 min)	28	1.3	75	66
Sample C	Si-EPI/Si	H_2(600°C 5 min)	46	0.6	50	4

Table 5.1: Summary of the samples under RBS/C investigation. The reference is the H−Si(100) after pre-epi bake. Sample A consists of Si-EPI/Si(100) with no post-deposition anneals. The Si-EPI/Si(100) stack with N_2 and H_2 post-deposition anneals are labeled as sample B and C respectively. The O AL and the Si(50-75 nm) thereon is deposited on all the samples (Fig.5.5). The deposited O-content is quantified from SIMS and the thickness of the amorphous layers is quantified from RBS/C.

This is predominantly due to the increased occupation of O atoms at dimers and back-bonds of Si disrupting the surface causing surface distortions [5]. As a consequence, a significant amount of Si atoms do not grow on lattice sites leading to an amorphous deposition. To conclude, the intermediate surface passivation with H has significant impact on the O-content of O $AL_{(2)}$...O $AL_{(n)}$ layers and the epitaxial ordering of Si (Si-$EPI_{(2)}$... Si-$EPI_{(n)}$) layers thereon.

5.4 2-period Si-O SLs with ISP

From the above investigations, we conclude that a process for creation of a Si-O SL with more than one period must include a surface H passivation step, creating an H-passivated surface prior to the deposition of O ALs. As such, we demonstrate the growth of fully crystalline 2-period Si−O SLs.

A fully epitaxial 2-period Si-O SL with Si thickness of 15 nm between O ALs is grown by the process sequence including surface passivation anneals (Fig. 5.7). Minimal structural defects are detected from TEM investigations. The uniform change in contrast from TEM could indicate the presence of O ALs and is confirmed from ^{16}O depth profile (Fig.5.8). The O-content of O $AL_{(1)}$ layer

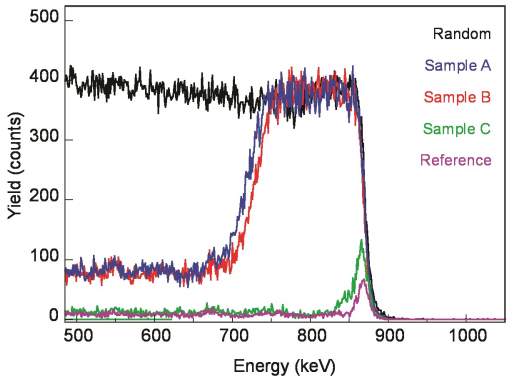

Figure 5.6: RBS/C spectra of stack as shown in Fig.5.5. The sample details of reference, A, B and C are mentioned in Table 5.1. A slight hump towards the lower energy for sample C illustrates the disorder in the film.

is 0.8 ± 0.1 AL. Due to the H_2 passivation step on Si-EPI$_{(1)}$, the O-content in O AL$_{(2)}$ is 0.6 ± 0.1 AL. Obviously, the H-termination of the Si-EPI$_{(1)}$ lowers the deposited O-content to a sub-AL content, enabling the epitaxial seeding of Si thereon (Si-EPI$_{(2)}$). This is in clear contrast to the structure without intermediate surface passivation (Fig.5.2(a)).

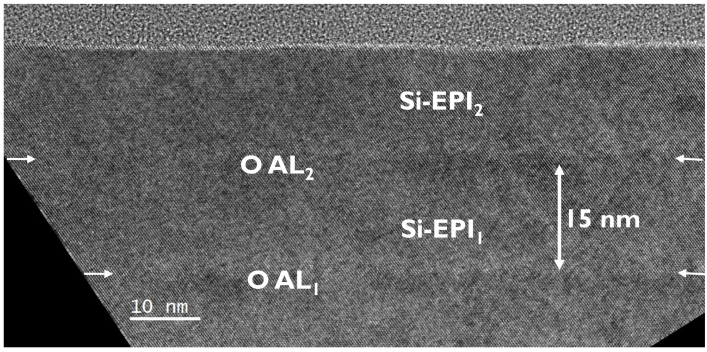

Figure 5.7: Cross sectional TEM image of 2-period Si-O SLs fabricated by the process sequence with ISP. The Si thickness between O ALs, viz. Si-EPI$_{(1)}$ and Si-EPI$_{(2)}$ is 15 nm. The uniform change in contrast may correspond to the presence of 2 O ALs indicated by arrows.

Thermal stability

Though Fig. 5.7 shows defect free TEM structures, the ^{16}O depth profile indicate a O diffusion towards the substrate. Such diffusion is circumvented by the H_2 anneal at a similar temperature of Si deposition i.e. 500°C without comprising on the O-content and the epitaxial quality of the Si layer. The reason for such ^{16}O diffusion is not known and is subjected to future study.

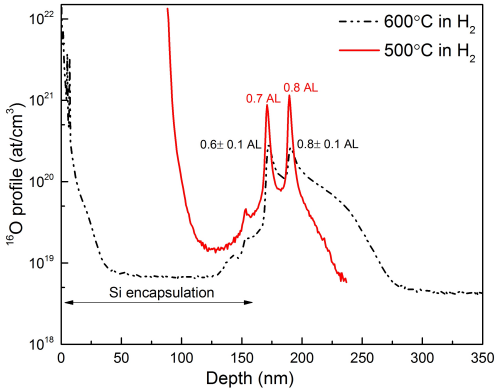

Figure 5.8: ^{16}O depth profile of 2-period Si-O SL at two different ISP anneals (500°C and 600°C in H_2 for 5 minutes). Significant reduction in ^{16}O diffusion is noted for 500°C anneal.

5.5 5-period Si-O SLs with ISP

To materialize the effective mass engineering, one prefers structures with a higher number of periods (n > 2) as well as with thinner Si layers. Note for instance that after 2-period growth, the surface roughness already has increased to 1.6 nm, versus 0.1 nm for an epitaxial Si layer of a comparable thickness. The combination of Si and O deposition with intermediate H-passivation is repeated 5 times to grow a 5-period Si–O SL structure. Fig.5.9 shows the TEM of 5-period Si–O SL with ∼7 nm Si layers between the O ALs.

Remarkably, the entire structure remains fully epitaxial even with the introduction of five O layers. Nevertheless, stacking faults are formed mostly within the top 2 periods of the SL. The thickness of the Si layers is quite well controlled in the lower periods. The topmost Si layer is on average slightly thinner than the other Si layers (5 instead of 7 nm). However an increased Si thickness is observed locally at the defected regions (indicated by circles),

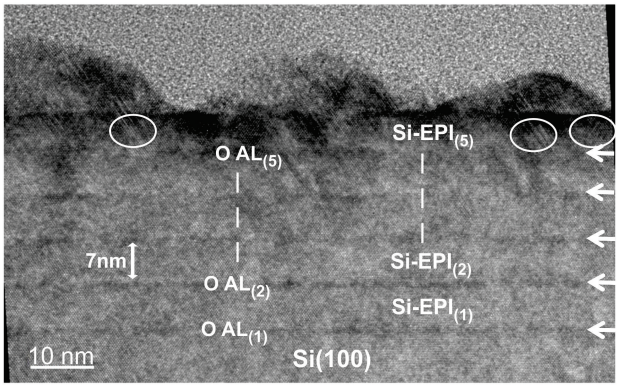

Figure 5.9: TEM image of a Si-O SL (5×) with ∼7 nm of Si between O layers. The topmost Si layer is defective with stacking faults, contributing to the global surface roughness.

leading to the global surface roughness. The defective structure can be expected to contain additional active chemisorption sites for the incoming SiH_4 molecules, contributing to a non-uniform film growth.

The accumulation of surface distortions caused by the multiple O ALs and the surface roughness from the stacking fault defects can be minimized by decreasing the Si thickness. This would be advantageous for device integration as well, since the inversion region could be within the SL region. The TEM image of a 5-period Si–O SL with Si layers of 3 nm is shown in Fig.5.10. The structure is epitaxial and a uniform change in contrast at the position of the O ALs is well distinguished. Note that the contrast change is not confined to one atomic layer, probably due to the roughness of the interfaces in combination with the integration over the TEM lamellae thickness.

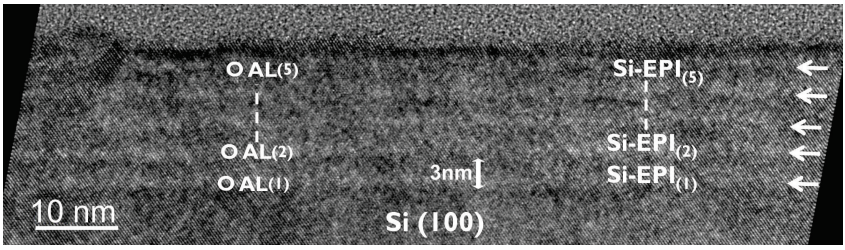

Figure 5.10: TEM image of a SL (5×) with ∼3 nm of Si between O layers. The uniform distortions are indicated by arrows corresponding to the position of O ALs.

The structural changes in surface morphology as a function of the number of Si – O periods and the total Si thickness is monitored by AFM (Fig. 5.11). The root mean square (rms) roughness increases as a function of the number of Si-O periods and with Si thickness.

1. With the increase in Si – O periods, it is likely that the O atoms occupy most of the Si back bonds, thereby disrupting the Si surface and contributing to the atomic surface roughness.
2. These surface distortions accumulate with thickness resulting in the formation of stacking fault like defects (Fig. 5.9), which can further increase the global surface roughness.

As seen in Fig. 5.11 (inset), the defects nucleate with increase in Si – O periods (SL(2×) to SL(5×)). In addition, a uniform distribution of defects is noticed with increase in total thickness for SL(5×) from 15 nm to 35 nm.

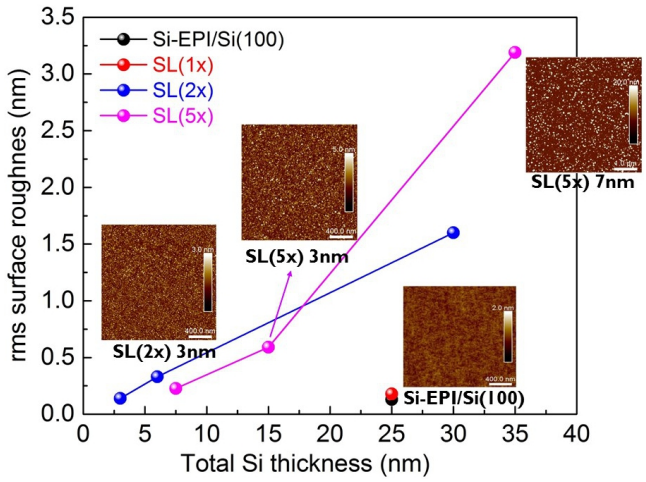

Figure 5.11: Evolution of rms roughness Vs total Si thickness. All the structures are fabricated with the process sequence including H_2 passivation anneals at 600°C for 5 min.

5.5.1 Surface structures

In addition to the structural information across the depth (Fig.5.10) and the surface morphology (Fig. 5.11), the chemical bonding of the O layers in

the overall Si-O SL structure is investigated. We therefore compare the FTIR spectra of the surfaces after the deposition of first (O $AL_{(1)}$) and the fifth (O $AL_{(5)}$) O AL in Fig. 5.12 (a) and (b) respectively.

After the deposition of O $AL_{(1)}$, most of the O atoms are incorporated in the Si–Si dimers or back bonds (as indicated by the Si–H vibrational mode at 2121 cm^{-1}), with the Si surface atoms mainly at the 1+ oxidation state [5]. After the deposition of the O $AL_{(5)}$ on Si-$EPI_{(4)}$, the O atoms are positioned at one and two back bonds of Si with a typical signatures at 2121 cm^{-1} and 2167 cm^{-1} respectively. The additional surface distortions caused by the presence of multiple O ALs weaken other Si back bonds, which are susceptible for 2^{nd} O atom insertion.

This is in agreement with XPS, where only the signals corresponding to Si^{1+} and Si^{2+} oxidation states are detected (Fig. 5.13). The Si^{3+} and Si^{4+} are not observed. Thus the XPS confirms the absence of precipitates, clusters or SiO_2 islands in the overall SL structure. Note that the Si-O SL with O back bond structures are considered to be thermodynamically meta-stable and can withstand thermal budget during device processing as suggested by Mears research group [15].

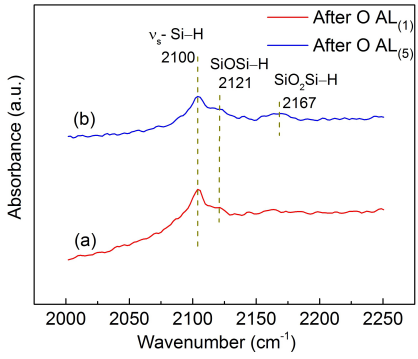

Figure 5.12: ATR-FTIR spectra comparing the O bonding structures after the deposition of (a) O $AL_{(1)}$ and (b) O $AL_{(5)}$.

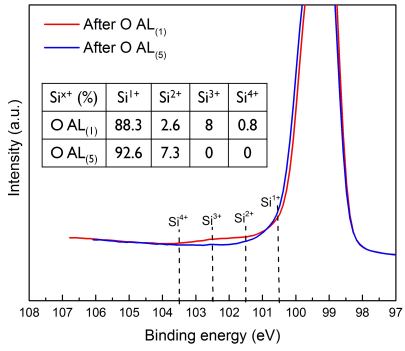

Figure 5.13: XPS of Si 2p angle integrated spectra after O $AL_{(1)}$ and O $AL_{(5)}$ deposition. The table (inset) indicates the relative Si sub oxide (Si^{x+} concentration (%)) after peak fitting. Negligible Si^{3+} and Si^{4+} states indicate the absence of O clusters.

5.6 Conclusion

In this chapter, we have investigated the processes for fabrication of epitaxial Si−O SLs with more than 2 periods. A simple combination of Si and O process yield defective structures when applied repeatedly. The epitaxial breaks down in consecutive periods is correlated to an high O-content greater than 1 AL at O $AL_{(2)}$...O $AL_{(n)}$ layers. The O-content is reduced to less than 1 AL by improving the surface H-termination through H_2 anneals. Such termination limit the O_3 reaction, leading to an O layer at sub AL-content enabling the growth of defect free Si−O SL structures. The oxidation state of Si with multiple O layers is 1+ or 2+ illustrating the absence of SiO_x clusters or precipitates.

Bibliography

[1] Suseendran Jayachandran, Eddy Simoen, Koen Martens, Johan Meersschaut, Hugo Bender, Matty Caymax, Wilfried Vandervorst, Marc Heyns, and Annelies Delabie. Quasi Two-Dimensional Si-O Superlattices : Atomically Controlled Growth and Electrical Properties. *ECS Journal of Solid State Science and Technology*, 5(7):P396–P403, 2016.

[2] A. Delabie, S. Jayachandran, M. Caymax, R. Loo, J. Maggen, G. Pourtois, B. Douhard, T. Conard, J. Meersschaut, H. Lenka, W. Vandervorst, and M. Heyns. Epitaxial Chemical Vapor Deposition of Silicon on an Oxygen Monolayer on Si (100) Substrates. *ECS Solid State Letters*, 2(11):P104–P106, sep 2013.

[3] Suseendran Jayachandran, Annelies Delabie, Jens Maggen, Matty Caymax, Roger Loo, Johan Meersschaut, Haraprasanna Lenka, Wilfried Vandervorst, and Marc Heyns. Chemical vapor deposition processes for the fabrication of epitaxial Si-O superlattices. *Thin Solid Films*, 557:36–41, apr 2014.

[4] Suseendran Jayachandran, Arne Billen, Bastien Douhard, Thierry Conard, Johan Meersschaut, Alain Moussa, Matty Caymax, Hugo Bender, Wilfried Vandervorst, Marc Heyns, and Annelies Delabie. Growth mechanisms for Si epitaxy on O atomic layers: Impact of O-content and surface structure. *Applied Surface Science*, 384:152–160, oct 2016.

[5] Suseendran Jayachandran, Annelies Delabie, Arne Billen, Harold Dekkers, Bastien Douhard, Thierry Conard, Johan Meersschaut, Matty Caymax, Wilfried Vandervorst, and Marc Heyns. Deposition of O atomic layers on Si (100) substrates for epitaxial Si-O superlattices: investigation of the surface chemistry. *Applied Surface Science*, 324:251–257, jan 2015.

[6] M. Nerding, L. Oberbeck, T. A. Wagner, R. B. Bergmann, and H. P. Strunk. Single to polycrystalline transition in silicon growth by ion-assisted deposition at low temperatures. *Journal of Applied Physics*, 93(5):2570, 2003.

[7] H Jorke. Kinetics of ordered growth of Si on Si(100) at low temperatures. *Physical Review B*, 40(3):2005–2008, 1989.

[8] Olivier Vatel, Steven Verhaverbeke, Hugo Bender, Matty Caymax, Frederic Chollet, Bert Vermeire, Paul Mertens, Elie André, and Marc Heyns. Atomic Force Microscopy and Infrared Spectroscopy Studies of Hydrogen Baked Si Surfaces. *Japanese Journal of Applied Physics*, 32(Part 2, No. 10B):L1489–L1491, oct 1993.

[9] Marcus K Weldon, Boris B Stefanov, Krishnan Raghavachari, Y J Chabal, Bell Laboratories, Lucent Technologies, and Murray Hill. Initial H_2O-induced Oxidation of Si (100)- (2x1). *Physical Review Letters*, 79(15):2851–2854, 1997.

[10] H. Bender. Hydrogen Passivation of HF-Last Cleaned (100) Silicon Surfaces Investigated by Multiple Internal Reflection Infrared Spectroscopy. *Journal of The Electrochemical Society*, 141(11):3128, 1994.

[11] Takayuki Aoyama, Ken-ichi Goto, Tatsuya Yamazaki, and Takashi Ito. Silicon (001) surface after annealing in hydrogen ambient. *Journal of Vacuum Science & Technology A: Vacuum, Surfaces, and Films*, 14(5):2909–2915, 1996.

[12] Henning Döscher, Anja Dobrich, Sebastian Brückner, Peter Kleinschmidt, and Thomas Hannappel. Si(100) surfaces in a hydrogen-based process ambient. *Applied Physics Letters*, 97(15):5–7, 2010.

[13] Yoshiko S Hiraoka. Quantum chemical study of silane decomposition on hydrogen-terminated Si (001) surfaces. *Jpn.J.Appl.Phys.*, 38:2745–2746, 1999.

[14] Christian K Fink, Ken Nakamura, Shingo Ichimura, and Stephen J Jenkins. Silicon oxidation by ozone. *Journal of physics. Condensed matter : an Institute of Physics journal*, 21(18):183001, may 2009.

[15] Nuo Xu, Hideki Takeuchi, Marek Hytha, Nyles W. Cody, Robert J. Stephenson, Byungil Kwak, Seon Yong Cha, Robert J. Mears, and Tsu-Jae King Liu. Electron mobility enhancement in (100) oxygen-inserted silicon channel. *Applied Physics Letters*, 107(12):123502, sep 2015.

Chapter 6

Electrical Characterization of Si-O SLs

Problem statement: Does the band engineered Si-O SL channel result in the enhancement of carrier mobility?

Objective: To investigate the electrical activity of O ALs in Si and to evaluate the mobility of Si-O SL transistor structures.

Organization of this chapter: The first section gives insight in the band structure of Si-O SL using metal Schottky test structures. The deep level defects are detected and is verified with MOSCAP structures. The latter is discussed in the second section. The last section discusses on the electrical mobility of Si-O MOSFETs.

6.1 Schottky Diodes

6.1.1 Band structure of Si-O SL

From theory, Si-O SL is a direct band gap material, where one can detect the optical direct band gap using photoluminescence spectroscopy [1–3]. However, our SL samples did not yield any photoluminescence signature illustrating the absence of direct optical bandgap. The IPE and the Schottky diodes are employed to qualitatively understand the band structure of Si-O SLs.

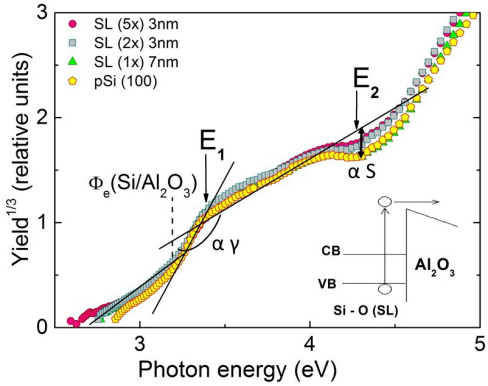

Figure 6.1: Cube root of electron IPE yield versus photon energy measured on $Au/Al_2O_3/Si$-O SL capacitors for different SL devices. The arrows at E_1 and E_2 indicate the onset of direct optical transitions in the Si crystal. The Φ_e is the spectral threshold for electron IPE from Si into Al_2O_3 (as indicated at 3.2 eV). The inset shows the schematic of the observed electron transitions. The γ and S are the yield deviation functions at E_1 and E_2 respectively.

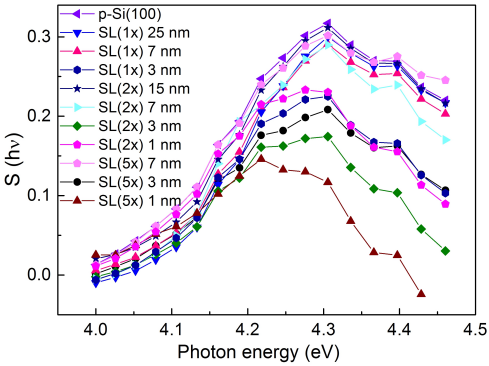

Figure 6.2: The Yield deviation function (S) verses photon energy at the E_2 singularity. For a given SL structures, with decrease in Si thickness there is reduction in direct optical intensity. In addition, the CB shifts down in energy (4.3 to 4.2 eV). The "SL(nx) b nm" in legends indicate the SL structures with "n" number of periods and "b" nm of Si thickness.

Fig.6.1 shows the spectral IPE yield as a function of the photon energy. From the spectral threshold (Φ_e) and the direct optical transitions at E_1 and E_2 singularity, following insight on the band structure is obtained

1. No significant change in Φ_e between SL and the p-Si(100) samples is noticed. Thus the presence of O ALs in Si cause no measurable modification of the VB maximum. The measured zero field barrier height between SLs and Al_2O_3 is similar as that of the bulk p-Si and Al_2O_3 - 3.2 eV.

2. Two changes in the band structure are observed with decreasing Si thickness between O ALs. (1) There is a reduction in direct optical intensity illustrating a decrease in the density of states (Fig.6.2) (2) The CB minima is lowered by 0.1 eV and is speculated to have a change in its wave vector.

Lack of any PL signature, coupled with IPE measurements illustrate that the Si-O SL structure is an in-direct band gap material. A rough estimate of the bandgap is calculated by summing of Si-O SL on n- and p-Si(100).

Fig.6.3 - 6.4 shows the I-V characteristics of Al/Si-O/p-Si(100) and Al/Si-O/n-Si(100) Schottky diodes respectively. A decrease in the forward and reverse current density with Si-O periods is noticed (Fig.6.3). The transport process across the Schottky diodes are assumed to be thermionic emission model [4] and the barrier height (ϕ_B) is calculated from the forward current density using the equation 6.1. This assumption is valid as the ideality factor is 1±0.1 and the doping density extracted from C-V characteristics is as low as 1×10^{15} cm^{-3}.

$$\phi_B = \frac{KT}{q} ln(\frac{A^* T^2}{J_s}) \tag{6.1}$$

where A^* is the Richardson constant (32 A/cm^2 K^2 for p-Si and 120 A/cm^2 K^2 for n-Si) and J_s is the saturation current - extrapolated from the forward current density at zero voltage. The extracted values are shown in the Table 6.1. With an increase in Si-O periods, we can notice a increase in Φ_{Bp} and a decrease Φ_{Bn} (not significant). The physics of the ϕ_B modulation with O ALs is discussed in the next section (6.1.2), while the sum of Φ_B for n and p-type Si substrates result in (Φ_{Bp}+Φ_{Bn}) ∼1.2 eV - similar to the bulk Si bandgap (E_g).

Thus there is no significant change in the Si band structure by inserting O ALs in Si as studied from IPE and Schottky experiments. This is in contrary with the theoretical simulations, where a direct band gap with less than 1.1 eV is expected.

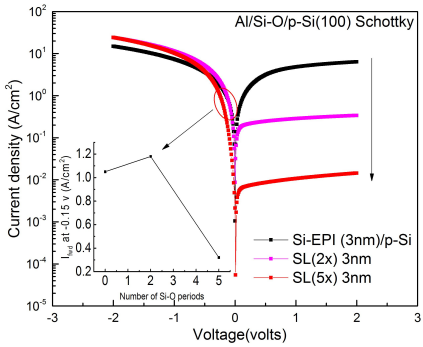

Figure 6.3: I-V characteristics of Al/Si-O/p-Si Schottky diodes. A decrease in the forward (inset) and reverse current is observed with increase in O ALs.

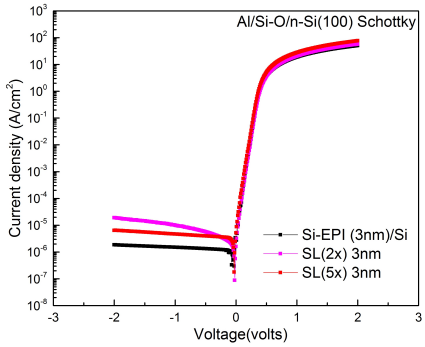

Figure 6.4: Schottky characteristics of Al/Si-O/n-Si Schottky diodes.

	ϕ_{Bn}	ϕ_{Bp}	E_g (eV)
Si-EPI/Si(100)	0.75	0.45	1.2
SL2x 3nm	0.75	0.45	1.2
SL5x 3nm	0.72	0.53	1.25

Table 6.1: The ϕ_B of n and p-type Al/Si-O Schottky diodes extracted from forward current density assuming thermisonic emission model.

6.1.2 Barrier height modulation

With an increase in Si-O periods and/or Si thickness between O ALs, the positive defect density increases and modulates the surface potential causing enhancement in the barrier height. This is illustrated with decrease in forward and reverse current densities as shown in Fig.6.5 and in Fig.6.6. The barrier height values are extracted considering the thermionic emission model and listed in Table 6.2.

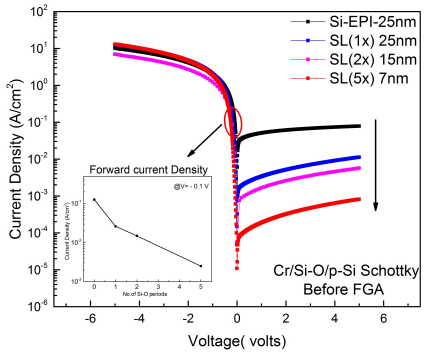

Figure 6.5: I-V characteristics of Cr/Si-O/p-Si(100) Schottky diodes. Decrease in forward (inset) and reverse current density with increase in O ALs with a similar total Si thickness (∼30±5 nm).

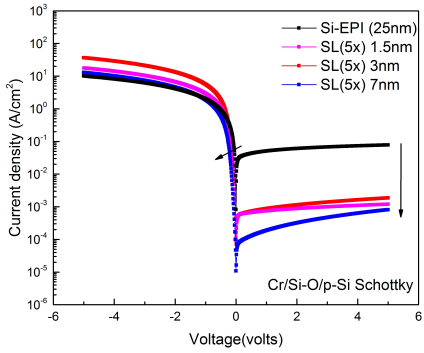

Figure 6.6: I-V characteristics of Cr/Si-O (5x)/p-Si(100) Schottky diodes. Decrease in forward and reverse current density with Si thickness sandwiched between O ALs is indicated by arrows.

	ϕ_{Bp}(eV)
Si-EPI (25nm)/Si(100)	0.5
SL(1x) 25nm	0.55
SL(2x) 15nm	0.59
SL(5x) 7nm	0.64
SL(5x) 1.5nm	0.57
SL(5x) 3nm	0.58

Table 6.2: The first four values of ϕ_{Bp} indicate the impact of Si-O periods for a similar total Si thickness. The last three values of ϕ_{Bp} indicate the impact of Si thickness for a SL(5x) sample. With increase in Si-O periods and/or Si thickness, the ϕ_{Bp} is increased.

Surface states

Among the several mechanisms contributing to the barrier height modulation [5–7], the presence of positive defect centers at Cr-Si interface due to the O ALs is considered to be the dominant. The positive defect centers repel the holes and further bend the bands, thereby increasing the barrier height. This can be understood, by studying the effect of Forming Gas Anneal (FGA) on the Schottky characteristics and the DLTS measurements. The Fig.6.5 and 6.7, illustrate the I-V characteristics for Cr/Si-O/p-Si Schottky diode before and after FGA respectively.

With a increase in the number of Si-O periods for a similar total Si thickness, we notice a decrease in forward and the reverse current densities as shown in Fig.6.5. The decrease in current densities is attributed to the increase in barrier height from 0.5 to 0.64 eV (Table 6.2). The barrier height modulation is by the positive defect centers caused by the O layer, modulating the surface potential close to the interface. These positive defect centers are reduced with FGA, resulting in similar forward and reverse current densities (Fig.6.7).

The increase in positive defect centers with O ALs and with Si thickness is studied using Si-O MOSCAP and Schottky diode test structures respectively.

Fig.6.8, shows the defect distribution across the Si band gap for 5-period Si-O SL structures at varied inter layer Si thickness (1nm, 3nm and 7nm Si). Two prominent differences are observed

1. There is almost an increase of 1 order of magnitude in density of defect states (DOS) with an increase in Si thickness from 1 nm to 7 nm. This illustrates that the time spent in the CVD reactor at a temperature of 500°C has an impact on the hole trap density.

2. There is a broad band of hole traps created by the presence of O layers in Si. A gradual shift in activation energy from 0.22 eV (for 1 nm), 0.34 eV (for 3 nm) to 0.4 eV (for 7 nm) illustrate the change in defect type during the Si deposition at 500°C.

3. During the DLTS measurements, a pulse of certain duration is applied to fill the traps and the capacitance transient is measured. A typical point like defect demonstrate a saturated filling around 1 ms. For Si – O SLs with inter-layer of 7 nm Si thickness, a non-saturated trap filling is observed up to 10 ms, showing an increase in the defect states associated to the extended defects like dislocations or stacking faults [8]. The origin of the defect peak in reference sample around 0.32 eV is not yet known.

The band structure of Cr/Si-O/p-Si(100) Schottky interface with positive hole traps due to the O ALs is shown in Fig.6.9.

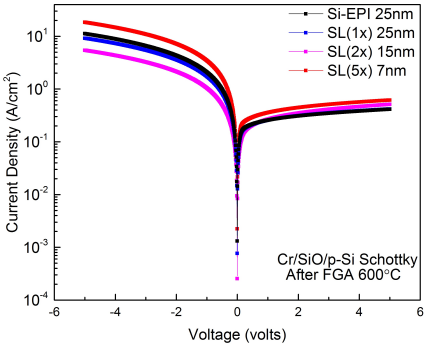

Figure 6.7: I-V characteristics of Cr/Si-O/p-Si(100) Schottky diodes after FGA of 600°C for 1 min.

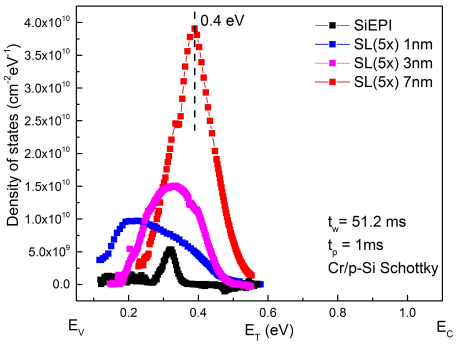

Figure 6.8: Defect distribution of positive hole traps for the SL(5x) with different Si thickness (1, 3 and 7nm) sandwiched between O ALs. The SiEPI is the reference.

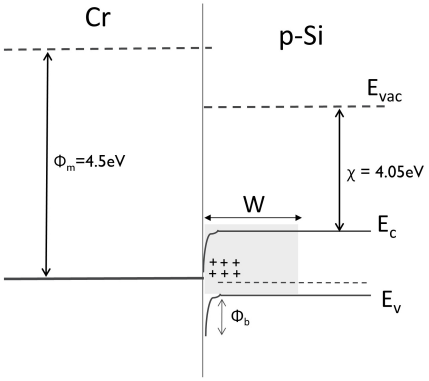

Figure 6.9: Band structure of Cr/Si-O/p-Si Schottky diode at equilibrium. The presence of O ALs act as positive hole traps responsible for the modulation of the surface potential. This diagram is not drawn to scale.

6.2 Metal Oxide Semiconductor Capacitors

Fig.6.10 shows the C-V characteristics of Si-O SL based MOSCAPs. First, it is remarkable that the surface potential can be modulated with gate bias despite the presence of 5 O ALs near the interface. This signifies the excellent epitaxial quality of SL, electrically behaving like a conventional Si semiconductor. Second, the dual sweep of the gate bias, from accumulation to depletion and vice versa, did not yield any hysteresis illustrating the absence of trapped charges in the gate oxide (data not shown). Last we notice a flat band voltage shift (ΔV_{FB}) with increase in number of Si-O periods. As epitaxial Si on Si (without O layer) is considered as our reference with identical process conditions, the observed ΔV_{FB} is attributed to the presence of additional charges, possibly caused by O ALs as quantified in Table 6.3.

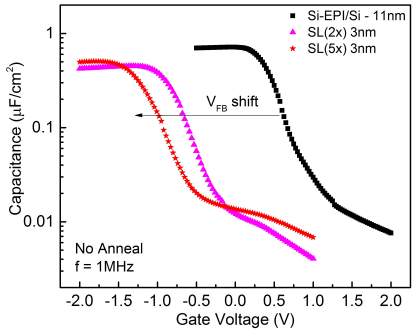

Figure 6.10: C-V characteristics of as deposited Si-O SL MOSCAPs.

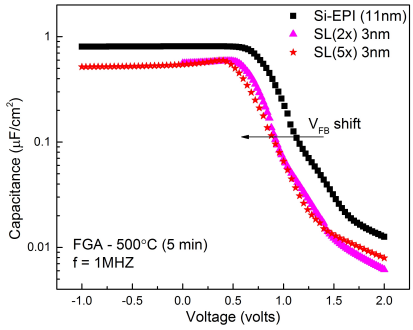

Figure 6.11: C-V characteristics after FGA at 500°C for 5 minutes. The ΔV_{FB} is reduced to 0.13V.

	V_{FB} (volts)	ΔQ (C)	N_{dep} (cm^{-2})
Si-EPI/Si(100) reference	0.63	-	-
SL(2x) 3nm	-0.67	2.7×10^{-7}	1.7×10^{12}
SL(5x) 3nm	-0.97	8×10^{-7}	5×10^{12}

Table 6.3: The flat band voltage (V_{FB}), charge (Q) and the concentration of the defect centers in the depletion region (N_{dep}) of as deposited MOSCAPs increases with increase in number of Si-O periods.

The number of defect centers in the depletion region (N_{dep}) of MOSCAP can be roughly estimated from the flat band voltage shift (ΔV_{FB}) using the equation 6.2 and 6.3.

$$\Delta V_{FB} = \frac{\Delta Q}{C_{ox}} \tag{6.2}$$

$$\Delta Q = q * N_{dep} \tag{6.3}$$

The q is the elemental charge, ΔQ is the change in the depletion charge and C_{ox} is the oxide capacitance. The respective values are indicated in Table 6.3. Compared to the Si-EPI/Si(100) reference, we notice an increase in defect states to 1.7×10^{12} for a 2-period SL with a inter layer Si thickness of 3nm (SL(2x) 3nm). The defect density increases further roughly 2.5 times (5×10^{12}) for a 5 period SL with a similar Si inter-layer thickness (SL(5x) 3nm). This indicates that the addition of O ALs is responsible for the increase in defect density. As understood from the Si-O Schottky diodes, the defects can be lowered by FGA (forming gas anneal), indicating a point like defect types [9]. It is illustrated in Fig.6.11 with reduced ΔV_{FB} of 0.13 volts compared to the as deposited MOSCAPs (Fig.6.10).

Defect Distribution: Further in-depth analysis on the defect distribution is performed using FT-DLTS (Fig.6.12-6.13). It analyse the depletion region of MOS capacitors corresponding to the defects due to the presence of O ALs [9, 10]. Fig.6.12 shows the distribution of the DOS as a function of the defect activation energy E_T. More details on the quantification is explained in Appendix B. A broad distribution of hole traps is centered around the mid-gap (0.48 - 0.53 eV) of Si. The density of the hole traps increases with increase in Si-O periods. The maximum DOS of 4.5×10^{12} cm^{-2} eV^{-1} is detected for SL (5x) 3nm. It is noticed that the C-V measurements slightly overestimate the value of DOS which is due to the first approximation in assuming the ΔV_{FB} is primarily due to the defects only in the depletion region (Fig.6.13). These defects are partially passivated by FGA, resulting in reduction of DOS by 5 times. This could indicate a point like defect behavior (in agreement with Schottky diode measurements). In some devices, a shallow level at E_V + 0.3 eV is detected corresponding to the Si dangling bonds.

Defect Types: Thus two kinds of defects are observed in SL structures. First, the **Si dangling bond defect types** at shallow levels. Second, a mid-gap defect states speculated due to the **related Si-O bond structure** [11].

We also observe a decrease in the activation energy from 0.52 to 0.47 eV with FGA, indicating the change in Si-O bond structure (Fig.6.12 and Fig.6.13). Recently by comparing Si-O SL and Si/SiO_2 capacitor,a similar mid gap defects are detected [10]. Thus it is concluded that, similar Si-O bond structures may be responsible for the deep hole traps in both of these structures [11].

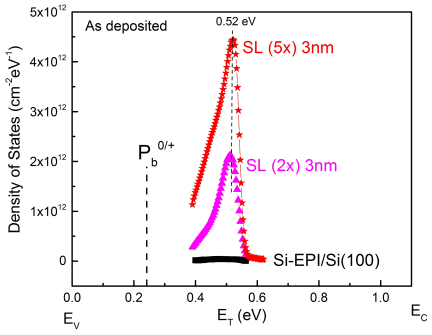

Figure 6.12: Defect distribution in the Si bandgap for as deposited Si-O SL MOSCAPs.

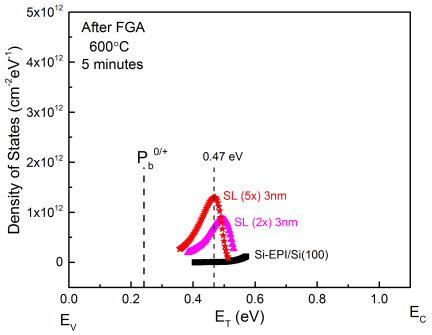

Figure 6.13: Defect distribution in the Si bandgap after FGA at 500°C for 5 minutes.

To evaluate the density of Si dangling bonds in Si-O SLs, ESR measurements were performed on SL(5×) 3nm sample. Fig.6.14, reveals the presence of 2 types of paramagnetic defects in the Si-O SL structures. The prominent broad signal labeled as P_{b0} - **Si dangling bonds defects** originating from the native oxide/SL interface. The second and much narrower signal, next to the marker is observed and identified to be from the **double donors**. The concentration of double donors and the dangling bonds correspond to $1\times10^{10}cm^{-2}$ and $1.2\times10^{12}cm^{-2}$ respectively. Interestingly after the H-depassivation at 620°C for 60 min, both the previously observed signals disappear. Such an unusual behavior reflects in pre-measurement treatment of samples, under which the top 3 nm of Si is removed due to the sequential oxidation and the HF dip. Therefore, it is concluded that the active point defects are only at top layer of the SLs (3nm) and inner layer of SLs are free from dangling bond defects/ESR inactive.

6.3 Metal Oxide Semiconductor Field Effect Transistors

Devices under Test: Si-O SL structures with varying Si-O periods and inter layer Si thickness between O AL are integrated in a CMOS process for mobility evaluation.

Split C-V technique: The mobility of the devices are measured using split C-V technique described elsewhere [12]. The split C-V mobility extraction methodology is illustrated in Fig.6.15 - 6.17. Drive currents and the mobility

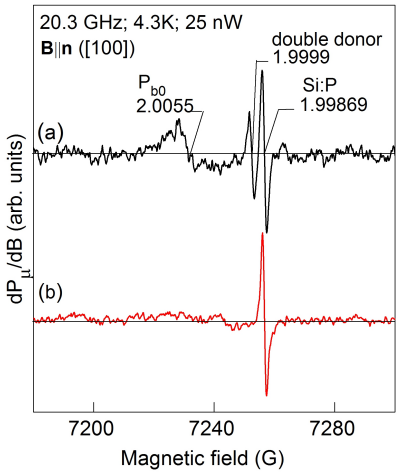

Figure 6.14: ESR spectra observed at T=4.3 K on SL(5x) 3nm sample (a) As grown (b) After de-passivation at 620°C for 1 hr in vacuum. The 1.9999 and 2.0055 corresponds to the g factor (dimensionless magnetic moment) of the electron. The frequency of the incident photon is 20.3 GHz correspond to the magnetic field of 7200 - 7280 G to meet the resonant condition.

values are reported for devices oriented in <110> direction with the FET channel perpendicular to the notch direction of the wafer. The Fig.6.15 shows the inversion C-V which is integrated across the gate voltage to obtain inversion charge carrier density (Q_{inv}). Later the charge density is combined with the channel current (Fig. 6.16) at a low drain bias to obtain the mobility (Fig. 6.17). The equations illustrating the mobility extraction using split C-V are illustrated below (Eq.6.4 - 6.6).

$$\mu_{eff} = \frac{g_{ds}}{C_{ox}(V_{gs} - V_{th})} * \frac{L}{W} \tag{6.4}$$

where μ_{eff} is the effective carrier mobility, g_{ds} is the channel conductance, C_{ox} is the oxide capacitance, V_{gs} is the gate-source voltage and V_{th} is the threshold voltage. The L and W are the length and width of the transistor respectively. The inversion charge density is given by

$$Q_{inv} = C_{ox}(V_{gs} - V_{th}) \tag{6.5}$$

However the above equation is less accurate as the Q_{inv} varies along the channel for the given V_{gs} and V_{ds}. Hence the inversion C-V is integrated across the V_{gs} range to obtain inversion charge carrier density as given in Eq.6.6.

$$Q_{inv} = \int_{-\infty}^{V_{gs}} C_{gc}(V_{gs}) dV_{gs} \tag{6.6}$$

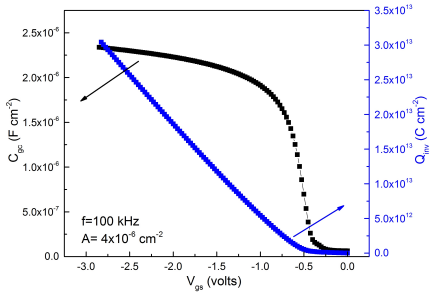

Figure 6.15: Inversion capacitance-voltage and the inversion charge density of a pMOSFET with 3 SL(3x) 1.5nm. The device dimensions are W = 80 μm and L = 5 μm.

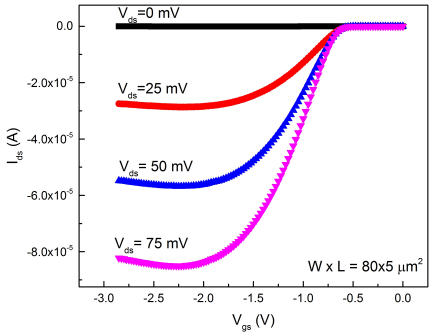

Figure 6.16: Output (I_{ds} vs V_{ds}) characteristics of a pMOSFET with3 SL(3x) 1.5nm. The device dimensions are W = 80 μm and L = 5 μm.

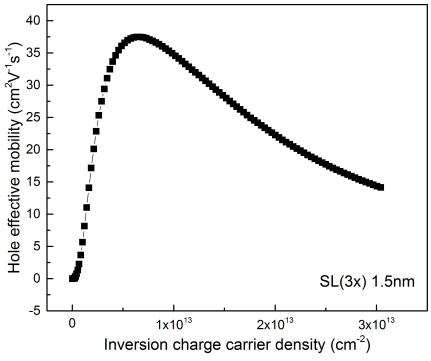

Figure 6.17: Extracted hole mobility from the split C-V technique.

Electrical Performance - Mobility evaluation:

In this section the Si-O SL MOSFET characteristics are analyzed. The extracted mobility at an inversion charge density of 1×10^{13} cm^{-2} for different

Si-O SLs is plotted in Fig.6.18- 6.19. The SL devices are labeled as "SL(nx) b nm", where n and b denote the number of Si-O periods and Si thickness respectively.

The pMOS and nMOS reference mobilities (Si-EPI/Si(100)) are approximately in line with high-κ HfO_2 MOSFET mobilities at similar inversion charge and channel doping density. For the pMOSFET (Fig.6.18), the introduction of a single O AL with 3 nm Si away from channel/oxide interface does not lead to significant mobility degrdation. Most remarkably, the Si-O SL with 1.5 nm Si and 3 O ALs (SL(3x) 1.5 nm) result in limited degradation of mobility compared to the reference within the error limits. SL(3x) 3nm and SL(5x) 3nm lead to a larger degradation of the mobility. This indicates that a larger Si thickness or an increase in Si-O period results in a deteriorating effect on the mobility of the charge carriers. This is likely related to the increase in defects with Si-O periods as discussed in section 6.2. These donor type defects are charged (+ve) and cause coulomb scattering during carrier transport. For nMOSFET (Fig.6.19), the electron mobility is also degraded with Si-O periods. No specific trend in the degradation is observed. More analysis on the defect distribution at top part of the Si band gap is subjected to future study.

In addition, no clear trend in enhancement/degradation of mobility is observed with FGA. The 500°C FGA anneal was performed on devices located on the edge of the wafer, while the devices without FGA anneal were located at the center. The mobility of the devices vary across the wafer, due to the non-uniform deposition of Si. Hence the observed change in mobility after FGA is related to the position of the devices rather then passivation effect after FGA.

Fig.6.20 shows the extracted mobility curves for long channel MOSFETs (W = 80 μm and L = 5 μm). The reference device with epitaxial Si deposition on Si (without any O layer) is shown as well. With increasing number of periods (n=3 and 5),we observe a significant degradation of the hole mobility. The degradation at low inversion carrier density is due to the coulomb scattering, caused by charged defect centers. The presence of donor defect centers was indeed suggested by ΔV_{FB} voltage in the MOSCAP devices, and quantified precisely using DLTS. At high concentration of inversion charge carriers ($>2\times10^{13}$ cm^{-3}), the transport is limited by the surface scattering between the channel/dielectric interfaces. This is in line with our structural understanding, where an increased surface roughness with Si–O periods during growth is noticed from the roughness analysis (section 5.5) The higher number of structural defects in the higher periods and higher surface roughness contribute to the scattering at high inversion carrier densities. Nevertheless, a comparable mobility with our reference device is observed for a three-period Si–O SL (n = 3) with a Si layer of only 1.5 nm thickness. The comparable mobility is observed irrespective of the inversion charge carrier concentration. Two reasons can explain the

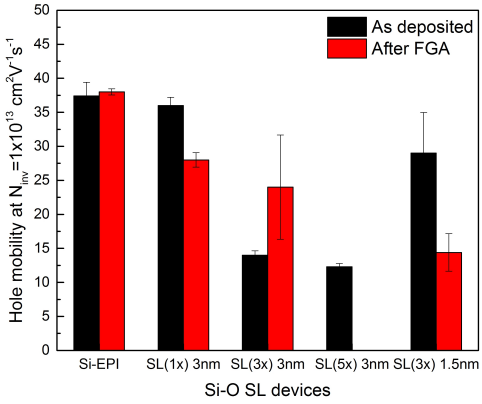

Figure 6.18: Hole mobility for different Si-O SL device before and after FGA. The SL devices are denoted as SL(nx) b nm, where n and b denote the number of Si-O periods and Si thickness respectively. FGA is performed on certain devices at 500°C for 5 minutes. The error bars illustrate the variations across different devices.

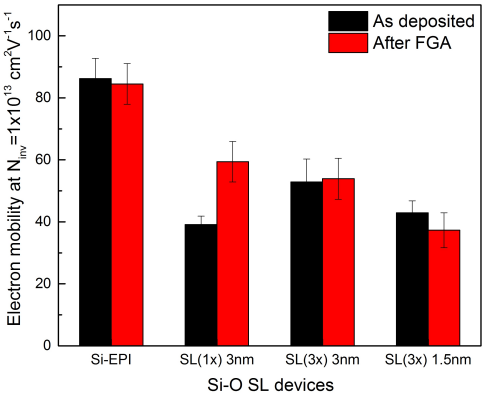

Figure 6.19: Electron mobility for different Si-O SL device before and after FGA.

observed mobility enhancement at thinner Si layers. First, the thin Si layers yield lower rms roughness during growth and hence the surface scattering of charge carriers at the channel/dielectric interface is minimal. Second, thin Si layers between the O layers are effective for quasi confinement and wave function redistribution. This in turn could result in a reduced intra sub-band scattering, which enhances the mobility.

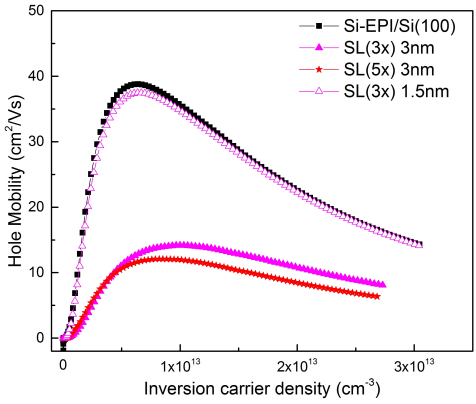

Figure 6.20: Universal hole mobility for different Si-O SL devices at different Si-O periods and Si thickness between.

The thershold voltages (V_{th}) were extracted using the maximum conductance (g_m) method [12]. The trends in the V_{th} for different Si-O devices are in alignment with the trends of corresponding mobility (data not shown). Higher the V_{th}, lower the mobility. Since the V_{th} differences are determined by the differences in charge in the devices, this points to the possibility of coulomb scattering as a cause for mobility degradation. The widening of the difference between nMOSFET and pMOSFET V_{th} as mobility degrades is consistent with charge trapping rather than fixed charge. Fixed charge would not result in a greater difference between n- and p-MOSFET V_{th}.

6.4 Conclusion

The electric properties of epitaxial Si-O SL is studied using Schottky, MOSCAP and FET test structures.

1. The presence of O ALs in Si yield positive defect centers around mid-gap of Si. Two prominent defect types are observed. One is the point type defect of Si−O related, whose intensity increase with number of O ALs. Second is the extended defect type which appear at high inter-Si thickness of 7 nm. These defect types also modify the surface potential resulting in barrier height modulation.

2. The presence of the defects degrade the hole mobility at low gate fields by Coulomb scattering. While at high gate fields, the surface roughness

accumulated during the Si−O growth limit the mobility of carriers by roughness scattering. The change in electron mobility with Si-O periods and Si thickness could not be explained.

Bibliography

[1] Raphael Tsu and John C Lofgren. Structure of MBE grown semiconductor–atomic superlattices. *Journal of Crystal Growth*, 227-228:21–26, jul 2001.

[2] R. Tsu. Si Based Green ELD: Si-Oxygen Superlattice. *Physica Status Solidi(a)*, 180(1):333–338, 2000.

[3] Raphael Tsu, Jonder Morais, and Amanda Bowhill. Visible Light Emission in Silicon-Interface Adsorbed Gas Superlattices. In *Materi. Res. Soc. Symp. Proc. 358*, page 825, 1994.

[4] S.M. Sze. *Physics of Semiconductor Devices*. A Wiley-Interscience publication, 1981.

[5] Winfried Monch. Barrier heights of real Schottky contacts explained by metal-induced gap states and lateral inhomogeneities. *Journal of Vacuum Science & Technology B: Microelectronics and Nanometer Structures*, 17(4):1867, 1999.

[6] Bing-Yue Yue Tsui and Ming-Hong Hong Kao. Mechanism of Schottky barrier height modulation by thin dielectric insertion on n-type germanium. *Applied Physics Letters*, 103(3):032104, 2013.

[7] C R Crowell, H B Shore, and E E LaBate. Surface-State and Interface Effects in Schottky Barriers at n-Type Silicon Surfaces. *Journal of Applied Physics*, 36(12):3843, 1965.

[8] A Berg, I Brough, J H Evans, G Lorimer, and A R Peaker. Recombination-generation behaviour of decorated defects in silicon. *Semiconductor Science and Technology*, 7(1A):A263–A268, jan 1992.

[9] Eddy Simoen, Suseendran Jayachandran, Annelies Delabie, Matty Caymax, and Marc Heyns. Deep levels in silicon–oxygen superlattices. *Semiconductor Science and Technology*, 31(2):025015, feb 2016.

[10] E. Simoen, C. Gong, N.E. Posthuma, E. Van Kerschaver, J. Poortmans, and R. Mertens. A DLTS Study of SiO_2 and SiO_2/SiN_x Surface Passivation of Silicon. *Journal of The Electrochemical Society*, 158(6):H612, 2011.

[11] Eddy Simoen, Suseendran Jayachandran, Annelies Delabie, Matty Caymax, and Marc Heyns. Comparison between Si/SiO 2 mid-gap interface states and deep levels associated with silicon-oxygen superlattices in p-type silicon. *Phys. status solidi*, pages 1–6, may 2016.

[12] Dieter K Schroder and Lawrence G. Rubin. Semiconductor Material and Device Characterization. *Physics Today*, 44(4):107, 1991.

Chapter 7

Conclusions and Outlook

Conclusions

Si-O SLs consists of alternating periods of epitaxial Si layers and O ALs, which are investigated in the context of logical applications. The structure of the Si−O SL plays a significant role in determining the quasi confinement of the charge carriers leading to effective mass engineering. Researchers have demonstrated an enhanced device performance by inserting O ALs in Si. However, the structure of the Si−O of SLs is not yet experimentally verified. On the other hand, simulations have been performed to understand the impact of the structure of Si−O SL for effective mass engineering. Yet, an experimental validation of the improved device performance is lacking. Thus the knowledge gap is: which Si−O structures can result in improved device performance and can be experimentally achieved? My PhD research lowers the knowledge gap with a systematic study on the fabrication process, structural properties and on electrical performance of Si−O SLs.

Creating fully epitaxial Si−O superlattices is challenging as oxygen is usually considered as contaminant that inhibits Si epitaxy. However this work demonstrates that Si epitaxy is allowed for specific structures of O ALs. The O AL with controlled O-content and surface structure are deposited by O_3 exposure on the H−Si(100) surface. For an O-content of less than one AL (1 AL $= 6.78\times 10^{14}$ atoms cm^{-2}), the O atoms are incorporated in the dimer and back bonds of Si, which are considered to be energetically favorable. This structure still provides a template for Si epitaxy. With further increase in O-content, more O atoms at Si back bonds weaken the Si−H bonds by structural distortions

resulting in an incorporation of O atom even at H – Si bonds. This structure does not provide a template for Si epitaxy. Next, the reduction of the Si deposition rate significantly improves the epitaxial quality of Si layers on the O AL, by providing sufficient time for surface diffusion of the Si ad-atoms, enabling incorporation in the Si lattice. Last, the different surface structure after O_2 chemisorption result in different growth mechanism for epitaxial Si on O AL i.e. epitaxial lateral overgrowth of Si over SiOx clusters. The simple repeat processes of Si and O deposition result in a defective superlattice structures primarily due to a high O-content at higher periods ($n \geq 2$), i.e. O-content larger than 1 AL. Hence, the controlled O depositions with O-contents less one AL in the entire structure is the key for achieving fully epitaxial Si-O SLs of up to five periods. Electrically, the amount of positive donor hole traps increases with number of Si-O periods and with the thickness of Si layers. These defects degrade the mobility of carriers at low gate fields through Coulomb scattering, while surface scattering is responsible for the mobility degradation at high gate fields. The defects can be mitigated at low Si thickness sandwiched between O ALs resulting in mobility comparable to the reference epitaxial Si layers.

Theoretically, the Si – O SLs with specific Si – O interface structures are promising for the charge carrier mobility enhancements. After the dedicated experiments, it is found that the O ALs in Si yield defects that degrade the device performance. This is well known to the epitaxial community, that the O defects degrade the lifetime of the charge carriers. However, once can still realize a higher mobility by precisely positioning the O atoms at the required Si – O bond structure, which is experimentally challenging. Further exploration on different O precursors, less inter-layer Si thickness, different Si orientations and other hetero-atoms (C,N,S,CO) are the scope for future research.

Outlook

Suggestions for mobility enhancement

Different approaches are suggested and Si-O SL can be further considered for the mobility enhancement

Theoretical approach - The precise position of O atoms has to be engineered to cause a desired potential perturbation leading to the quasi confinement and the effective mass engineering.

Two of the proposed structures are promising from theoretical simulation - First, the reconstructed Si is connected with Si−O−Si bridges (Rec-I) for electron mobility enhancement. Second, in addition to the Rec-I structure, additional O atoms are introduced in Si dimers for hole mobility enhancement (Rec-II).

The theoretically proposed structures can be realized experimentally in the following sequential way.

1. Oxidation of Si(100) to form the Si/t-SiO_2/a-SiO_2 structure. [t-SiO_2 refers to - Trydymite SiO_2]
2. Hydrofluoric acid treatment to remove the needless t-SiO_2 and a-SiO_2.
3. Epitaxial Si thereon to complete the Rec-II structure.

The proposed above experimental realization is not straightforward and is technologically challenging. The thickness of SiO_2 in step 1 is important as Si/crystobalite-SiO_2 (c-SiO_2) is formed during the initial stages of oxidation. Later the c-SiO_2 is transformed into t-SiO_2 to release the compressive strain during the oxidation process. Hence one might exploit atomic layer etching technique to precisely control the etching of a-SiO_2 and the part of t-SiO_2.

Future work on experiments and Integration -

1. To explore surface reactions of different O precursors on Si with the objective of investigating Si-O bond structures. As different bond structures can lead to different potential perturbation and effective mass engineering, the impact of Si−O structure on electrical mobility can be further studied.
2. It is reported that, the use of NO oxidation can avoid the formation of positive defects centers and the O atoms are deposited onto the Si dimers.

However the incorporation of N during oxidation can be detrimental for sub-band engineering and requires other alternatives.

3. A wider process space can be further investigated for the mobility enhancement. The anneal at 650°C for source/drain activation can potentially cause diffusion of O atoms and limiting the mobility. This can be limited by the development of integration process at low thermal budget ensuring confined O layers. It is also evident from the MOSCAP results that the defect density can be significantly minimized by FGA at 500°C without enhancing O diffusion. Hence we believe a FGA at 500°C after the Si-O SL channel deposition coupled with the low thermal budget integration process could potentially boost the mobility of carriers.

4. The choice of gate stack of TiN/HfO_2 with a thin IMEC clean oxide could induce lots of interface defects with the channel interface. A thermal oxide between the gate dielectric and the channel could have been a better choice for reducing the interface defects. On the other hand, Mears and his co-workers have used nitrated SiO_2/Poly-Si gate stack for the device integration.

Appendix A

Estimation of surface OH density using $HfCl_4$ experiments

In this section, the estimation of surface hydroxyl density from $HfCl_4$ surface reaction is described. The amount of Hf adsorbed on the surface after the first $HfCl_4$ cycle strongly depends on the chemical nature of the silicon surface. On the silicon surface, reaction of $HfCl_4$ with Si−OH sites is preferred than with Si−H and Si−O−Si surface groups.

$$\underline{(-\mathrm{OH})_x} + \mathrm{HfCl_4(g)} \longrightarrow \underline{-\mathrm{O}_x-\mathrm{HfCl}_{(4-x)}} + \mathrm{xHCl_{(g)}} \tag{A.1}$$

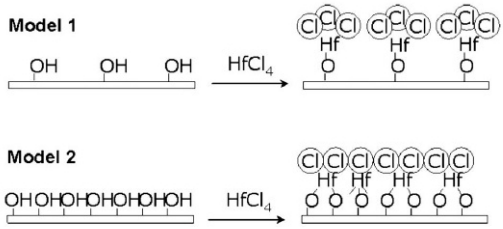

Figure A.1: Schematic representation of the theoretical models used to estimate the surface hydroxyl density from Hf concentration after one $HfCl_4$ chemisorption reaction

Two theoretical models describing the dependence of the $HfCl_4$ chemisorption on the hydroxyl density are proposed based on the ligand exchange reaction (Eq. **??**). Both models assume that $HfCl_4$ strictly reacts only with Si−OH surface sites, and that all these surface sites are eventually occupied after the first reaction pulse. The schematic of the models are indicated in Fig. **??**.

$$\#OH = \#Hf \tag{A.2}$$

The first model describes the direct relation between the Hf concentration and the surface −OH density (Eq.**??**). If the surface −OH density is placed far apart, then eventually only one $HfCl_4$ reacts on each −OH groups and hence can be directly estimated from Hf content. However the limitation of this model is that, when the distance between the hydroxyl groups are smaller, one $HfCl_4$ can react with two or even three −OH groups resulting in the deviation of the model.

The second model is based on steric hindrance of the Cl ligands at the surface and applicable to the surfaces with high −OH density. This model assumes the reaction of $HfCl_4$ with most of the surface hydroxyls while maintaining the maximum packing density of the Cl ligands. The −OH density on the surface is then calculated by the mass balance equation of the $HfCl_4$ chemisorption

$$\#OH = \#HCl_{(g)} = (4 \times \#Hf) - \#Cl_{max} \tag{A.3}$$

The −OH density before chemisorption equals the number of HCl molecules release after the $HfCl_4$ reaction (Eq.**??**). The number of released HCl molecules is the difference between the number of Cl ligands associated with $HfCl_4$ ($4 \times$ #Hf) and the amount of Cl remaining at the surface after the chemisorption reaction dictated by the steric hindrance ($\#Cl_{max}$) (Eq.**??**).

To summarize, the Fig.**??** illustrate the models to estimate the surface −OH density from the measured Hf content. The slope remains unity for the one $HfCl_4$ chemisorption on one OH group. The slope degrades for one $HfCl_4$ chemisorption on 2 or 3 OH groups. For the surface with maximum hydroxyl density, the steric hindrance model (second model) is used to estimate the surface OH density.

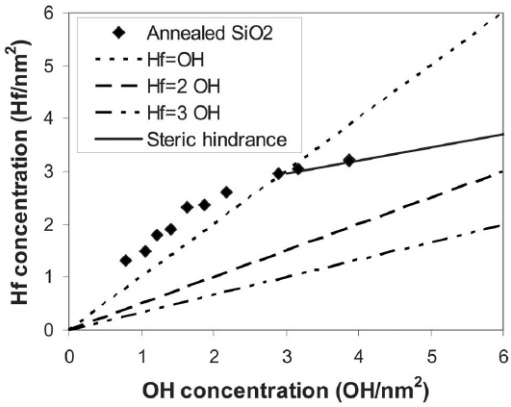

Figure A.2: Relation between Hf concentration at 300°C after the first $HfCl_4$ reaction cycle.

Appendix B

Quantification of DLTS spectra

Prior to the DLTS frequency-scan, the C-V characteristics is measured at 1 MHz. The gate voltage is swept from depletion to accumulation and back applied on the top (gate) contact. The C-V characteristics are detailed in the section . Next the trap filling kinetics is studied at room temperature whereby the DLTS amplitude (capacitance transient - ΔC) was measured versus the bias pulse duration (t_p), in the range of 10^{-8} to 1 sec. A voltage pulse (V_p) is varied from the depletion (V_R) to an accumulation to fill the traps during the t_p time. Then, for a t_p duration corresponding to the saturated filling of traps, the so-called isothermal frequency scan (F-scan) was applied, where the sampling period (t_w) is varied between 1 ms to 10s at room temperature. The t_w is proportional to the activation energy (E_T) of the traps by assuming a constant hole capture cross section (σ_p) given by Eq.B.1.

$$E_T = E_V + kT\ ln(3.33 \times 10^{21} \sigma_p T^2 \tau_0) \tag{B.1}$$

with E_V is the top of the valence band, k as the Boltzmann's constant and τ_0 is the emission time constant proportional to t_w ($\sim t_w/2.33$) at constant temperature T. The DLTS amplitude is been normalized with the steady state capacitance (C_R) and density of defect states (D_T) is quantified using the equation B.2.

$$D_T = \frac{\epsilon_{Si} C_{acc} A_{cap} N_{dop} \Delta C}{(C_R^3 kT\beta)} \quad (cm^{-2}eV^{-1}) \tag{B.2}$$

with the ϵ_{Si} being permittivity of Si, C_{accu} is the capacitance at accumulation regime, A_{cap} is the capacitor area, N_{dop} is the substrate doping density which can be derived from the C-V characteristics. The ΔC is the DLTS amplitude and β is the energy resolution factor, estimated to be 2.5. As an example, a quantified DLTS spectra from the F-scan (Fig. B.1) is shown in Fig. B.2.

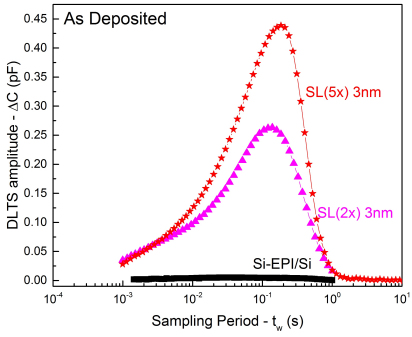

Figure B.1: F-scan (t_w) of DLTS for different SL samples at RT.

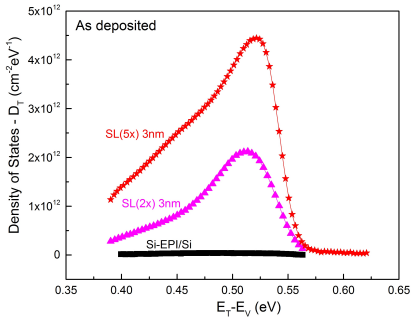

Figure B.2: Density of states (D_T) vs activation energy (E_T-E_V) derived from F-scan at RT for as deposited SL samples.

Appendix C

Integration steps for the fabrication of Si−O SL transistors

In this section the fabrication of the Si−O SL MOSFETs is detailed in the order of the different processing steps involved.

Well Implants

Device quality (<0.13 μm) Czochralski n-type (phosphorous, 12 ±3 ohm.cm) and p-type (boron, 16-24 ohm.cm) silicon wafers were used to fabricate Si−O SL transistors. Crystal orientation was (100). Notch orientation is <110>. The wafers are supplied by MEMC. A 13 nm PECVD SiO_2 was deposited on the wafers as implant oxide. The well implants for the n-type wafers were: P 30keV 5 3.2×10^{11}cm^{-2} , P 60 keV 5×10^{11}cm^{-2}, and P 120 keV 9×10^{11}cm^{-2}. For the p-type wafers, B 15 keV 6×10^{11} cm^{-2}, B 30 keV 1×10^{12} cm^{-2} , B 60 keV 1.2×10^{12} cm^{-2}. A 1000°C rapid thermal anneal for 20s in N_2 was used to activate the well implants. The implants were chosen to obtain a $\sim1\times10^{17}$cm^{-3} dopant concentration up to a depth of ∼200nm. The well dopant concentration limit the mobility degradation in the MOSFET inversion channel due to the dopant scattering.

Si–O SL growth

After well formation the Si–O SL were grown in an ASM polygon reactor equipped with Epsilon epi reactor and a Pulsar atomic layer deposition (ALD) reactor, allowing *insitu* processing with wafer transport under inert N_2 ambient. The process steps for the Si–O SL growth are enumerated below

1. Si(100) surface preparation: IMEC Clean, HF clean (2% for 30 sec) and a standard pre-epi bake for 2 min at 850°C in H_2 with a reactor pressure of 40 Torr. The wafers are cooled down to 350°C in H_2 to ensure H-termination.
2. O deposition: O_3 exposure (ppO_3 = 0.01 Torr) at 50°C on the H-terminated Si surface. The O_3 exposure time is limited to 50 ms to control the deposited O-content to 1 AL (1 AL = 6.78×10^{14} at/cm^2.
3. Si deposition: Epitaxial Si deposition on an O-layer using SiH_4 chemistry at 500°C, with a pressure of 20 mTorr using N_2 as carrier gas. The growth rate of Si is 0.2 nm/minute. An incubation period of ∼9 minutes should be taken into account while designing the deposition time for the desired Si thickness.
4. Surface Passivation Anneal: An *insitu* surface anneal is performed at 600°C in H_2 for 5 minutes. This step ensures H-termination at each of period of Si during the growth of SLs.
5. Steps 2-4 are repeated until the desired number of Si–O periods are fabricated.

The thickness of the top Si layer in SLs was adapted (1.5 nm thicker) to account for the Si loss during subsequent processing. The lot has both pMOSFETs and nMOSFETs. Reference wafers are included as an epitaxial-Si on Si (without O layers) grown with the similar conditions as in the 2D nanolattices. Lattices were grown with a 3nm and 5nm Si with 1, 3 and 5 O ALs between.

Isolation

Direct Moat Isolation was realized by depositing 350 nm of PECVD SiO_2 on top of the Si–O SLs. This oxide was patterned using I-line lithography and a combination of Ar sputtering, CF_4 based oxide dry etching and 2% HF wet etching. This process results in the oxide having ∼45° sloped edges. These sloped edges are important to ensure that the gate electrode runs smoothly across the isolation side walls. The isolation is thicker than 80 nm everywhere as

required for the source/drain junction implantation step. The isolation thickness will ensure that the silicon underneath the isolation does not get doped by the implantation and retains the well doping of the opposite type.

Gate Stack formation

The gate stack was formed by first performing an IMEC clean which forms a chemical oxide serving as the interfacial SiO_2 on which the high-κ gate dielectric was deposited. The resulting chemical SiO_2 oxide is 1-1.2 nm thick. Later a 2.7 nm HfO_2 deposition was done in an ASM POLYGON 200 mm reactor. The HfO_2 needs to be thinner than 3 nm to avoid crystallization and excessive charge trapping which results in large hysteresis in I-V and C-V characteristics. A 3nm HfO_2 results in $\sim$ 1.5 nm EOT (Effective Oxide Thickness) and $1\mu Acm^{-2}$ gate leakage,a 2nm of oxide results in 1 $mAcm^{-2}$ at 1V, which compromises capacitance and carrier mobility. A 10 nm PVD TiN/TaN metal act as the gate electrode (Fig. C.1).

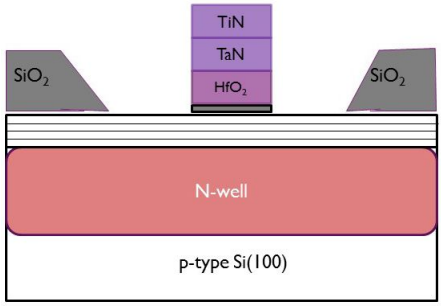

Figure C.1: Schematic of Si–O device after gate stack integration.

S/D Junction activation

Forming appropriate junctions in substrates containing Si–O SL while maintaining the integrity and electrical quality of the SL channel is one of the key challenges relating to MOSFET fabrication (Fig. C.2). The presence of SL channel is likely to increase defectivity at source/drain junctions. A thermal activation at a temperature is required to ensure re-crystallization of the S/D junctions with limited O diffusion. No work has been published detailing the formation of junctions in Si–O SL based transistors. Both the 1000°C spike annealing and a low thermal budget SPER (Solid Phase Epitaxial Regrowth) junctions (650°C for 5 minutes) are investigated. The latter SPER anneals

are preferred to conserve the properties of Si–O SLs, with acceptable junction leakage and no observed O diffusion.

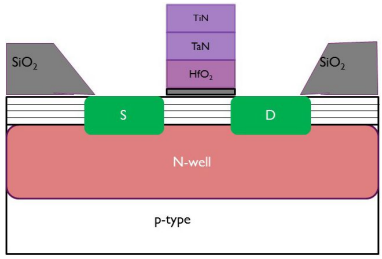

Figure C.2: Schematic of Si–O device after Source/Drain stack integration.

Contact metallization

After junction implants 120 nm of PECVD SiO_2 was deposited and contact openings were patterned with I-line lithography. A 2nm Ti and 200nm TiN were deposited by PVD acting as the Source/Drain contacts. The backside of the wafer was covered with blanket TiN (Fig. C.3).

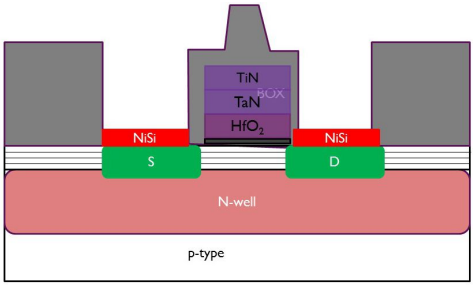

Figure C.3: Schematic of Si–O device after contact metallization.

Arenberg Doctoral School of Science, Engineering & Technology
Faculty of Engineering Science
Department of Materials Engineering
Research group ...
Kapeldreef 75
B-3001 Leuven

KATHOLIEKE UNIVERSITEIT LEUVEN

ASSOCIATIE K.U.LEUVEN

FACULTY OF ENGINEERING SCIENCE
DEPARTMENT OF MATERIALS ENGINEERING
RESEARCH GROUP ...
Kapeldreef 75
B-3001 Leuven
suseendran.jayachandran@imec.be
www.website.kuleuven.be